PREDICTION OF LAMINARIZATION IN BUOYANT TURBULENT PIPE FLOW OF LOW

PRANDTL NUMBER FLUID

A Dissertation

by

ADAM MICHAEL OLER

Submitted to the Office of Graduate and Professional Studies of
Texas A&M University
in partial fulfillment of the requirements for the degree of

DOCTOR OF PHILOSOPHY

Chair of Committee,	Mark Kimber
Committee Members,	Pavel Tsvetkov
	Karen Kirkland
	Maria King
Head of Department,	Michael Nastasi

August 2020

Major Subject: Nuclear Engineering

ABSTRACT

Turbulent pipe flow with $Pr = 0.026$ is studied using Reynolds Averaged Navier Stokes (RANS) and Large Eddy Simulations (LES) for $Re_d = 5300$ under various Richardson numbers with a constant heat flux boundary condition. The goal of this study is to better understand and improve predictions of buoyancy aided mixed convection in low Prandtl number fluids with an emphasis on the transition to laminarization.

The present work is validated using Direct Numerical Simulations (DNS) data and LES data available in literature and also performed in-house. At the onset of this investigation very limited data existed for only a few Richardson numbers in peer reviewed literature. Using this data as a validation, LES was performed using OpenFOAM to fill in gaps and widen knowledge in the ranges of interest. Using this newly created data set, a thorough investigation is performed to determine how common eddy-viscosity RANS models predict mixed convection turbulent pipe flow in low Prandtl number fluids. Using this for a base of knowledge, a thorough calibration framework is constructed that allows for the calibration of low Reynolds $k - \epsilon$ turbulence models. Additionally, to assess the improvement of model performance a quantitative comparative error analysis framework is developed to guide in model calibration. The results from this study represent a solid foundation for future model development that is easily accessible for the user.

DEDICATION

To my mother and father.

ACKNOWLEDGMENTS

CONTRIBUTORS AND FUNDING SOURCES

TABLE OF CONTENTS

LIST OF FIGURES

x

LIST OF TABLES

NOMENCLATURE

A	Actual Value
Re_d	Bulk Reynolds Number
T_b	Bulk Temperature
x, y, z	Coordinate System
ξ	Cumulative Relative Error Measure
ρ	Density
x	Distance
μ	Dynamic Viscosity
F_s	Factor of Safety
Δ	Filter Width
$\prime$	Fluctuating Component
u_τ	Friction Velocity
Gr	Grashof Number
g_j	Gravity Vector
$\sim$	Grid Filter
δ	Half-Width
ν	Kinematic Viscosity
δ_{ij}	Kronecker Delta
L	Leonard Stress
$\Delta r^+, \Delta \theta^+, \Delta z^+$	Non-Dimensional Distance Between Cells
$*$	Non-Dimensional Quantity
T_m	Non-Dimensional Temperature

y^+	Non-Dimensional Wall Unit
N_r, N_θ, N_z	Number of Cells in Each Direction
Nu	Nusselt Number
o	Order of Convergence
D	Pipe Diameter
Pr	Prandtl Number
P	Predicted Value
p	Pressure
r	Radius
T_{ref}	Reference Temperature
r	Refinement Factor
Ri	Richardson Number
C_f	Skin Friction Coefficient
c_p	Specific Heat
σ	Standard Deviation
S_{ij}	Strain Rate Tensor
sgs	Sub-Grid Stress
f	System Response Quantity
T	Temperature
$\hat{}$	Test Filter
λ	Thermal Conductivity
β	Thermal Expansion Coefficient
$\overline{f}$	Time Averaged Quantity
E	Total Energy
ϵ	Turbulence Dissipation Rate

k	Turbulence Kinetic Energy
μ_t	Turbulent Dynamic Viscosity
ν_t	Turbulent Kinematic Viscosity
Pr_t	Turbulent Prandtl Number
Re_τ	Turbulent Reynolds Number
u	Velocity Vector
$q"$	Wall Heat Flux

1. INTRODUCTION

Turbulent mixed convection finds relevance in a wide variety of engineering applications, ranging from power generation to heat dissipation from buildings and other structures. In many cases, accurately predicting turbulent mixed convection is of great importance when analyzing the performance and/or safety of a given system under a range of conditions. One phenomenon that has a large impact on a system is laminarization. This can occur from various sources and has a dramatic effect on otherwise fully turbulent flows. The impact of laminarization fundamentally alters a flow causing reduction of drag forces and heat transfer. Garg et al. [1] is an example of a study that has demonstrated that buoyancy can disrupt the near-wall burst sweep process normally present in turbulent flow which causes turbulence production to decrease dramatically leading to laminarization. In buoyancy aided configurations, where the gravitational vector is oriented opposite to that of the bulk flow direction, local density changes begin to emerge in the near-wall heated regions. The result of this is a reduction of velocity gradients from the wall to the core of the flow, resulting in reduced shear stress.

Understanding this phenomena is vitally important in many engineering applications. In the nuclear field, a key feature of next generation reactor design is passive safety. If a pump is damaged, these systems make use of natural convection to maintain adequate heat removal from the core. This involves multiple regime changes from forced convection to mixed convection and eventually to natural convection, and during this time, laminarization is possible. Being able to predict this phenomena is paramount for the safe operation of these reactors. A potential benefit of laminarization is a reduction in friction and required pumping power due to the decrease in turbulence levels.

While the current study is focused on buoyancy influenced physics, it is useful to draw comparisons to other efforts aimed at understanding how turbulence can be attenuated. Significant work on controlling turbulent boundary layers has been performed by Tsao et al. [2], Ho and Tai [3], and Kim [4] using micro-electro-mechanical-systems (MEMS). Other studies have investigated

the interactions between magnetic fields and liquid metals, which are known to cause a variety of phenomena including suppression of turbulence. Branover [5] is an example of an earlier work that demonstrated the suppression of turbulence in pipe flow with both transverse and longitudinal magnetic fields.

Due to the complicated physics involved in predicting turbulent mixed convection, both experimental and computational studies are necessary. Experimental efforts have a long history and serve as the basis of many textbook correlations in use today, but often focus on global characterizations such as the average Nusselt number [6] [7] [8] [9] which are used to form empirical correlations [10] [11]. Examples of upward heated air flow studies include Carr et al. [12] and Polyakov and Shindin [13], where velocity profiles were measured using hot-wire anemometry and laser Doppler anemometry, respectively, to calculate the skin friction using velocity gradients at multiple axial positions. Their studies demonstrated that initially the skin friction decreases with increasing heat flux and reaches a minimum value, beyond which a further increase in heat flux causes the skin friction to also increase. These and other experimental efforts can be extremely challenging unless a tight control of the surroundings is achieved. More recent efforts have been made to capture full field co-located velocity and temperature measurements. These experiments have explored thermographic particle image velocimetry as a potential method to resolve these coupled fields. In thermographic particle image velocimetry, specialized phosphors featuring temperature-dependent emission spectra are seeded into the flow. After excitation from a UV laser source, high-speed cameras are used to characterize the flow field via conventional particle image velocimetry and measure the local temperature via phosphor thermometry. By combining these two techniques, simultaneous full-field measurement of velocity and temperature is achievable. Fond et al. [14] showed this as a valid method of obtaining simultaneous temperature and velocity measurements in high-temperature applications (e.g., combustion). Time-averaged experiments have also been conducted by Omrane et al. [15], while single-shot experiments were accomplished by Someya et al. [16] and Neal et al. [17]. The signal-to-noise ratio seems to preclude this technique from validation-type measurements at lower temperatures, and although further studies will undoubt-

edly address this shortcoming, capturing the data required for numerical model validation on a local scale remains a challenge for turbulent mixed convection.

While advancements have been made to allow these studies for fluids such as air and water, there are important systems which rely on the performance of liquid metals. Liquid metals have gained more traction as a potential coolant for next generation reactors due to the rapid increase in computational power in the past few decades. They are attractive as a coolant due to increased heat transfer efficiency and large ranges between melting points and boiling points. Experimentally, these can be difficult to work with due to the necessity for constant heating to maintain a liquid state. The opacity of the fluid also makes traditional flow measurements such as particle image velocimetry impossible. Due to these, and other numerous challenges, high fidelity experimental data is not as prevalent compared with data for air or water. Schulenberg and Stieglitz [18] summarized various techniques for providing accurate measurements of systems with liquid metal. This highlighted current flow measurement techniques along with the challenges still faced in experimental facilities. Some experimental studies exist; for example, Buhr et al. [19] performed a study on the heat transfer of mercury in a vertical pipe configuration. As one might expect, the study found the relationship between Nusselt number and buoyancy to be analogous to that observed in other fluids, demonstrating a significant decrease in turbulence followed by a clear recovery. But differences also exist. For example, an investigation by Jackson et al. [20] with sodium as the working fluid concluded that heat transfer is enhanced in upward flow and impaired in downward flow which is conversely true for higher Prandtl number fluids. Jackson [21] also developed a theoretical model which provides criterion for the conditions that buoyancy influence becomes significant for both upward and downward flow for liquid sodium (Pr = 0.001) which determined the onset of significant effects from buoyancy in liquid sodium occur at a Richardson number equal to 0.002. More detailed reviews of earlier works involving mixed convection can be found by Jackson et al. [22] and later Jackson [23].

While these experimental studies are vital, it is often difficult to capture the underlying phenomena which govern the observed physics. To gain more insight into these problems, higher

3

order computational models, such as direct numerical simulations (DNS) or large eddy simulations (LES) have also been employed. Kasagi and Nishimura [24] highlighted the similar effects between magneto-hydrodynamic (MHD) flow in a transverse magnetic field (Ohtsubo [25]) and turbulent mixed convection of air between two infinite parallel plates. This study also underpins the common ground shared from different mechanisms (MHD and buoyancy) that have similar signatures when observing the flow physics. For both magnetic induced turbulence attenuation and buoyancy induced laminarization, the overall effect on the fluid motion occurs through distortion of the shear production of turbulent kinetic energy imparted through body forces. You et al. [26] performed DNS for upward and downward mixed convection flows for air in a pipe with a range of Richardson numbers, which categorize the relationship between buoyant, inertial and viscous forces, from 0.0 to 0.241. Patterns and behaviors identified in their study were similar to those from experimental efforts, namely that for the upward flow configuration, a laminarization begins to take effect as the buoyancy is increased and a recovery of turbulence is observed beyond the minimum skin friction. Zhao et al. [27] performed DNS for buoyancy aided mixed convection of lead-bismuth eutectic ($Pr = 0.026$) pipe flow. This study revealed the onset of laminarization occurs much earlier in liquid metal than in air. In the downward configuration, the heat transfer was only increased due to the opposition of buoyancy and flow direction. Aside from the findings consistent with experiments, these numerical studies also allow the investigator to unobtrusively probe the flow in ways not possible in real world experiments. This allows incredibly detailed flow physics to be fully resolved for analysis. An example of an excellent study on this topic was done by He et al. [28], where DNS was performed to investigate laminarization of turbulent flows from a stream-wise body force for both constant and spatially varying body forces for air (Pr=0.071). This level of physics-based understanding would not be possible experimentally. With the availability of high fidelity computational and experimental studies, validation of models that require much less computational power than DNS or LES is possible.

Reynolds averaged Navier-Stokes (RANS) turbulence models have been widely used to solve various flow problems in engineering and science. While these models are very useful, their basis

lies in assumptions that are made in the construction of the model. Based on this, their intrinsic reliability is hinged on validation against experimental or higher fidelity computational studies. Examples of these types of studies include [29], where an assessment of RANS models was performed in the forced convection regime, and Bae et al. [30], where the authors analyzed RANS models for highly buoyant flows. Over several studies Keshmiri and various collaborators [31] [32] [33] performed investigations of buoyancy-influenced flows in vertical tubes, but limited their analyses to only qualitative comparisons of turbulence models. Recently, Clifford and Kimber [34] performed an assessment of RANS based turbulence models of flow on a heated vertical surface with buoyancy effects. This study highlighted limitations of current RANS models. One potential deficiency was in the prediction of the turbulent viscosity ν_t.

Multiple assessments of computational models for low Prandtl number flows have also been performed. Shams et al. [35] [36], Roelofs et al. [37], and Grötzbach [38] are examples of studies on the status of turbulent heat transfer modeling for low Prandtl number fluids. A consensus among these studies is that there is currently no single model capable of capturing forced, mixed and natural convection regimes to a high degree of fidelity. Many of the approaches are focused on the closure of the turbulent heat fluxes through algebraic heat flux models. Kenjereš et al. [39] were among the first to develop these methods. Shams et al. [40] calibrated their models to extend to liquid metals. De Santis et al. [41] performed direct numerical simulations (DNS) of mixed convection for in a horizontal channel flow for low Prandtl number fluids with an assessment of an algebraic heat flux model used with a Reynolds Averaged Navier Stokes (RANS) approach. De Santis and Shams [42] also performed a RANS assessment using a low Reynolds turbulence model coupled with an algebraic heat flux model. These studies further highlighted the need for different modeling approaches to capture buoyant flows.

With several deficiencies in the computational simulation of buoyant flows highlighted, this investigation aims to further assess and address some of these limitations. As previously mentioned, laminarization has a rather drastic effect on both the heat transfer and friction forces present in many engineering applications. To further understand the limitations of current models, an assess-

ment of multiple RANS based approaches was performed using the DNS of Zhao et al. [27] as validation. From this, another need was identified. A common feature between these previously mentioned RANS validation studies lies in the qualitative identification of a model's ability to capture a given set of physics. These studies rely on an "eye test" to asses model error and validity. In order to properly validate these models, a quantitative approach is needed. Though many error metrics exist and are currently used for error quantification, these metrics lack insight into the physics of the problem. A framework to demonstrate the potential of quantitative model assessment is developed. The present investigation examines the mean profiles of velocity, temperature, and turbulence (and their gradients) predicted by four RANS-based turbulence models against the seminal DNS results of Kasagi and Nishimura [24]. Using a modified error analysis, the predictive capacity of each model is quantified to provide a comprehensive assessment of its capacity for turbulent mixed convection scenarios. The error in each prediction is combined into a single metric which is compared from model-to-model. This investigation also involved a sensitivity analysis of the damping function f_μ used in the calculation of the turbulent viscosity. It was found that the calculated skin-friction coefficients and Nusselt numbers were especially sensitive to changes in the parameters of f_μ. From this, possible modifications could be made to existing models to improve their predictions for mixed convection. Using this framework, the same approach was applied against the DNS by Zhao et al. [27]. This study further highlighted that while different modeling approaches exist, there is still need for additional model development to accurately capture these flows

With these results and the hypothesis presented by Clifford and Kimber [34], an approach to modify the turbulent viscosity ν_t was developed. A common RANS approach involves the use of low Reynolds $k - \epsilon$ models. These models resolve turbulence down to the laminar sub-layer. Examples of these include models developed by Yang and Shih [43] and Lam and Bremhorst [44]. While these models have been widely used, one of their limitations lies in the parameterization of coefficients in the damping function f_μ. Using a gradient-based grid search approach, a calibration technique is developed. This technique is shown to have a remarkable effect on the prediction of

laminarization in buoyancy-aided liquid metal pipe flow. A unique feature of this framework is that only required data from DNS or experiments other than boundary conditions and initial conditions is the skin friction coefficient.

In order to validate this method, it was was determined that additional validation data was necessary. A recent LES study by Centurelli [45] attempted to better quantify the onset of laminarization using a Reynolds Averaged Navier-Stokes (RANS) based approach to identify the minimum skin friction with a subsequent LES study to follow. Analysis of these results determined that the findings were not physical and were not usable as a validation metric. With the lack of trusted data for validation, it was determined that new data must be generated.

Using Zhao et al. [27] as validation, LES was performed for two Richardson numbers ($Ri =$ 0.017 and 0.040). With exceptional agreement between DNS and LES results, four additional predictive cases were run in between the two validation cases ($Ri = 0.022, 0.025, 0.030, 0.035$). The results from this determined that laminarization occurs earlier than predicted by Zhao et al. [27]. This study also determined that the degree that the skin friction coefficient and Nusselt numbers are affected was significantly larger than previously predicted. Using this data long with the DNS results from Zhao et al. [27], the complete picture of how laminarization occurs for this flow condition is obtained. With the addition of LES validation data, calibrations at each of these Richardson numbers was successfully performed. The results from this investigation show a complete numerical analysis. It was determined that RANS numerical models have a problem predicting laminarization. Using higher fidelity numerical methods (DNS and LES), this problem was further studied to gain a great understanding of the physics and using this increased understanding successful attempts were made to determine improvements that can be made to the models. The contributions from this dissertation are summarized as following:

- Framework for comparative quantitative analysis between models

- Sensitivity analysis of damping functions for low Reynolds turbulence models

- LES of buoyancy-aided mixed convection for LBE at $Re = 5300$

    - Prediction of onset of laminarization

    - Predictions of skin friction behavior

    - Predictions of Nusselt number behavior

    - Predictions of Reynolds stress anisotropy

- Framework for turbulence model damping function calibration

2. QUANTITATIVE ASSESSMENT OF EDDY VISCOSITY RANS MODELS FOR TURBULENT MIXED CONVECTION IN A DIFFERENTIALLY HEATED PLANE CHANNEL

2.1 Section Summary

Turbulent mixed convection between two vertical, infinite parallel plates at different temperatures is studied using various two-equation turbulence models. The numerical simulations are performed at a turbulent Reynolds number of $Re_\tau = 150$ and a Grashof number of $Gr = 9.6 \times 10^5$. Comparisons are made against highly trusted DNS results. Consistent with the DNS approach, the current simulations are performed using constant properties and the Boussinesq approximation to predict the influence of buoyancy. Previous studies have provided assessments of two-equation turbulence models for various scenarios, but often rely on a qualitative "eye" test in order to determine the most appropriate model to predict a given flow. This study aims to provide a quantitative assessment that accounts for both the physics captured by the turbulence model as well as the magnitude of the system response quantities (SRQ) using a modified symmetric mean absolute percent error (SMAPE) method. Uncertainty quantification is also performed to determine the discretization error for each turbulence model. Recommendations are made as to which turbulence models best capture the physics – hydrodynamically and thermally – using both local and global validation metrics. Lastly, a sensitivity analysis is performed on the damping functions used in the most accurate models. This underpins the potential of model developments and adjustments most worth pursuing for buoyant flows. Overall, this framework provides a more physics-based comparative analysis of the selected turbulence models.

2.2 Numerical Method

To replicate the DNS calculations of Kasagi and Nishimura [24], a two-dimensional representation of a differentially heated plane channel (refer to Figure 2.1) is generated using ANSYS [R] ICEM by Ansys [46]. In the current study, the computational domain is prescribed to be 2δ x $5\pi\delta$ in the x- and y-directions, respectively, with translational periodicity in the stream-wise (y) direction. Using the projection-based meshing framework, a base grid of 120 cells in the x-direction (2δ) and 200 cells in the y-direction ($5\pi\delta$) is constructed for model assessment. The mesh is carefully adjusted in the transverse direction to ensure $x^+ \leq 0.50$, permitting accurate resolution of the thermal and hydrodynamic boundary layers with each analyzed turbulence model.
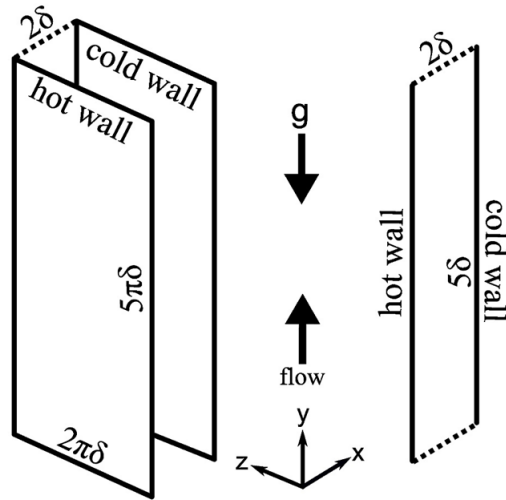
Figure 2.1: Computational Domain for DNS of Kasagi and Nishimura [12] (left) and RANS (right)

Using this finite-volume grid, the coupled heat transfer and fluid flow is resolved using the RANS framework within ANSYS [R] Fluent by ANSYS Fluent et al. [47]. Mimicking the technical approach of Kasagi and Nishimura [24], the thermophysical properties are assumed to be

10

constant over the prescribed temperature conditions while the effect of buoyancy is modeled using the Boussinesq approximation. For a stationary, Newtonian fluid, the conservation equations for mass (continuity), linear momentum, and thermal energy transport can be expressed as:

Continuity:

$$\frac{\partial \overline{u}_i}{\partial x_i} = 0 \tag{2.1}$$

Momentum:

$$\overline{u}_j \frac{\partial \overline{u}_i}{\partial x_j} = \frac{\partial}{\partial x_J}\left[-\frac{\overline{p}}{\rho}\delta_i + \nu\frac{\partial \overline{u}_i}{\partial x_j} - \overline{u'_i u'_j} \right] - g\beta\Delta\overline{T} \tag{2.2}$$

Energy:

$$\overline{u}_i \frac{\partial \overline{T}}{\partial x_i} = \frac{\partial}{\partial x_j}\left[\alpha\frac{\partial \overline{T}}{\partial x_j} + \overline{u'_i T'} \right] \tag{2.3}$$

Equations (1), (2), and (3) are nearly indistinguishable from the classical Navier-Stokes equations while the new terms in the linear momentum and energy conservation relationships, $(u'_i u'_j)$ and $(u'_i T')$, respectively, represent the contributions of turbulence to the transport of each variable. To resolve this interconnected system of equations, additional closure models are required to characterize the Reynolds stress $(u'_i u'_j$) and turbulent heat flux $(u'_i T')$ throughout the computational domain.

The present investigation focuses on the most common type of RANS-based formulations: two-equation eddy viscosity models. In these turbulence treatments, the isotropic eddy viscosity hypothesis of Boussinesq is used to relate the Reynolds stress tensor to the mean velocity gradients

via the following relationship:

$$\overline{u_i' u_j'} = -\nu_t \left(\frac{\partial \overline{u_i}}{\partial x_j} + \frac{\partial \overline{u_j}}{\partial x_i} \right) + \frac{2}{3} k \delta_{ij} \tag{2.4}$$

where ν_t represents a turbulent kinematic viscosity and k is the scalar turbulence kinetic energy, a homogenized measure of the entire turbulent energy spectrum. Similarly, the turbulent heat fluxes are calculated using the simple gradient diffusion hypothesis (SGDH):

$$\overline{u_i' T'} = -\frac{\nu_t}{Pr_t} \left(\frac{\partial \overline{T}}{\partial x_i} \right) \tag{2.5}$$

where Pr_t is the turbulent Prandtl number, typically valued from 0.8 to 0.9 for air. In this framework, two additional transport relationships are used to track the evolution of k and its local rate of dissipation (ϵ):

$$\underbrace{\overline{u_i} \frac{\partial k}{\partial x_i}}_{\text{Advection}} = \underbrace{\frac{\partial}{\partial x_j} \left[\left(\nu + \frac{\nu_t}{\sigma_k} \right) \frac{\partial k}{\partial x_j} \right]}_{\text{Transport}} + \underbrace{P_k}_{\text{Production}} + \underbrace{G_k}_{\text{Buoyancy}} \underbrace{-\epsilon}_{\text{Dissipation}} + \underbrace{D}_{\text{Damping}} \tag{2.6}$$

$$\underbrace{\overline{u_i} \frac{\partial \epsilon}{\partial x_i}}_{\text{Advection}} = \underbrace{\frac{\partial}{\partial x_j} \left[\left(\nu + \frac{\nu_t}{\sigma_\epsilon} \right) \frac{\partial \epsilon}{\partial x_j} \right]}_{\text{Transport}} + \underbrace{C_{1\epsilon} f_1 \frac{\epsilon}{k} P_k}_{\text{Production}} + \underbrace{C_{1\epsilon} C_{3\epsilon} \frac{\epsilon}{k} G_k}_{\text{Buoyancy}} \underbrace{- C_{2\epsilon} f_2 \frac{\epsilon^2}{k}}_{\text{Dissipation}} + \underbrace{E}_{\text{Damping}} \tag{2.7}$$

It should be noted that the direct production of turbulence from buoyancy (G_k) is modeled using the SGDH, which does not contribute to the overall budget for the scalar turbulence kinetic energy in the current analysis due to the fully developed condition created by the periodic boundary conditions. Based on the observations from the original DNS calculations of Kasagi and Nishimura [24], as well as the RANS model assessments of Kim et al. [48], this assumption will be inconsequential due to the term's negligible magnitude. Using these transport variables, an additional constitutive expression is used to compute the turbulent viscosity:

$$\nu_t = C_\mu f_\mu \frac{k^2}{\epsilon} \tag{2.8}$$

where f_μ is a model-dependent damping function which serves to control the relationship between ν_t and the computed turbulence parameters. Four different turbulence models are investigated in the present investigation: the traditional two-layer k-ϵ model (KE) of Launder and Spalding [49] Wolfshtein et al. [50] Jongen [51] and three low-Reynolds-number formulations (Lam and Bremhorst [44] (LB), Yang and Shih [43] (YS), and Speziale et al. [52] (AB)). The model constants for each of these models ($C_{1\epsilon}$, $C_{2\epsilon}$, C_μ, σ_k, and σ_ϵ) are listed in Table 2.1 while the low-Reynolds-number damping functions for all four formulations are provided in Table 2.2.

Table 2.1: Closure constants for each RANS model

Model	C_μ	$C_{\epsilon1}$	$C_{\epsilon2}$	σ_k	σ_ϵ
KE	0.09	1.44	1.92	1.00	1.3
LB	0.09	1.44	1.92	1.00	1.3
YS	0.09	1.44	1.92	1.00	1.30
AB	0.09	1.45	1.83	1.00	1.40

Table 2.2: Damping functions for each RANS model

Model	f_μ	f_1	f_2
KE	1	1	1
LB	$\left[1 - exp\left(-0.0165 Re_y\right)\right]^2\left(1 + \frac{20.5}{Re_t} bigg)\right)$	$1 + \left(\frac{0.05}{f_\mu}\right)^2$	$1 - exp\left(-Re_t^2\right)$
YS	$\left(1 + \frac{1}{\sqrt{Re_t}}\right)\left[1 - exp\left(\begin{array}{c} -1.5 \times 10^{-4} Re_y \\ -5.0 \times 10^{-7} Re_y^3 \\ -1.0 \times 10^{-10} Re_y^5 \end{array}\right)\right]^{0.5}$	$\frac{\sqrt{Re_t}}{1+\sqrt{Re_t}}$	$\frac{\sqrt{Re_t}}{1+\sqrt{Re_t}}$
AB	$tanh(0.0008 Re_k)\left(1 + \frac{4}{Re_t^{0.75}}\right)$	1	$\left[1 - \frac{2}{9} exp\left(-\frac{Re_t^2}{36}\right)\right]\left[1 - exp\left(-\frac{Re_k}{12}\right)\right]$

Each of the transport equations are discretized spatially using second-order accurate finite-volume schemes; collocated upwind schemes are applied to all advection terms while diffusion is treated with central differencing. A periodic mass flow condition is imposed to achieve a constant Reynolds number of 4358, which corresponds to $Re_\tau = 150$ (consistent with the DNS computations of Kasagi and Nishimura [12]). Translational periodicity is applied to both stream-wise boundaries of the channel ($y = 0$ and $y = 5\delta$) to mimic the fully developed flow conditions of the original DNS calculation. Constant temperature conditions are applied at each wall of the channel; the right surface ($x = \delta$) is prescribed at a lower temperature than the left wall ($x = -\delta$), which permits the analysis of both buoyancy-aided and opposed flow regimes simultaneously. The thermal boundary condition for the RANS simulations was set to be constant wall temperature with a ΔT of $1°C$ in order to maintain the accuracy of the Bousinessq approximation while the Grashof number is set to 9.6×10^5 by artificially adjusting the gravitational constant. In this fashion, the right side of the computational domain ($x > 0$) is buoyancy-opposed while the flow on the left side ($x < 0$) of the channel is aided by buoyancy. To resolve the pressure-velocity coupling within the Reynolds-averaged Navier-Stokes equations, the SIMPLE algorithm of Patankar [53], in conjunction with the methods of Rhie and Chow [54], is employed. The discretized system of equations is resolved iteratively using an algebraic multigrid (AMG) solver until the RMS residual of each transport relationship falls below a 10^-9 criterion. Even with the use of a coupled solver in ANSYS Fluent, the transport equation for temperature is solved segregated from the velocity and pressure fields. Once the velocity and turbulence fields are resolved, a custom user-defined scalar transport function defined in accordance with Equation (3) is computed to track the temperature throughout the domain.

2.3   Numerical Uncertainty

Errors introduced by a particular turbulence model cannot be properly estimated without first addressing the various numerical errors. Although uncertainty quantification for numerical results remains an ongoing field of study, important guiding principles are captured in the ASME Verifica-

tion and Validation 20 Standard of Mechanical Engineers [55], and this serves and the motivation for the current study. The final goal of a full validation study would be to assess the model form error, which speaks to the adequacy of a given modeling approach and the impact of the assumptions tied to that model. Experimental errors one might normally include are not considered here as we take the DNS data to represent the true physics without any uncertainty. Numerical errors on the other hand must be quantified before a useful validation study can be conducted. These include the discretization error induced from discretizing the underlying partial differential equations and the iteration error, which stems from the requirement to iteratively solve the system of transport relationships. By forcing conservative requirements on residuals, the iteration error can be shown to be much smaller than the discretization error, and therefore neglected. In the current study, each simulation is subjected to stringent convergence criteria (RMS residual of 10-9 for every discretized equation). Additionally, the iterative solution algorithm employs a double precision solver, which effectively eliminates potential truncation errors in each numerical SRQ. By taking the above precautions, it is expected that the effects of iteration and round-off error are negligible in comparison to the more heavily scrutinized discretization error Oberkampf and Roy [56]. The discretization error is determined by performing a grid convergence study. This is done by running the simulation on two or more successively finer grids. As the grid is refined, the spatial discretization error should, in theory, asymptotically approach zero. In practice, grid refinement is limited based on computational capabilities and is performed until the difference reaches an acceptable value, which is carried forward as the numerical uncertainty. Based on the method proposed by Roache [57], with the practical modifications introduced by Oberkampf and Roy [56] the following transcendental relationship is evaluated to determine the observed order of convergence (o) between grid refinements:

$$r_{12}^o \frac{f_2 - f_1}{r_{12}^o - 1} - \frac{f_3 - f_2}{r_{23}^o - 1} = 0 \tag{2.9}$$

where the subscripts 1, 2, and 3 refer to quantities extracted from the coarse, medium, and fine density grids, respectively, and r is the grid refinement between both referenced meshes. Any

differences between the observed and theoretical orders of convergence come from boundary conditions, grid quality, non-linearity in the solution, and other factors. Using the observed order of convergence, the grid convergence index (GCI) at each location can be calculated using:

$$GCI = 2\sigma = \frac{F_s}{r_{23}^o - 1}|f_3 - f_2| \tag{2.10}$$

The factor of safety is nominally set to 1.25 if the observed order of convergence is within 10% of the order of the employed numerical schemes (2nd order in this investigation). If this condition is not met, the factor of safety is set to three and o is reduced to 0.5. Using this method to define a factor of safety results in a conservative estimate of the actual discretization uncertainty. By defining the discretization uncertainty in this manner, the GCI has the same physical units as the SRQ. To perform the GCI in this study, the skin friction coefficient and Nusselt numbers are calculated on three successive grids. The resulting data is used to construct an uncertainty band which can be used to approximate the discretization error. This uncertainty is propagated through the error metric as described in the next section. In the current study, three grids are constructed using a constant refinement factor of four. From the outlined base mesh configuration (120×200), a coarser mesh featuring 6,000 elements (60×100) and finer mesh with 96,000 (240×400) finite-volume cells are generated for the GCI analysis. Based on this approach, the relative discretization uncertainties (GCI_ϕ/ϕ) are found for global metrics such as skin friction coefficient (C_f) and Nusselt number (Nu). Results of this analysis show average and maximum relative uncertainties on the order of a few percent across all turbulence models. The results that follow are extracted from the original base mesh and the calculated GCI results, which represent a 95% confidence interval around those values, will be carried forward in each presented global SRQ.

2.4 Model Error Assessment

To better understand a model's capability to predict a given flow condition, a quantitative analytic approach can provide simple metrics for easy comparison. Many different methods exist to quantitatively compare data sets, though no standard approach exists. Mean relative error (MRE)

is a conventional method of error analysis but is unbounded. This causes problems when the SRQ is close to zero (e.g., velocity near a wall) and becomes undefined when the true value is zero (e.g., velocity gradient in the center of a channel). Using solely the ratio of the predicted and true value as a measure of accuracy was proposed by Kitchenham et al. [58]. This method is also asymmetric, unbounded, and can be undefined when the true value is zero. Mean absolute percentage error (MAPE), which uses a normalized sum, can be skewed drastically by true values close to zero and is also undefined as the true value approaches zero. Armstrong and Forecasting [59] and Makridakis [60] discussed another issue of using MAPE. Inherently, it is not symmetric when swapping actual and predicted values in the formulation. This stems from interchanging the value in the denominator, thus dividing by a different number. Symmetric mean absolute percent error (SMAPE), as proposed by Armstrong and Collopy [61], addresses this issue by replacing the denominator with the mean of the true and predicted values. If one value is dominant or zero, this is reflected in both the numerator and the denominator. This causes a limit of -2 or $+2$, depending on the signs of the true and predicted values. While this can lead to unwanted limiting at the error bounds if the true value is zero and the predicted value is very close to zero, it circumvents issues often encountered with other methods. Törnqvist et al. [62] investigated multiple approaches, including those mentioned here, and concluded that the natural logarithm of the ratio between the actual and predicted value was a good choice for determining relative change. However, this method is limited by the need for positive values and is also unbounded.

For this investigation, SMAPE is used because it has an upper and lower bound and is not limited to only positive quantities. All models used in this investigation are subject to the advantages and limitations of the SMAPE approach. Although this introduces some subjectivity into a quantification of error, the method provides a clear quantitative metric that can be easily compared across modeling approaches. In quantifying the difference between DNS and any simulation, the SRQs' magnitudes, as well as the gradient of their profiles, are used as validation metrics. The

17

SMAPE method is applied to each extracted SRQ according to:

$$\phi_i = \frac{P_i - A_i}{|A_i| + |P_i|} \tag{2.11}$$

This metric (ϕ) is determined at each physical location (i) and can be calculated for any arbitrary SRQ. The true or accepted value (A_i) must be at the same physical location as the predicted value (P_i) for the comparison to be one-to-one. The result of Equation (11) provides a profile of the model error for a given SRQ relative to the true or accepted value. Taking this process, a step further, the gradient of each accepted and predicted profile is determined numerically and is subjected to the same procedure:

$$\nabla\phi_i = \frac{\nabla P_i - \nabla A_i}{|\nabla A_i| + |\nabla P_i|} \tag{2.12}$$

The gradient of the profiles is calculated using a second-order central differencing scheme for the interior points and either a forward or backward differencing at the boundary walls, depending on the location within the channel. This provides a second metric to characterize the performance of each RANS model against the benchmark DNS values. The first quantity provides the error in the magnitude of the SRQ and the second provides the error in the magnitude of the slope of the SRQ. In order to obtain a global value representative of the relative error, the sums of both metrics are taken across the total number of extracted points, m:

$$\xi\phi = \sum_{i=1}^{m} |\phi_i| \tag{2.13}$$

and

$$\xi\nabla\phi = \sum_{i=1}^{m} |\nabla\phi_i| \tag{2.14}$$

Both metrics provide valuable insight into how accurately a turbulence model captures the physics within the differentially heated plane channel. Inspection of these two metrics side-by-side in this unique format enables a direction comparison of both the magnitude of the SRQ and shape of its profile. 2.2 is an example of how these metrics can be used to demonstrate the relative error

between a model's predictions of the magnitude and gradient of a given SRQ and how this error differs from model to model. In this example problem, Models 2 and 3 yield the best predictions of the magnitude of the SRQ, but the worst predictions of the shape of its profile. Here, Models 2 and 3 would be able to accurately capture the SRQ of interest, but do not faithfully replicate the physics of the problem. Meanwhile, Models 1 and 4 are relatively better at predicting the gradient of the profile but have markedly increased error in the prediction of the SRQ magnitude. In this scenario, Models 1 and 4 may offer a better prediction of the problem physics but are unable to capture the magnitude of the SRQ of interest. While this may not be acceptable from a turbulence modeling perspective, it indicates that the model has value due to its ability to adhere to the general trend of the benchmark quantities. These inspections are made easy by maintaining the same range on either axis, allowing for the domain to be divided into two equal sections. Models appearing below and to the right of the $45°$ line have relatively better predictions of the gradient than the magnitude of a given SRQ. The opposite is true of models above and to the left of the diagonal black line. It is important to note that the error metric is defined by the sum of the SMAPE at each point and has not been normalized any further.
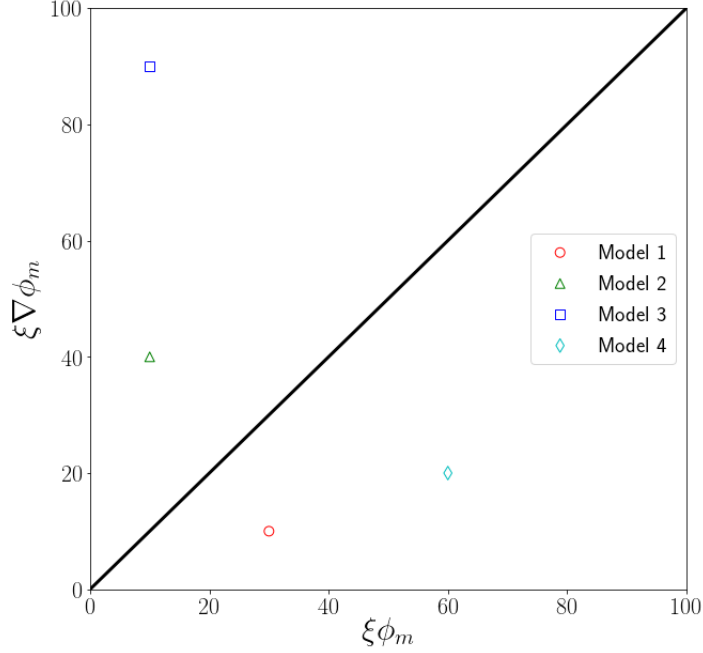
Figure 2.2: Example of error metric comparison for different models

2.5 Hydrodynamic Results

In this flow configuration, there exists an asymmetry in $\overline{u}^*$ $\left(\overline{u}^*/U_bulk\right)$ due to the differential thermal boundary conditions. In both the buoyancy-aided and opposed regions, there is a deviation from the normal logarithmic region that would exist in an isothermal or forced convection flow regime. In the buoyancy-aided region, $\overline{u}^*$ is increased while in the buoyancy-opposed region, the opposite is true. 2.3 shows the comparison between the averaged velocity profiles, $\overline{u}^*$, calculated from the various RANS models and the DNS results from Kasagi and Nishimura [24] in both the buoyancy-aided and opposed regions. Figure 4 shows the error metric ξ for $\overline{u}^*$ on the x-axis and $\nabla\overline{u}^*$ on the y-axis. Due to the nature of SMAPE, the total error is bounded by the number of points used in the analysis. In this study, each side of the domain (buoyancy-aided and opposed) consists of 60 physical locations for each SRQ sample; therefore, each metric can range from 0 to 60, where 0 would be an exact prediction and 60 would be complete deviation from the benchmark DNS cal-culations. This enables an intuitive inspection of the performance of each turbulence model for a

given metric using the DNS results as a baseline. Used in conjunction with the profiles in Figure 3, a new level of inspection is achieved to determine how well a model performs in a given prediction. From a simple visual inspection, it is challenging to definitively conclude which model is truly the best. The AB results for example, seem the have the lowest error in the buoyancy aided profile for $x^+ > 10$, but other models appear to do better in the near wall region. Additional clarity can be gained by analyzing the data in Figure 4, where all models are seen to yield roughly the same error in $\overline{u}^*$, but exhibit a larger spread when observing errors in $\nabla \overline{u}^*$. When considering results from both the magnitude and shape of the profiles, it becomes clear that LB and YS provide the best predictions (nearly identical) for buoyancy aided. It is also clear from both figures that KE is unable to adapt to the presence of buoyancy in the aided region. In the buoyancy-opposed region, the model grouping is more consistent compared to the spread in the aided predictions. From Figure 4, YS most accurately captures both $\overline{u}^*$ and $\nabla \overline{u}^*$, with AB following closely behind. Though LB has a similar prediction of $\nabla \overline{u}^*$ as YS, the prediction of $\nabla \overline{u}^*$ is noticeably less accurate than YS and AB. Similarly, KE has a reasonable prediction of $\overline{u}^*$ in the buoyancy-aided region, but is unable to accurately predict $\nabla \overline{u}^*$.
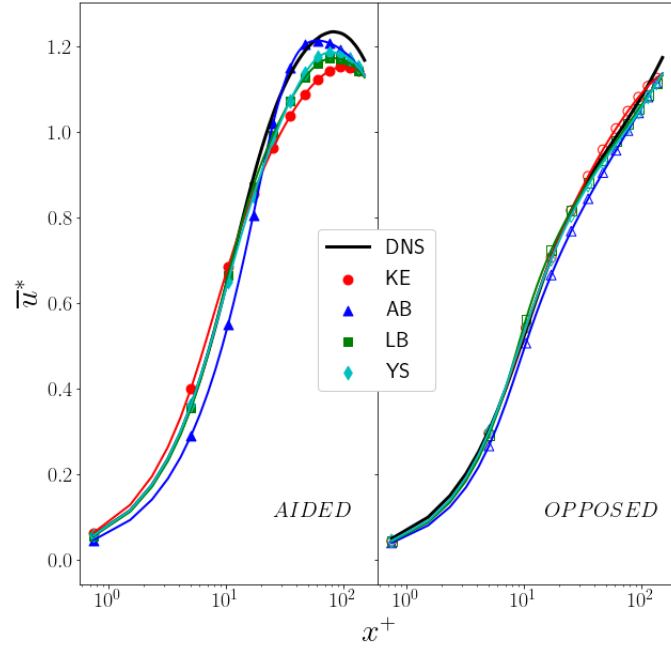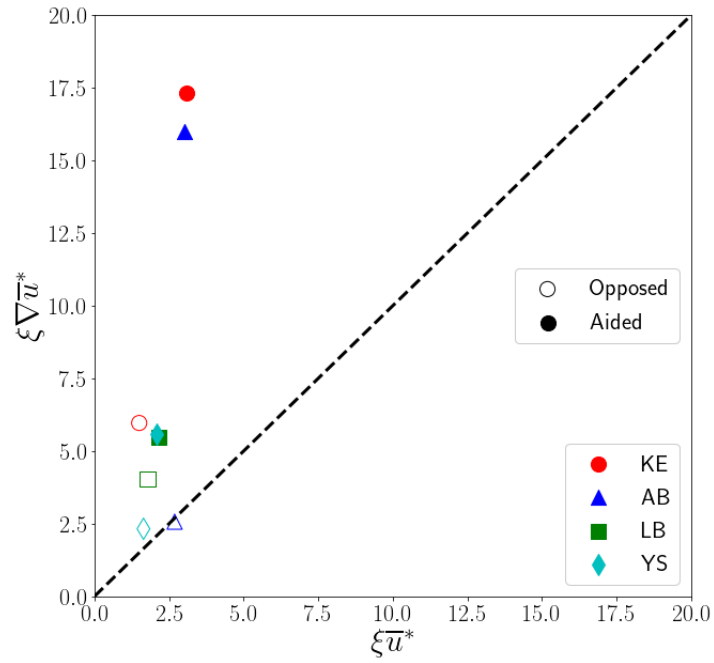
Figure 2.3: Comparison of mean velocity profiles

Figure 2.4: Error metrics for mean stream-wise velocity ($\overline{u}^*$) profiles

22

Figure 2.5 shows the comparison between model predictions of the stream-wise Reynolds stress, $\overline{u'u'}^*$. In the buoyancy-aided region, the Reynolds stress is suppressed relative to the buoyancy-opposed region due to the complex interaction between buoyancy and turbulence. In the buoyancy-aided region at the onset of mixed convection, turbulence is suppressed by a disruption to the burst-sweep process that occurs in the near-wall region where turbulence is generated. With this decrease in turbulence production, a similar reduction of the Reynolds stresses is observed in this region. With increasing buoyancy, the turbulence is further reduced to a minimum before undergoing a recovery (starting around $x^+ = 75$ for the DNS results). The opposite is true in a reversed orientation where the bulk flow is opposed by buoyancy. In this configuration, heat transfer is enhanced with increasing influence of buoyancy. In order to predict this behavior, linear eddy viscosity models employ the use of the Bousinessq approximation shown in Equation (4). This particular flow is considered one-dimensional ($\overline{v}^* = 0$) due to the geometry and the flow being stationary as well as fully developed. This causes the normal Reynolds stresses to be equal ($\overline{u'u'}^* = \overline{v'v'}^*$) because they are solely defined by the term $-2/3k\delta_{ij}$ as the other term in Equation (4) is zero. Using this definition presents an obvious problem: the models are unable to capture any anisotropy present in the flow.

In the buoyancy-aided region, it is apparent that AB is unable to accurately predict $\overline{u'u'}^*$. The model is overly sensitive to the presence of buoyancy and $\overline{u'u'}^*$ in the buoyancy-aided region is greatly suppressed. Figure 2.6 shows the error metric comparison for each model for $\overline{u'u'}^*$ and $\nabla\overline{u'u'}^*$. KE has the best prediction of $\overline{u'u'}^*$ in the buoyancy-aided region, but suffers in its prediction of $\nabla\overline{u'u'}^*$ in comparison to LB and YS, which have slightly worse predictions of $\overline{u'u'}^*$ but improved predictions of $\nabla\overline{u'u'}^*$. In the buoyancy-opposed region, the model grouping is much closer with LB and YS performing the best in both $\overline{u'u'}^*$ and $\nabla\overline{u'u'}^*$.

Figure 2.5: Comparison of mean normal Reynolds stress profiles
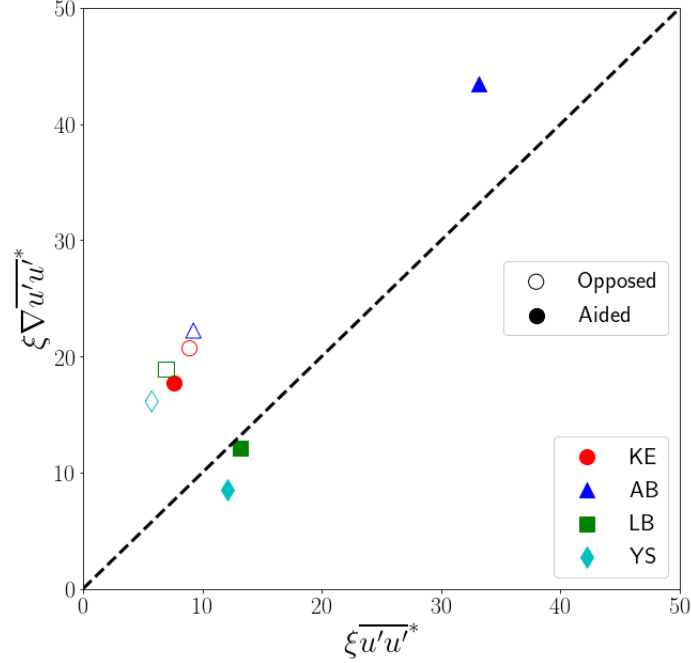
Figure 2.6: Error metrics for mean normal Reynolds stress profiles ($\overline{u'u'}^*$) profiles

Similar to the stream-wise Reynolds stress, the shear stress is reduced in the buoyancy-aided region while it is increased in the buoyancy-opposed region. Figure 2.7 shows the comparison between models for the Reynolds stress, $\overline{u'v'}^*$, and Figure 2.8 shows the error metric ξ for $\overline{u'v'}^* *$ on the x-axis and $\nabla \overline{u'v'}^*$ on the y-axis. In the buoyancy-aided region, KE and AB have poor predictions of $\overline{u'v'}^*$ with AB also having a poor prediction of $\nabla \overline{u'v'}^*$. YS and LB both have accurate predictions of $\overline{u'v'}^*$ and $\nabla \overline{u'v'}^*$ in this region. From the previous figures comparing the models, KE and AB are not capable of capturing the effect of buoyancy in the buoyancy-aided region, while LB and YS are able to maintain accurate predictions in this region. In the buoyancy-opposed region, the model grouping is once again much closer in comparison to the buoyancy-aided region. It is notable that KE performs the worst in the fully turbulent core ($x^+ > 30$) but recovers in the near wall region ($x^+ < 10$). AB performs poorly near the wall and has a much better prediction in the fully turbulent core. YS and LB have more reasonable predictions throughout the entirety of the buoyancy-opposed side of the channel. Combining these predictions, it is concluded that the YS

25

model provides the best predictions of the hydraulic SRQs, with KE, LB, and AB following behind in decreasing performance.
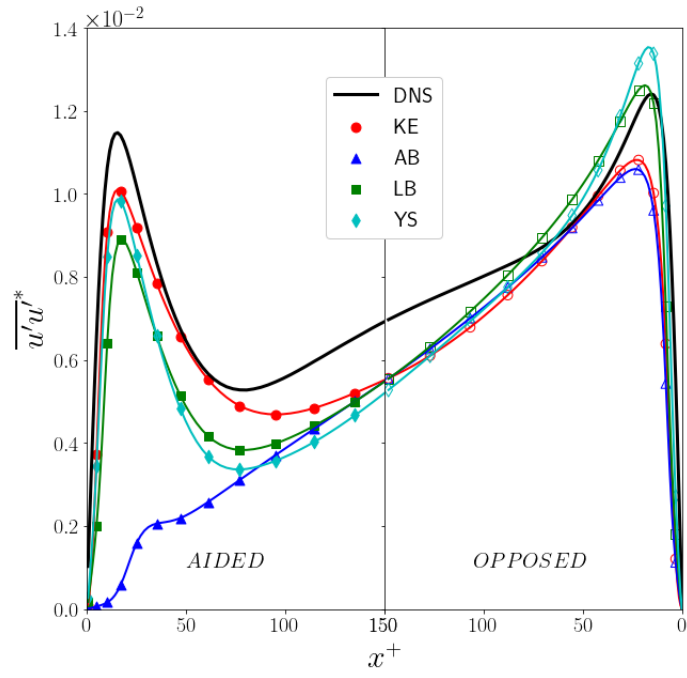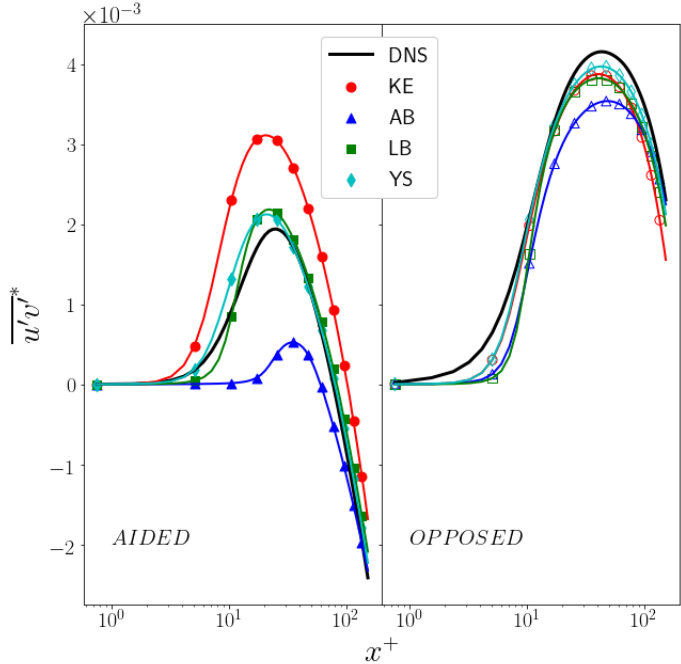

Figure 2.7: Comparison of mean Reynolds shear stress profiles
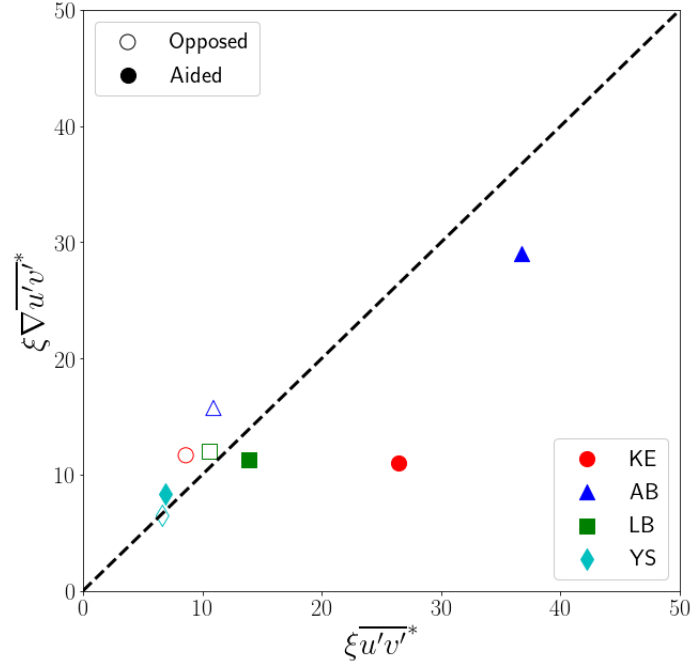
Figure 2.8: Error metrics for mean Reynolds shear stress profiles ($\overline{u'v'}^*$) profiles

The effect of buoyancy is not limited to thermal SRQs; similar trends are observed in the predicted skin friction coefficient (C_f), a dimensionless measure of the drag force imparted on the fluid by the heated surface. This is an important measure of the wall shear stress, which is a measure of the near-wall velocity gradient. In the buoyancy-aided region, the mean velocity is intensified near the wall due to the beneficial effects of buoyancy, resulting in a larger skin friction coefficient. The reverse is found at the opposite wall, where the effects of buoyancy oppose the bulk flow direction, creating less drag along the surface. Figure 2.9 shows the results for the calculated skin friction coefficient. The results vary in the aided region with LB providing the best prediction followed closely by YS. In comparison, both KE and AB generate inaccurate predictions. In the buoyancy-opposed region, LB and KE provide highly accurate predictions with AB and YS following close behind.
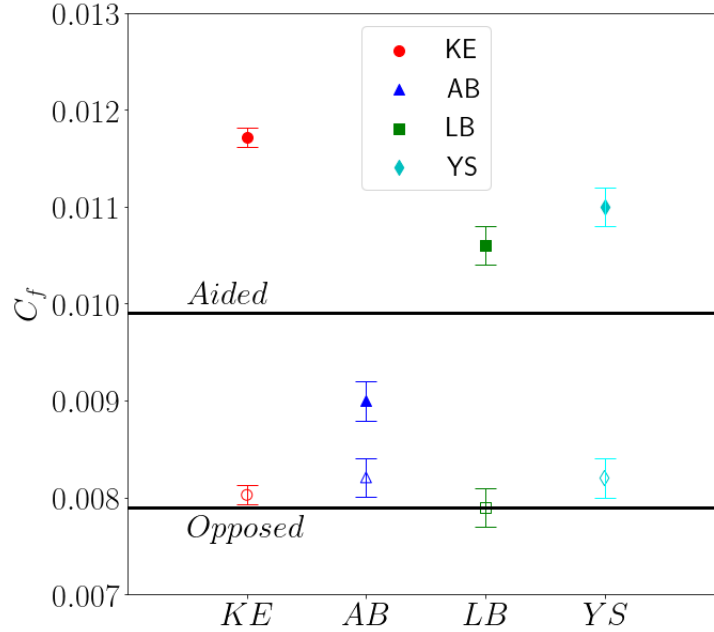
Figure 2.9: Skin friction coefficient comparison between RANS models.

2.6 Thermal Results

In the presence of buoyancy, the mean temperature profile becomes asymmetric. The temperature gradient in the buoyancy-aided region is increased, while the opposite is true for the buoyancy-opposed region. This is due to the heightened advection term on the left hand side of Eq. 3; in the buoyancy-aided region, the stream-wise velocity gradient is larger, resulting in a heightened transfer of thermal energy. Conversely, the stream-wise velocity reduction in the buoyancy-opposed region retards the transfer of heat, resulting in the shallower profile. Figure 2.10 and Figure 2.11 show the profiles and related error metrics for $\overline{T}^*$. From these figures, KE is not sensitive to the presence of buoyancy whereas AB is overly sensitive. In the buoyancy-aided region, YB and LS provide similar predictions for both magnitude and shape of $\overline{T}^*$. In the buoyancy-opposed region, YS has a clear advantage over LB in the prediction of $\overline{T}^*$.
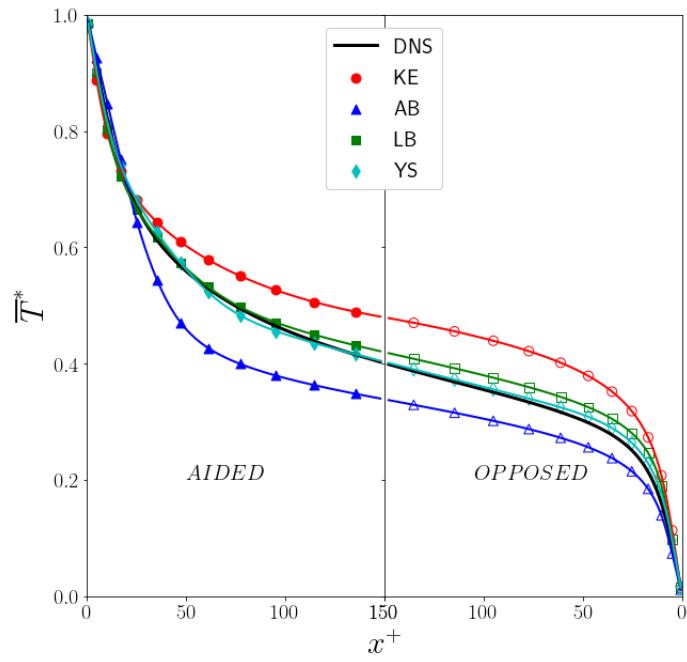
Figure 2.10: Comparison of mean temperature profiles
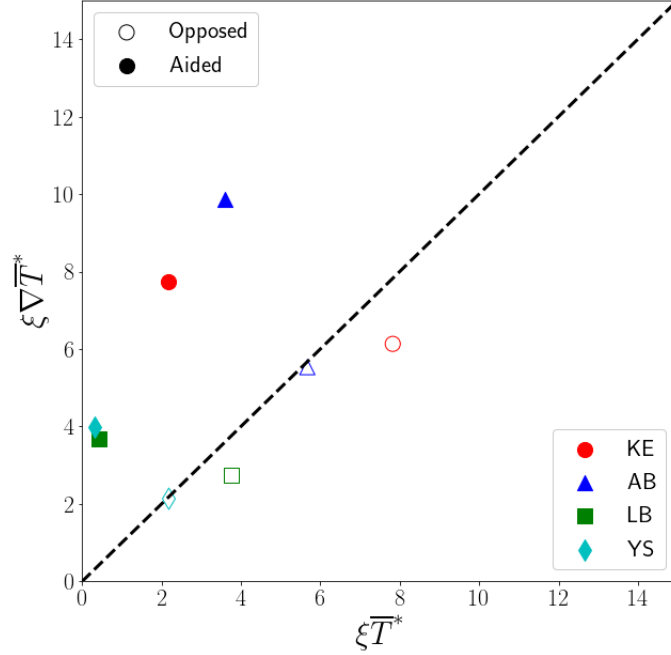
Figure 2.11: Error metrics for mean temperature ($\overline{T}^*$) profiles

A major component of the temperature calculation is determining the magnitude of the turbulent heat flux. As with the Reynolds stresses, the turbulent heat fluxes require additional closure models. Methods for closure range from more complex multi-equation models to the more simplistic SGDH approach used here. The advanced formulations are often derived for thermally driven buoyant flows, but normally yield marginally improved results and are not widely available in most CFD applications. Therefore this current study focuses on the readily available more simplistic SGDH approach (Eq. 5). SGDH captures the heat fluxes using a relationship that is based on the gradient of temperature. In fully developed flows the gradient of the mean temperature is zero in the stream-wise direction resulting in SGDH being unable to predict $\overline{u'T'}^*$. Figure 2.12 and Figure 2.13 show comparisons between model predictions of $\overline{v'T'}^*$. In the buoyancy-aided region, YS and LB have the best predictions of $\overline{v'T'}^*$, but have unwanted behavior starting at $x^+ > 10$ that contributes some error to the prediction of $\nabla\overline{u'T'}^*$. From this, the deduction can be made that as long as there is a reasonable prediction of the radial turbulent heat flux, $\nabla\overline{u'T'}^*$, that the temper-

30

ature, $\overline{T}^*$, will also be accurately captured for this particular flow condition. This justifies the use of SGDH in this particular problem. LB shows similar behavior in this region, but it is markedly less pronounced than YS, giving a better prediction of $\nabla\overline{v'T'}^*$. KE has a reasonable prediction of $\nabla\overline{u'T'}^*$, but over predicts $\overline{u'T'}^*$. Throughout this region, AB is unable to capture the behavior for $\overline{u'T'}^*$ and $\nabla\overline{u'T'}^*$. In the buoyancy-opposed region, YS has the best prediction of $\overline{v'T'}^*$, but the worst prediction of $\nabla\overline{u'T'}^*$. The other models follow in a similar fashion with LS, AB, and KE generating increasingly accurate predictions of $\nabla\overline{u'T'}^*$ and decreasingly accurate predictions of $\overline{u'T'}^*$, respectively.
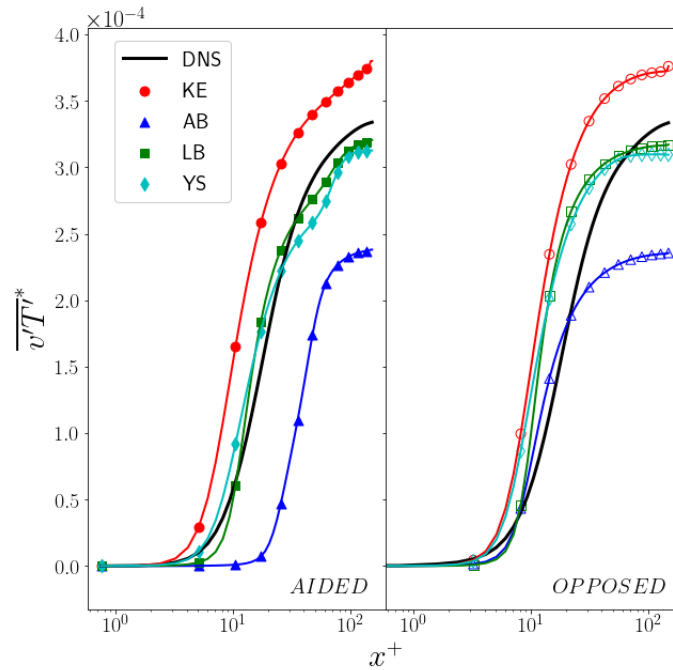
Figure 2.12: Comparison of mean turbulent heat flux profiles
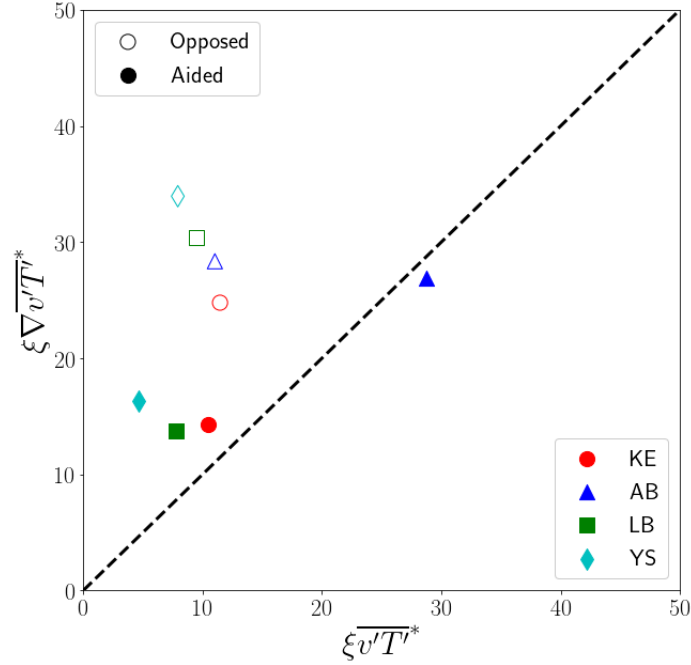
Figure 2.13: Error metrics for mean turbulent heat flux profiles ($\overline{v'T'}^*$) profiles

Additional analysis can be conducted for global metrics as well. The Nusselt number is a representation of the ratio of convective to conductive heat transfer mechanisms at the boundary of the fluid. Therefore, the Nusselt number is proportional to the convective strength of the flow and the challenge with CFD modeling (specifically RANS) is characterizing the change in Nu with buoyancy as it both affects the mean and turbulent flow characteristics simultaneously. Figure 2.14 shows the calculated Nusselt number from DNS and the chosen RANS models for both buoyancy aided and opposed configurations. In the presence of buoyancy in the aiding region, the convective heat transfer is drastically reduced, owing to the decreased turbulent shear stress in this region. Both YS and LB accurately predict this phenomenon. KE has a large over prediction of the Nusselt number in this region, while AB has a sizeable under prediction of the Nusselt number. In the buoyancy-opposed region, each model provides a reasonable prediction of the Nusselt number with YS being a slight outlier with the largest over prediction. These characterizations are important to understand for modelers desiring to quantify model form uncertainty. For example, considering a

32

transient flow that transitions from buoyancy opposed to buoyancy aided flow, one would expect the KE model to overestimate the heat transfer performance and thereby predicting a lower temperature or heat flux in a particular application.
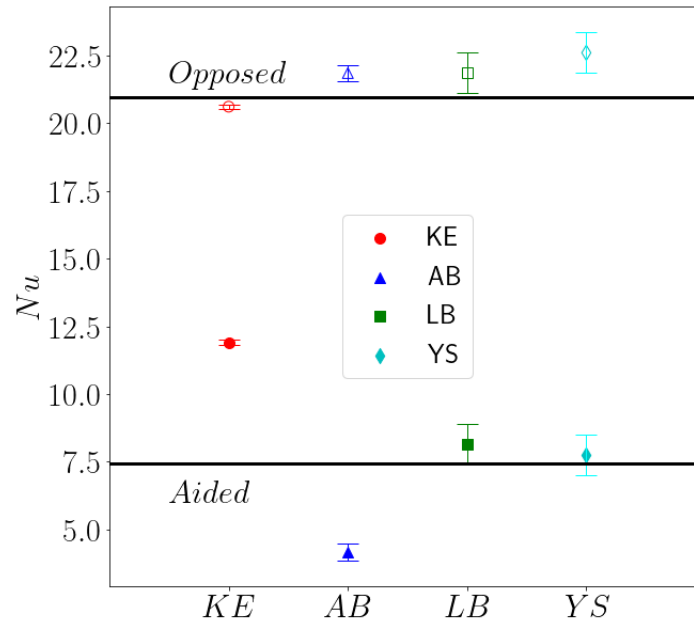
Figure 2.14: Comparison of calculated Nusselt numbers for each RANS model

2.7 Turbulence Kinetic Energy Budgets

From the investigation performed here, it is clear that LB and YS are the two most capable models that most accurately predict both buoyancy aided and opposed mixed convection in this flow configuration. This warrants a further look into the performance of these models. It is important to note that in the range of Grashof number considered here, the effect of buoyancy is also indirectly felt through the variation of the shear production in the turbulent kinetic energy budgets. This propagates as a reduction in the Reynolds stresses in the buoyancy-aided region and a comparable increase in the buoyancy-opposed region. Based on analogous observations from Kim, it is anticipated that the effects of buoyancy are predominantly concentrated on variations to the mean

flow characteristics, and not through direct production of turbulent kinetic energy. As shown by Kasagi and Nishimura [24] and later by Kim et al. [48], the production due to buoyancy is negligible for this Grashof number in comparison to the other budget terms.

Figure 2.15 shows the production (top set of profiles) and dissipation (bottom set of profiles) of turbulent kinetic energy for LB and YS. In the buoyancy-aided region, the dissipation at the wall is over predicted, which is not unique to this formulation as both models accurately capture production and dissipation in the fully turbulent core. Both models have slight under predictions in the buoyancy-opposed region. This is true all the wall and throughout the entire cross section of the channel. Figure 2.16 shows the prediction of turbulent diffusion for both models. Each of them under predict the magnitude of the minima and maxima in both buoyancy-aided and opposed regions, and also under predict throughout the buoyancy-aided region. This arises from an under prediction of the turbulence kinetic energy. Figure 2.17 shows the comparison of the viscous diffusion for YS and LB. YS has the better prediction at the wall in both regions, but both models under predict the minima in each side and then settle to similar predictions in the mean flow with values near zero. Overall, both models have relatively similar predictions for all the budget terms discussed here. The differences in these models lies further in their formulation and calibration.
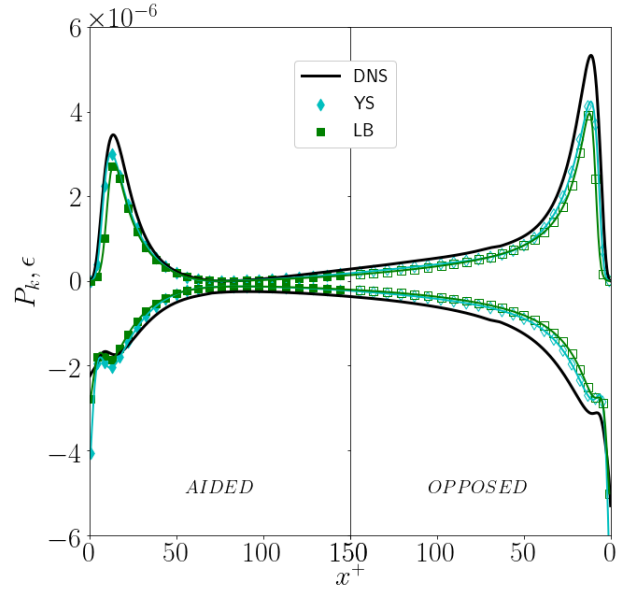
Figure 2.15: Production and dissipation budget terms for LB and YS
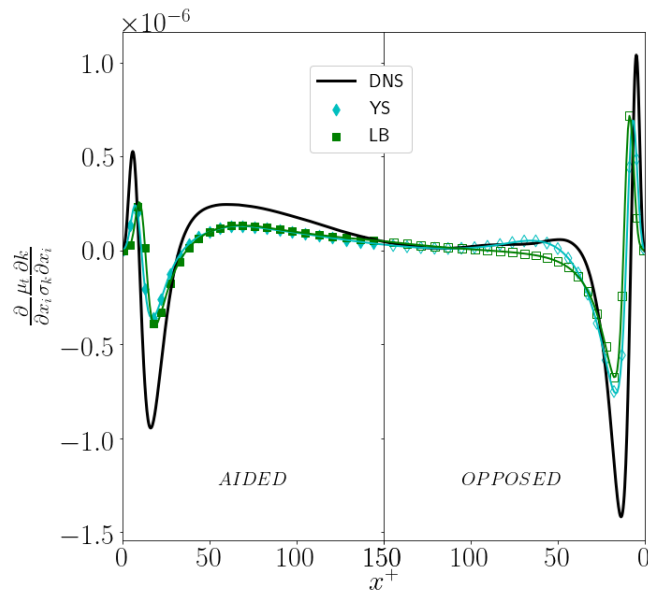
Figure 2.16: Turbulent diffusion budget term for LB and YS

35
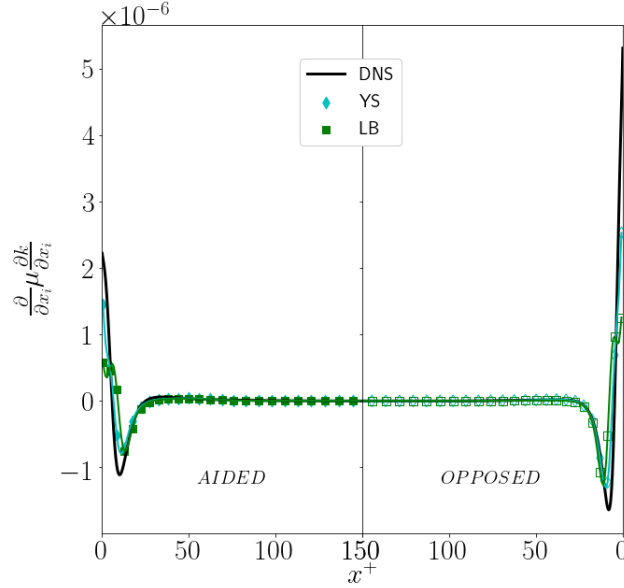
Figure 2.17: Viscous diffusion term for LB and YS

2.8   Sensitivity Analysis of Damping Function (f_μ)

The main difference between low-Reynolds-number eddy viscosity models lies in the formulation of the damping functions, which augment the behaviors of turbulent viscosity (ν_t) , production of dissipation and destruction of dissipation near the wall. Here we focus on the scaling of the turbulent viscosity (ν_t). In general, these models tend towards the behavior of the standard two-layer $k - \epsilon$ model in the free-stream regions. In the formulation of the damping function f_μ, available experimental or DNS data is used to calibrate a given model to improve its accuracy in the prediction of a specific flow or set of flows. This usually involves introducing a set of parameters that can be modified to better fit a given data set. The model constants for YS were calibrated using fully developed turbulent channel flow at a constant $Re_\tau = 180$ to be $A_1 = -1.5 \times 10^{-4}$, $A_3 = -5.0 \times 10^{-7}$, and $A_5 = -1.0 \times 10^{-10}$. The LB formulation is similar with two coefficients, $C_1 = -0.0165$ and $C_2 = 20.5$, being calibrated using experimental turbulent pipe flow data from Hinze [63]. To try to understand the cause of the disparities observed in the YS and LB models, a sensitivity analysis of these coefficients is performed. Because both models accurately capture the

36

shear production relative to the DNS results despite mischaracterizing the mean velocity profile, it is theorized that each model mispredicts the turbulent viscosity relative to the corresponding parameter in the benchmark data set. For each model, a sensitivity analysis was performed using the skin friction coefficients and Nusselt numbers from the buoyancy aided and opposed regions. This was done using a Latin Hypercube approach with a $\pm 10\%$ variation of the nominal values for each parameter.

Figure 2.18 shows the sensitivity of the skin friction coefficients in buoyancy-aided and opposed regions for both YS and LB models with the corresponding DNS values represented by horizontal black lines and the nominal values of each model denoted by black circles. The LB model is more sensitive to the variation of parameters in this selected range with a skew towards the minimum in the aiding flow and a skew towards the maximum in the opposed flow. While YS does show decreased variability in comparison to LB, there still is an evident sensitivity to the change in parameters. This demonstrates the damping functions influence on the gradient of the velocity. Figure 2.19 shows the sensitivity of the Nusselt number in the buoyancy aided and opposed regions for both YS and LB models. Similarly, LB has increased sensitivity in comparison to YS with a large range of calculated Nusselt numbers. Through this sensitivity analysis, both models are sensitive to changes in the parameters used to define their damping function and those changes have a significant impact on the mean SRQs typically measured in a CFD simulation. The impact of this finding underpins the need to further investigate conditions upon which damping functions are based. Additional research is underway to formulate damping functions that perform well in both buoyancy aided and opposed flows, while maintaining accuracy in forced convection conditions.

37
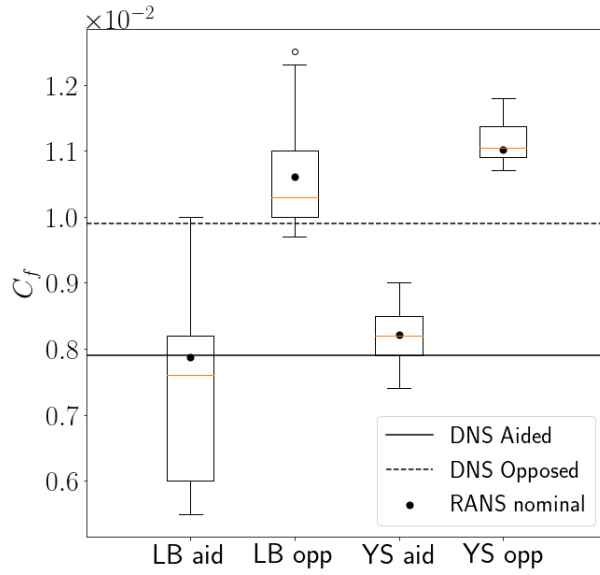
Figure 2.18: Sensitivity analysis of parameters in the damping function (f_μ) and the resulting effect on the skin friction coefficient (C_f) for YS and LB models
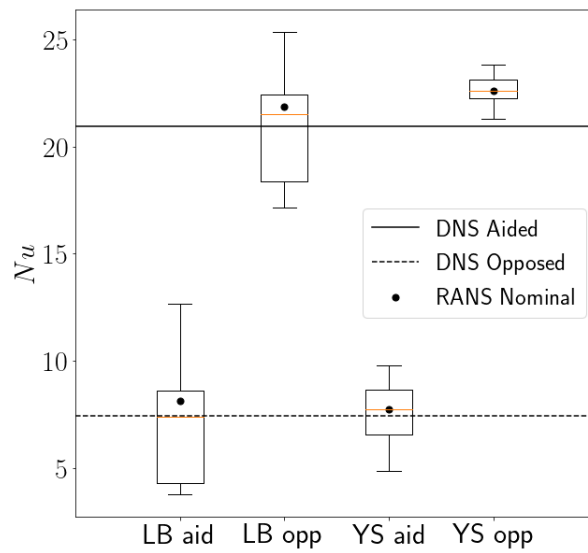
Figure 2.19: Sensitivity analysis of parameters in the damping function (f_μ) and the resulting effect on the Nusselt number (Nu) for YS and LB models

2.9 Section Conclusion

Overall, this framework provides a quantitative yet approachable method of error, sensitivity and calibration analyses, which can be applied across various applications, and accounts for not only error in magnitude but also error in the gradient of the profiles. This provides another level of insight into the physics captured by these various models employed in CFD, and provides a framework for evaluating the usefulness of particular turbulence models in a wider range of flow conditions.

Using this framework, an investigation of various two-equation eddy viscosity models has been performed in order to highlight proficiencies and deficiencies in each of the models. Using a quantitative method that considers error in both shape and magnitude of each SRQ, a more in-depth analysis of these models was made possible. This method can be applied to a range of applications and is not only limited to the scope of this investigation. Comparisons between profiles of any quantity of interest are possible.

Through the investigation, it was observed that two models, LB and YS, outperformed the other two formulations, KE and AB. These two models were able to consistently and accurately predict the mean and turbulent flow characteristics in fully-developed turbulent mixed convection channel flow when compared to validated DNS results from Kasagi and Nishimura [24].

Focusing on these two models, a sensitivity analysis was performed which highlighted the overall sensitivity of the skin friction coefficient and Nusselt number to the variation of parameters in the damping function formulation. Using this approach, future calibrations could be performed to reduce error in a wide range of problems using the parameters of the damping function as the tuning mechanism. Modified damping functions can also be formulated, and their intended capabilities assessed using methods discussed here.

3. LARGE EDDY SIMULATIONS OF BUOYANCY AIDED MIXED CONVECTION PIPE FLOW FOR LEAD BISMUTH EUTECTIC

3.1 Section Summary

Turbulent buoyancy-aided mixed convection of lead-bismuth eutectic (LBE) in a heated cylindrical pipe at Re_d = 5300 is analyzed using large eddy simulations (LES). Specifically, the range containing the onset of mixed convection through full laminarization to the beginning of recovery is simulated in order to better determine the effect on the skin friction coefficient due to the increased presence of buoyancy. This analysis identifies the Richardson numbers that encompass the laminarization regime for LBE at Re_d = 5300 by quantification of the contributions to the skin friction coefficient using the FIK identity. Analysis of the budgets for turbulent kinetic energy show that buoyancy diminishes the shear production to a minimum before recovery begins. The anisotropy of the Reynolds stresses are studied along with a detailed quadrant analysis that reveals how the skin friction is affected by the presence of buoyancy throughout the range of Richardson numbers. Lastly, the resulting flow is visualized using the Q-criterion and vorticity contours.

3.2 Physical Domain and Numerical Method

Turbulent mixed convection in a heated upward pipe flow for LBE (Pr = 0.026) with gravitational effects was simulated using LES. Figure 3.1 shows the computational domain for all simulations in this investigation. In order to determine the gravitational force in relation to the inertial forces, the global Richardson number was utilized. This represents the ratio of the Grashof (Gr) and Reynolds Number (Re_d) defined, respectively, as

$$Gr = \frac{g_i \beta q" D^2}{\lambda \nu^2} \tag{3.1}$$

and

$$Re_d = \frac{\rho U_b D}{\mu} \tag{3.2}$$

The Richardson number is then defined as:

$$Ri = \frac{Gr}{Re_d^2} \tag{3.3}$$

Using DNS from Zhao et al. [27], validation of the current method was done using two cases, namely Ri = 0.017 and 0.040. Targeting additional Richardson numbers inside this range, the aim of this investigation was to elucidate the onset of laminarization and subsequent recovery of turbulence. Results from Ri = 0.017, 0.022, 0.025, 0.030, 0.035 and 0.040 are presented. It will be shown that this effectively describes laminarization and beginning of recovery. In order to be consistent with the DNS study, a constant bulk Reynolds number of 5300 is maintained by a constant pressure gradient in the streamwise direction. The force due to buoyancy is accounted for by the Bousinessq hypothesis and the Richardson number is adjusted by varying the gravity constant, g_i.

All simulations were performed in OpenFOAM V6.0 [64] using a modified solver that implements the aforementioned source terms to properly simulate the given flow. Second order finite volume schemes are used spatially and a second order backward scheme is used temporally in order to obtain the accuracy required for high resolution LES. Similar to the DNS study, a computational

length of 30R is found to be appropriate to conduct this simulation. Cyclic boundary conditions were applied at the inlet and outlet for velocity, pressure and temperature. Initialization was performed with a precursor RANS simulation and a coarse LES to generate fluctuations in the flow domain. This is mapped to the appropriate mesh using the *mapFields* function available in Open-FOAM. The proper mesh resolution is designed with the requirements that the non-dimensional y^+ is 0.2 in the first cell center from the wall. Simulations were run for 100 flow through times ($FT = \frac{L}{U_b}$) to wash out initial simulation conditions. Following this, an additional 200 flow throughs were evaluated and time-averaged to acquire statistically steady converged results. All Data is presented non-dimensionalized by U_b, r and T_b where appropriate for comparison with available DNS.
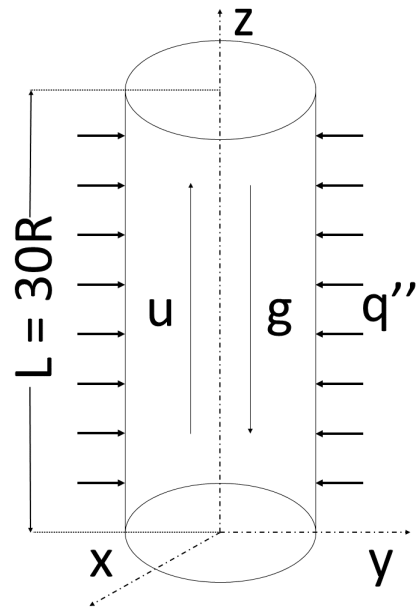
Figure 3.1: Simulation Domain.

3.3 Mathematical Models

3.3.1 Governing Equations

The filtered system of equations governing heat and fluid flow for incompressible fluids are:

$$\frac{\partial \widetilde{u}}{\partial x_i} = 0 \tag{3.4}$$

$$\frac{\partial \widetilde{u}_i}{\partial t} + \frac{\partial}{\partial x_j}\left(\widetilde{u_i u_j}\right) = -\frac{1}{\rho}\frac{\partial \widetilde{p}}{\partial x_i} + \nu \frac{\partial^2 \widetilde{u}_i}{\partial x_j \partial x_j} - \frac{\partial \tau_{ij}}{\partial x_j} - \beta g_i \left(\Delta \widetilde{T}\right) \tag{3.5}$$

$$\frac{\partial \widetilde{T}}{\partial t} + \frac{\partial}{\partial x_j}\left(\widetilde{u}_j \widetilde{T}\right) = \alpha \frac{\partial^2 \widetilde{T}}{\partial x_j \partial x_j} \tag{3.6}$$

where $\tau_{ij} = \widetilde{u_i u_j} - \widetilde{u}_i \widetilde{u}_j$ with $\sim$ representing a grid filtered quantity. The body force from buoyancy is accounted for by the last term in Equation 3.5. To account for the linear increase in temperature present for fully developed pipe flow with constant wall heat flux, the temperature is split into the periodic temperature and the mean temperature increase:

$$\widetilde{T} = \widetilde{T}_p + \frac{\Delta \widetilde{T}}{L_z} z \tag{3.7}$$

The mean temperature increase can be expressed by [65]:

$$\frac{\Delta \widetilde{T}}{L_x} = \frac{2q"}{\delta \rho c_p U_b} \tag{3.8}$$

Substitution into Equation 3.6 yields:

$$\frac{\partial \widetilde{T}_p}{\partial t} + \frac{\partial}{\partial x_j}\left(\widetilde{u}_j \widetilde{T}_p\right) = \alpha \frac{\partial^2 \widetilde{T}_p}{\partial x_j \partial x_j} + u_z \frac{2q"}{\delta \rho c_p U_b} \tag{3.9}$$

This solves for the periodic temperature with the last term in Equation 3.9 accounting for heat flux, and requires the boundary condition for the periodic temperature to be a constant wall temperature.

3.3.2 Sub-grid Scale models

Based on the lack of previous numerical studies on buoyant liquid metal flows, multiple sub-grid models were considered and their applicability determined based on validation against DNS from Zhao et al. [27]. In this investigation, two different sub-grid scale models were considered:

1. Dynamic K-Equation (dynamicKEqn)

2. Wall Adapting Local Eddy-Viscosity (WALE)

The first is a local dynamic model with a sub-grid scale (SGS) kinetic energy equation (dynamicKEqn) proposed by Yoshizawa [66] and later modified by Kim and Menon [67] to include dynamic scaling of turbulence kinetic energy and dissipation. This details the sub-grid kinetic energy as:

$$\frac{\partial k_{sgs}}{\partial t} + \widetilde{u}_i \frac{\partial k_{sgs}}{\partial x_i} = -\tau_{ij}\frac{\partial \widetilde{u}_i}{\partial x_j} - \epsilon + \frac{\partial}{\partial x_i}\left(\nu_T \frac{\partial k_{sgs}}{\partial x_i}\right) \tag{3.10}$$

The sub-grid stresses τ_{ij} are modeled as:

$$\tau_{ij} = -2\nu_T \widetilde{S}_{ij} + \frac{2}{3}\delta_{ij}k_{sgs} \tag{3.11}$$

where

$$\nu_T = c_v k_{sgs}^+ \widetilde{\Delta} \tag{3.12}$$

Finally, the equation is closed by modeling the dissipation term:

$$\epsilon = c_\epsilon \frac{k_{sgs}^+}{\widetilde{\Delta}} \tag{3.13}$$

Kim and Menon [67] applied a dynamic model to obtain appropriate values for c_v and c_ϵ using a similar procedure as Germano et al. [68], which is described by:

$$L_{ij} - \frac{1}{3}\delta_{ij}L_{kk} = 2c_v M_{ij} \tag{3.14}$$

where:

$$M_{ij} = -\left(\widehat{\Delta} K^{\frac{1}{2}} \widehat{\widetilde{S}}_{ij} - \Delta k_{sgs}^{\frac{1}{2}} \widehat{\widetilde{S}}_{ij}\right) \quad (3.15)$$

where ($\widetilde{}$) represents a test filtered quantity. Equation 3.14 makes up a set of five independent equations that can be solved using a least square method proposed by Lilly [69] which gives:

$$c_v = \frac{1}{2} \frac{L_{ij} M_{ij}}{M_{ij} M_{ij}} \quad (3.16)$$

In order to evaluate c_ϵ, a mathematical identity between the dissipation rate resolved at the grid scale filter level

$$\epsilon = \nu \left(\widetilde{\frac{\partial u_i}{\partial x_j} \frac{\partial u_i}{\partial x_j}} - \frac{\partial \widetilde{u}_i}{\partial x_j} \frac{\partial \widetilde{u}_i}{\partial x_j} \right) \quad (3.17)$$

and the test filter level,

$$E = \nu \left(\widehat{\widetilde{\frac{\partial u_i}{\partial x_j} \frac{\partial u_i}{\partial x_j}}} - \frac{\partial \widehat{\widetilde{u}}_i}{\partial x_j} \frac{\partial \widehat{\widetilde{u}}_i}{\partial x_j} \right) \quad (3.18)$$

can be evaluated as:

$$F = E - \widehat{\epsilon} = \nu \left(\widehat{\frac{\partial \widetilde{u}_i}{\partial x_j} \frac{\partial \widetilde{u}_i}{\partial x_j}} - \frac{\partial \widehat{\widetilde{u}}_i}{\partial x_j} \frac{\partial \widehat{\widetilde{u}}_i}{\partial x_j} \right) \quad (3.19)$$

This is used to evaluate the model for the dissipation rate coefficient c_ϵ,

$$F = c_\epsilon G \quad (3.20)$$

where

$$G = \left(\frac{K^{\frac{3}{2}}}{\widehat{\Delta}} - \frac{\widetilde{k_{sgs}^{\frac{3}{2}}}}{\Delta} \right) \quad (3.21)$$

Lastly, this can be solved directly for a single unknown:

$$c_\epsilon = \frac{F}{G} \quad (3.22)$$

From this point, a local dynamic determination of the model coefficient is performed. Further details are available from Kim and Menon [67]. The second sub-grid treatment is the WALE

45

model developed by Nicoud and Ducros [70]. This model is based on the square of the velocity gradient tensor that accounts for effects from both the rotation and strain rate tensors while properly scaling the eddy viscosity in the near wall without requiring any dynamic scaling. Used in conjunction with Eq. 5, this forms the closure for the momentum equations. The mathematical formulation of the model is as follows:

$$\nu_T = \left(C_w \Delta\right)^2 \frac{\left|G_{i,j}^a\right|^{\frac{3}{2}}}{\left(S_{ij}S_{ij}\right)^{\frac{5}{2}} + \left|G_{i,j}^a\right|^{\frac{5}{4}}}$$

(3.23)

where Δ is taken as the cube root of the control volume and C_w is usually taken to be 0.5. G_{ij}^a is the trace-less part of G_{ij} defined as:

$$G_{ij} = \frac{1}{2}\left(g_{ik}g_{kj} + g_{ij}g_{ki}\right)$$

(3.24)

where

$$g_{ij} = \frac{\partial U_i}{\partial x_j}$$

(3.25)

The contribution to the Nusselt number from the turbulent heat fluxes, $u_j'T'$, is nearly negligible [27] with the overwhelming majority of the heat transfer occurring due to conduction; therefore only the resolved heat fluxes are necessary to properly capture the heat transfer for this flow For this reason there is no need for an additional sub-grid model to be added to Equation 3.9.

In OpenFOAM there are two options generally available to determine the filter cut-off (Δ), cube root volume and Van Driest. The cube root volume is given by:

$$\Delta = c(V_c)^{\frac{1}{3}}$$

(3.26)

where c is a model coefficient typically taken as 1. The Van Driest is given by:

$$D = 1 - exp(\frac{y^+}{A^+})$$

(3.27)

with the final length scale given by:

$$\Delta = min(\frac{\kappa y}{C_s}D, \Delta_g)$$

(3.28)

Van Driest applies a damping function that is derived based on the law of the wall applied to regions up to $y^+ = 500$. This is not applicable as buoyancy aided flow does not follow this behavior and application of this model could introduce unwanted error. As far as the authors are aware, no correlative relationship exists similar to the wall of the wall that includes buoyant effects. For this reason, the choice of the filter must only depend on the mesh. The other option in OpenFOAM, Cube Root Volume, is simply the root of the cell volume. This does not require or need any knowledge of the flow conditions; therefore, this is an ideal candidate for use in predictive cases.

3.4 Mesh Selection

3.4.1 LES Mesh Selection

An integral step to performing LES is the determination of an adequate mesh for capturing key physics in a given set of simulations. While many metrics exist to accomplish this task, there is no widely accepted standard for LES. Using a modified version of Geurts and Fröhlich [71], the sub-grid activity is determined to estimate the total turbulent energy resolved for each LES prediction. Based on the work of Celik et al. [72], with simplifications made by Pope [73] and Lilly [74], this is expressed as the ratio of the sub-grid turbulent viscosity (ν_{sgs}) and total viscosity ($\nu_{sgs} + \nu$) given by:

$$S \approx \frac{\nu_{sgs}}{\nu + \nu_{sgs}}$$

(3.29)

The parameter, S, is non-dimensional and bounded from 0 (DNS) to 1, where the entirety of the turbulent energy is within the sub-grid. This is expressed as a percentage of activity of the given sub-grid scale model at a given physical location in the domain. Figure 3.2 shows this expression as a radial line trace sampled at several points from the wall to the center of the pipe for three different mesh densities at the same physical locations for $Ri = 0.017$. In order to maintain the integrity of

each mesh, the same number of cells in the laminar sub-layer (8) was kept constant for each mesh, while the remaining domain was varied. This can be seen from their matching sub-grid activities in the near wall region. Table 3.1 shows the defining parameters and statistics for each mesh used in the mesh study. Each mesh refinement resulted in an increase of nearly double the amount of cells. The finest mesh was comprised of 1.23 million cells. Figure 3.3 shows a cross section of the finest mesh used for all simulations that demonstrates the expansion of the mesh in the radial direction to accurately capture the turbulent features of the flow. As expected, as the mesh density is increased the sub-grid activity is decreased. The finest mesh (mesh 3) shows the lowest sub-grid activity with a maximum around 4% at any given location. Although it is expected that the most demanding mesh requirements would be for the lowest Richardson number ($Ri = 0.017$), a similar analysis was done to determine sub-grid activities across the entire range of Richardson numbers, and results are shown in Figure 3.4. Between the bounds of 0.017 and 0.040, the flow is expected to undergo a suppression of turbulence resulting in a drastically reduced sub-grid activity. Therefore, one would assume that the maximum sub-grid activity will remain lower for the first validation case of $Ri = 0.017$. Including the predictive cases shows that there is in fact a drastic reduction in the sub-grid activity from $Ri = 0.017$ to 0.025. From this lowest point there begins an increase in sub-grid activity which continues until $Ri = 0.040$. This demonstrates the appropriateness of the current mesh to be used for all simulations including those used for prediction and not simply validation.

Mesh	N_r	N_θ	N_z	Δr^+	$\Delta\theta^+$	Δz^+	cells
Mesh 1	18	29	150	0.2 - 7.5	40	68	391,500
Mesh 2	22	35	183	0.2 - 6.1	30	55	704,550
Mesh 3	26	44	215	0.2 - 5.5	24	47	1,235,520

Table 3.1: Number of mesh cells in each direction with associated cell spacing in wall units
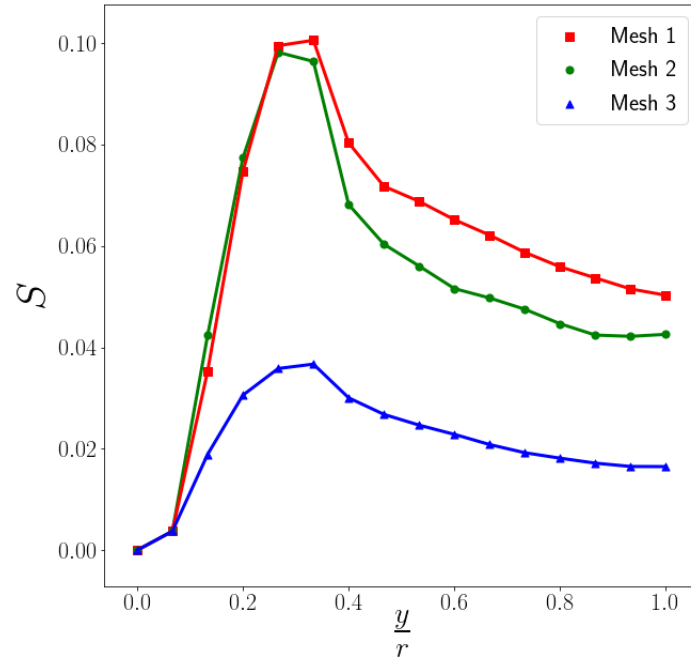
Figure 3.2: Sub-grid activity for each mesh at Ri = 0.017
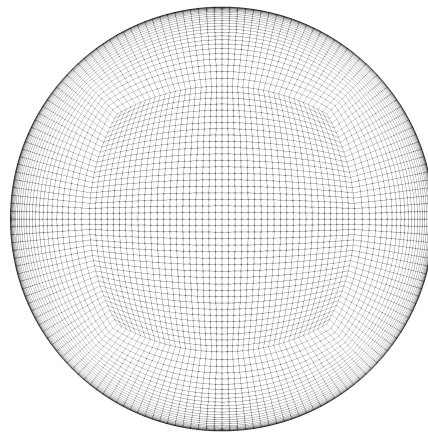
Figure 3.3: Cross section of o-grid mesh used in all simulations
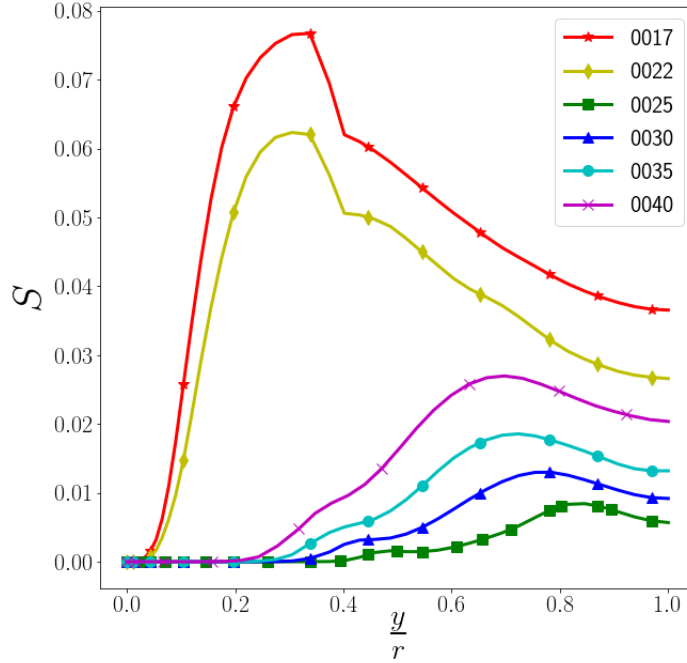
Figure 3.4: Sub-grid activity for $Ri = 0.017$ to 0.040

3.4.2 Sub-Grid Model Selection

Two different sub-grid models were tested in the validation portion of the investigation (WALE and dynamicKEqn). Figures 3.5 and 3.6 show results for the mean axial velocity and Reynolds shear stress at $Ri = 0.017$ and 0.040 in comparison to DNS from Zhao et al. [27]. Both WALE and dynamicKEqn are able to accurately predict the first order mean axial velocity with great similarity. Their differences begin to become more apparent in the prediction of the Reynolds shear stress. While both sub-grid models provide reasonable predictions, the dynamic k-equation model provides a more accurate prediction of the peak at $Ri = 0.017$. With this in mind, the subsequent analyses will utilize only the dynamic k-equation model for comparison.
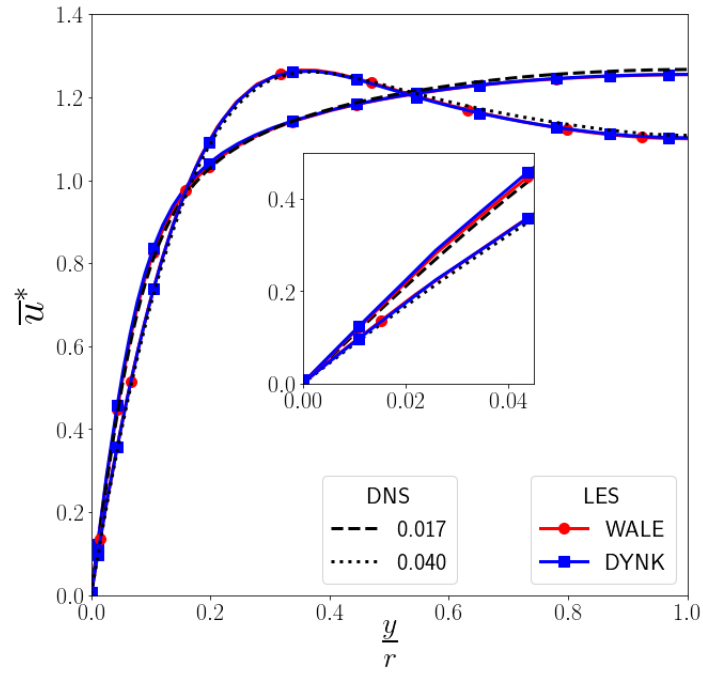
Figure 3.5: Comparison between WALE and dynamic k-equation models for mean axial velocity, $\overline{u}^*$

Figure 3.6: Comparison between WALE and dynamic k-equation models for Reynolds shear stress $\overline{u'v'}^*$

3.5 Results

3.5.1 Hydrodynamic

Figure 3.7 shows the time averaged axial velocity profiles sampled across the radius of the pipe. Note that the two validation cases ($Ri = 0.017$ and 0.040) are presented along with their corresponding DNS comparisons and predictive LES cases ($Ri = 0.022, 0.025, 0.030, 0.035$). Also included are results for forced convection to aid in overall comparis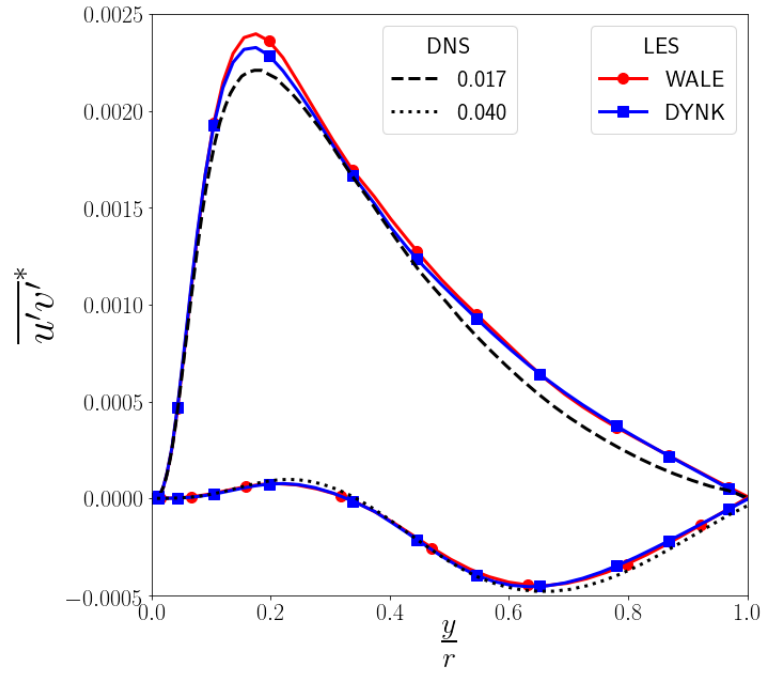on. For reference, all DNS profiles are presented as dotted lines for each Richardson number, with LES represented by solid colored lines.

In the presence of buoyancy with a fixed mass flow rate produced by a constant pressure gradient, the centerline velocity decreases as buoyancy increases from forced convection all the way up to natural convection. From $Ri = 0.0$ to 0.022, the centerline velocity is decreased considerably from forced convection. At these Richardson numbers, buoyancy begins to have a noticeable effect on the mean velocity profiles, but the flow remains turbulent. As buoyancy continues to increases the peak velocity shifts towards the heated wall. From the predictive cases shown here, this trend occurs rather rapidly between $Ri = 0.022$ and 0.025 with appearance of the 'M-shaped' velocity profile at $Ri = 0.025$. With such a small change in Ri producing a drastic change in the signature of the velocity profile, we begin to gain an appreciation of how abrupt the laminarization is for this particular flow.

Figure 3.8 shows the mean axial velocity profiles in wall units ($y^+, \overline{u}^+$). In forced convection or isothermal flows, the logarithmic law of the wall represents a self-similar solution for the mean axial velocity. Outside of the buffer layer, the velocity profile for forced or isothermal flows, adheres relatively close to a logarithmic relationship. Comparisons from DNS show this relationship is valid for $109 < Re_\tau < 2003$ [75]. As shown here, the DNS for $Ri = 0.0$ follows this relationship. Beginning with $Ri = 0.017$ and continuing through the range of simulations here, there is an large deviation from the law of the wall. It is important to note that this invalidates any model that utilizes damping functions based on the law of the wall, as noted earlier in regard to the Van

Driest filter approach. At $Ri = 0.025$, the largest magnitude is found, which is caused by the low friction velocity u_τ used in the non-dimensionalization. This begins to highlight the process of laminarization, where the skin friction is reduced to a minimum and eventually begins to return towards the forced convection value as observed between $Ri = 0.025$ to $Ri = 0.040$.
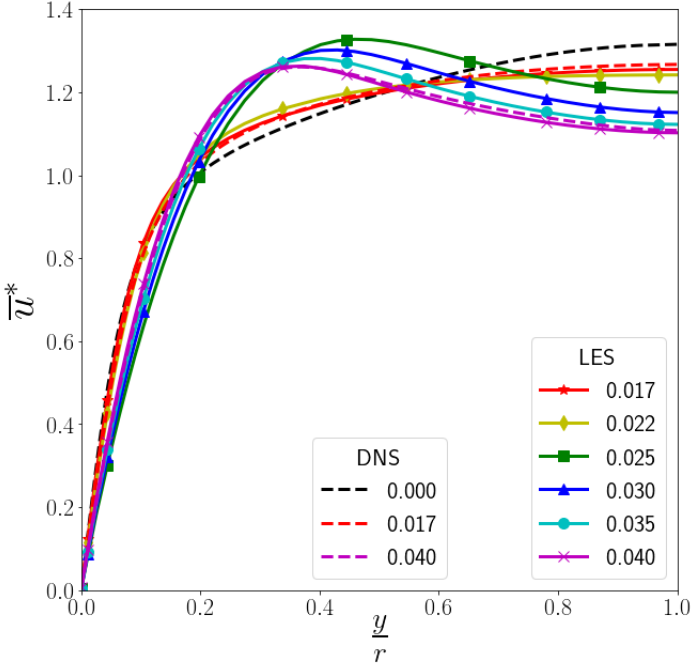
Figure 3.7: Mean axial velocity profiles plotted in global coordinates
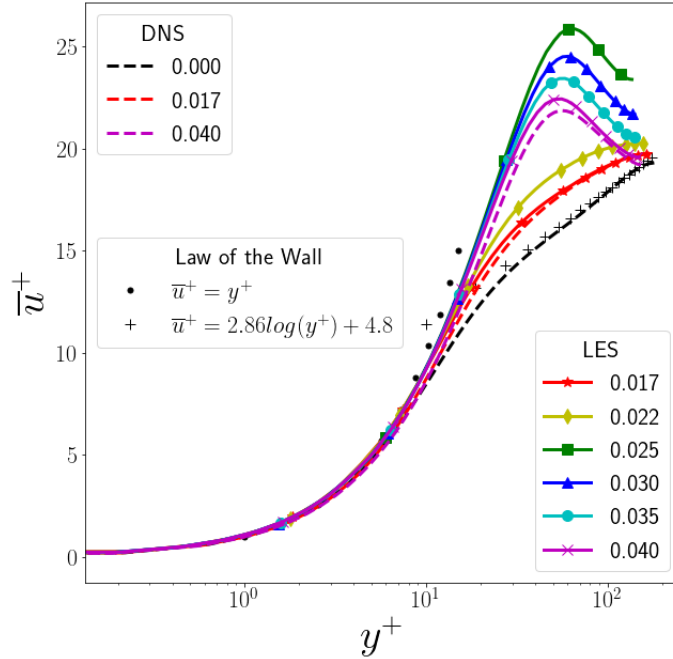
Figure 3.8: Mean axial velocity profiles plotted in wall units

Figure 3.9 shows the Reynolds shear stress ($\overline{u'v'}^*$). Consistent with previous DNS studies of turbulent mixed convection in a pipe by You et al. [26] and Zhao et al. [27] the Reynolds shear stress decreases non-monotonically with increasing buoyancy before undergoing a recovery with continued increase in Richardson number. The LES here shows in detail how rapidly this process occurs with the reduction of the shear stress between Ri = 0.022 and 0.025. At Ri = 0.025, the shear stress becomes negative in the turbulent core of the pipe. This negative contribution in the turbulent core suppresses the velocity which results in an increase of the velocity elsewhere to satisfy the conservation of mass. At the point of laminarization, there exist two distinct regions where in the near wall the flow behaves in a laminar fashion with turbulence still present in the core of the pipe. The result of this is the 'M-shape' typically seen in buoyancy-aided mixed convection flows above a critical Richardson number. Figure 3.10 shows the comparison of the skin friction coefficients at each Richardson number. The agreement between DNS and LES is more than satisfactory for both validation cases. In line with the Reynolds shear stress the skin friction is

reduced to a minimum at $Ri = 0.025$. From this point the skin friction begins to recover towards the fully turbulent value. To better quantify these predictions and determine the critical Richardson number for this flow, the FIK identity proposed by Fukagata et al. [76] is used. This identity breaks down the contributions to the skin friction coefficient into laminar, turbulent and buoyant terms:

$$C_f = \underbrace{C_{fl}}_{laminar} + \underbrace{C_{ft}}_{turbulent} + \underbrace{C_{fb}}_{buoyant} \tag{3.30}$$

$$C_f = \underbrace{\frac{16}{Re_d}}_{laminar} + \underbrace{8 \int_0^1 r\overline{u'v'}r dr}_{turbulent} - \underbrace{8 \int_0^1 (r^2 - 1)\langle \overline{f}(r) \rangle r dr}_{buoyant} \tag{3.31}$$

where

$$\langle \overline{f}(r) \rangle = \overline{f}(r) - 2 \int_0^1 r\overline{f}(r) dr \tag{3.32}$$

$$\overline{f}(r) = \frac{Ri}{Re_d \cdot Pr}\overline{\varphi} \tag{3.33}$$
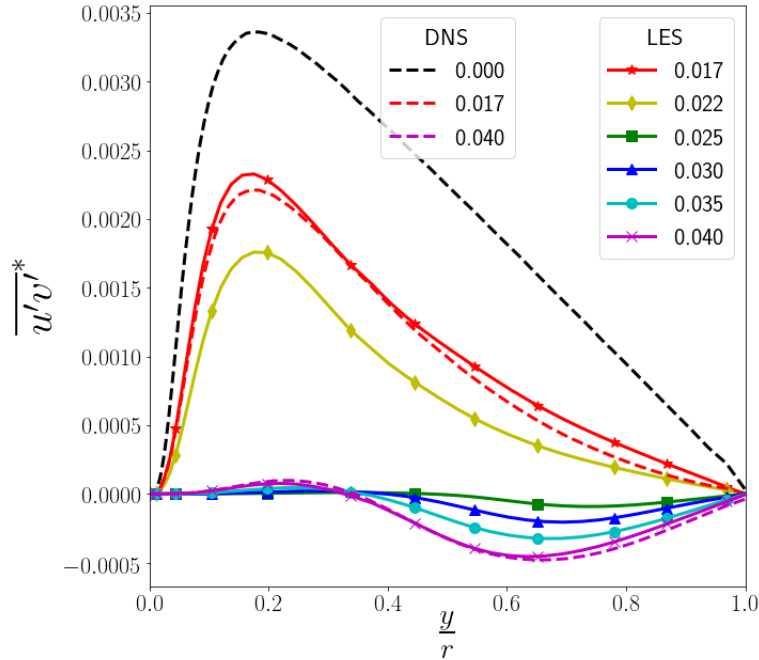
Figure 3.9: Reynolds shear stress plotted in global coordinates
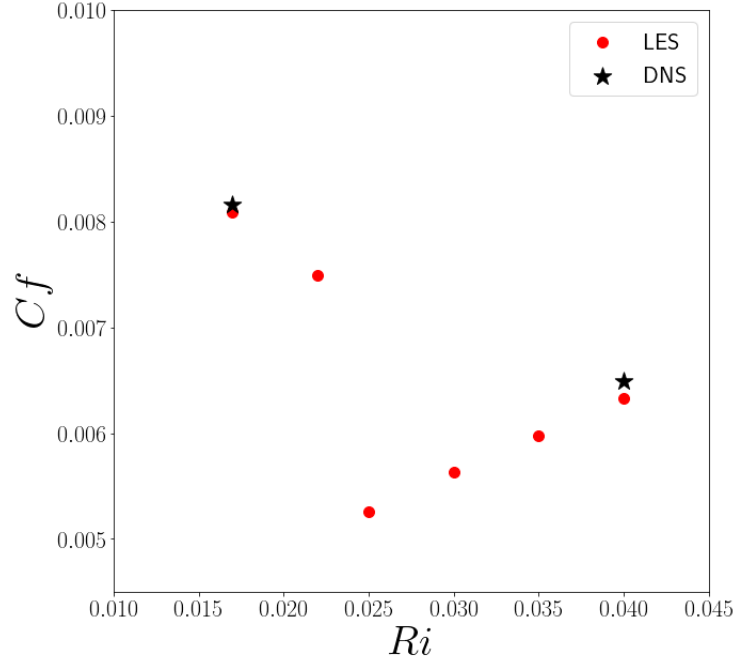
Figure 3.10: Skin friction coefficient (C_f) for LES and DNS from Zhao et al.

At this range of Richardson numbers the temperature profiles are not significantly different from each other; therefore, the buoyant contribution can be considered to grow at a nearly linear rate with only a dependence on the Richardson number. Note this only holds true for the range in this current study; a further increase in Ri would begin to deviate from this linear dependence [27]. Figure 3.11 shows the contributions to the skin friction coefficient for each Richardson number from each source. This figure highlights the rapid non-linear decay of the turbulence contribution from $Ri = 0.017$ to 0.025. Using the FIK identity as a metric, the onset of laminarization can be determined when the contribution to turbulence can be considered negligible. After laminarization has occurred the turbulent contribution grows at a very minimal rate. Interestingly, this contribution is negative and continues to grow increasingly more negative as the Richardson number is increased. Further, over the range simulated here the flow can be considered to remain laminar state for a range of a Richardson numbers with the onset of the laminarization regime occurring near $Ri = 0.025$ and continuing up to $Ri = 0.040$. As expected this behavior continues to increase

towards the recovery of turbulence as shown by Zhao et al. [27]. In order to better predict the onset of laminarization, using the turbulent contributions from $Ri = 0.025$ to 0.040, a polynomial was fitted with an order of two and an adjusted R-square was 0.9992 with root-mean-square-error (RMSE) of 1.519e-06. This strongly suggests that, in this range of Richardson numbers, the turbulent recovery grows quadratically. Applying a simple extrapolation, the onset of laminarization is predicted to be at $Ri \approx 0.023$.
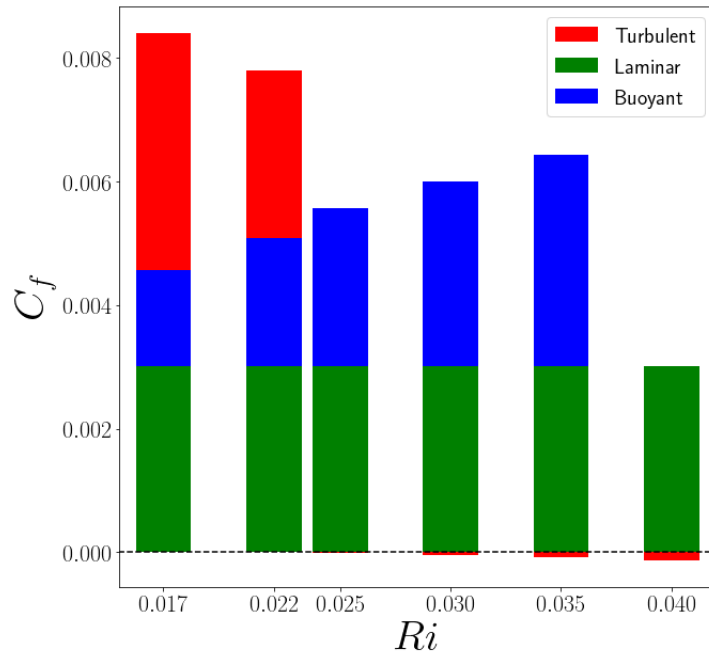
Figure 3.11: Contribution of each term to skin friction by FIK identity predicted by the dynamic k-equation model

Figure 3.12 shows the normal Reynolds stresses ($\overline{u'u'}^*$, $\overline{v'v'}^*$, $\overline{w'w'}^*$) from top to bottom. Initially, the stream-wise normal stress ($\overline{u'u'}^*$) is dominant by an order of magnitude in comparison to $\overline{v'v'}^*$ and $\overline{w'w'}^*$. After laminarization has occurred, this is no longer the case as all the normal stresses are comparable in magnitude. This behavior remains throughout this range.
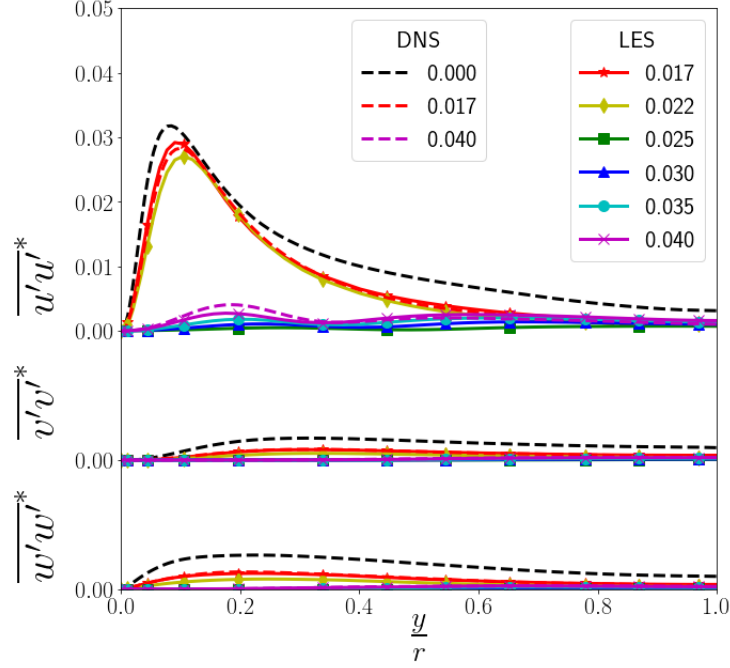
Figure 3.12: $\overline{u'u'}^*, \overline{v'v'}^*, \overline{w'w'}^*$ (top to bottom respectively) profiles plotted in global coordinates

Analysis of the budgets of the turbulence kinetic energy allow for deeper inspection into the dominant mechanisms for this particular flow. The equation for the budgets of turbulence kinetic energy are as follows:

$$\underbrace{\widetilde{u_j}\frac{\partial k}{\partial x_J}}_{Advection} = \underbrace{\frac{1}{\rho}\frac{\partial \widetilde{u_i'p'}}{\partial x_i}}_{Pressure\ Tran.} - \underbrace{\frac{1}{2}\frac{\partial \widetilde{u_j'u_j'u_i'}}{\partial x_i}}_{Turbulent\ Diff.} + \underbrace{\nu\frac{\partial^2\widetilde{k}}{\partial x_j^2}}_{Viscous\ Diff.} - \underbrace{\widetilde{u_i'u_j'}\frac{\widetilde{u_i}}{\partial x_j}}_{Production} - \underbrace{\nu\frac{\widetilde{\partial u_i'}}{\partial x_j}\frac{\partial u_i'}{\partial x_j}}_{Dissipation} - \underbrace{\frac{g}{\rho}\widetilde{u_i'T'}\delta_{ik}}_{Buoyancy}$$

(3.34)

Figure 3.13 shows a comparison between the production of TKE for each Richardson number. This highlights the scale of the reduction in production from $Ri = 0.017$ to 0.025. Figure 3.14 shows the budgets for the turbulence kinetic energy for each case with DNS comparison for $Ri = 0.017$ and $Ri = 0.040$. From $Ri = 0.017$ to 0.022, there is most noticeably a reduction in the shear production of TKE. From this point on there is a large reduction in all terms of the TKE budget. It should be noted that the scale of the y-axis from $Ri = 0.025$ to 0.040 have been adjusted to

properly display each budget term. For each Ri, viscous diffusion and dissipation are the dominant mechanisms in the near wall region while outside the laminar sub-layer, shear production becomes the main positive contribution. Near the laminarization point the shear production has a double peak begins to appear. This is a result from contribution from the turbulent shear stress becoming negative in the core of the pipe center causing the 'M-shape' behavior in the mean axial velocity profiles. As this remains negative with increase in Richardson number, the double peaks grow in magnitude. Consistent with DNS from Kasagi and Nishimura [24], You et al. [26] and Zhao et al. [27], the production due to buoyancy remains one of the smallest contributions to the turbulent kinetic energy.
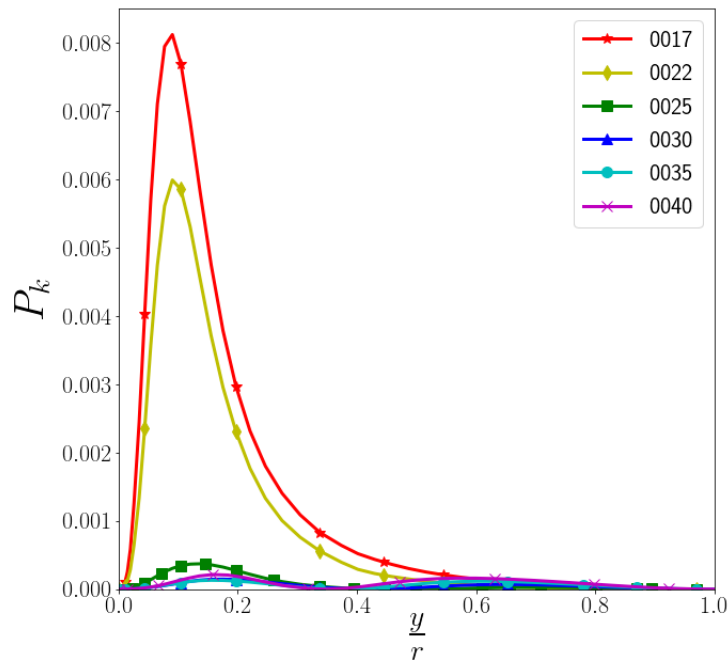
Figure 3.13: Comparison between production of turbulence kinetic energy for each Richardson number
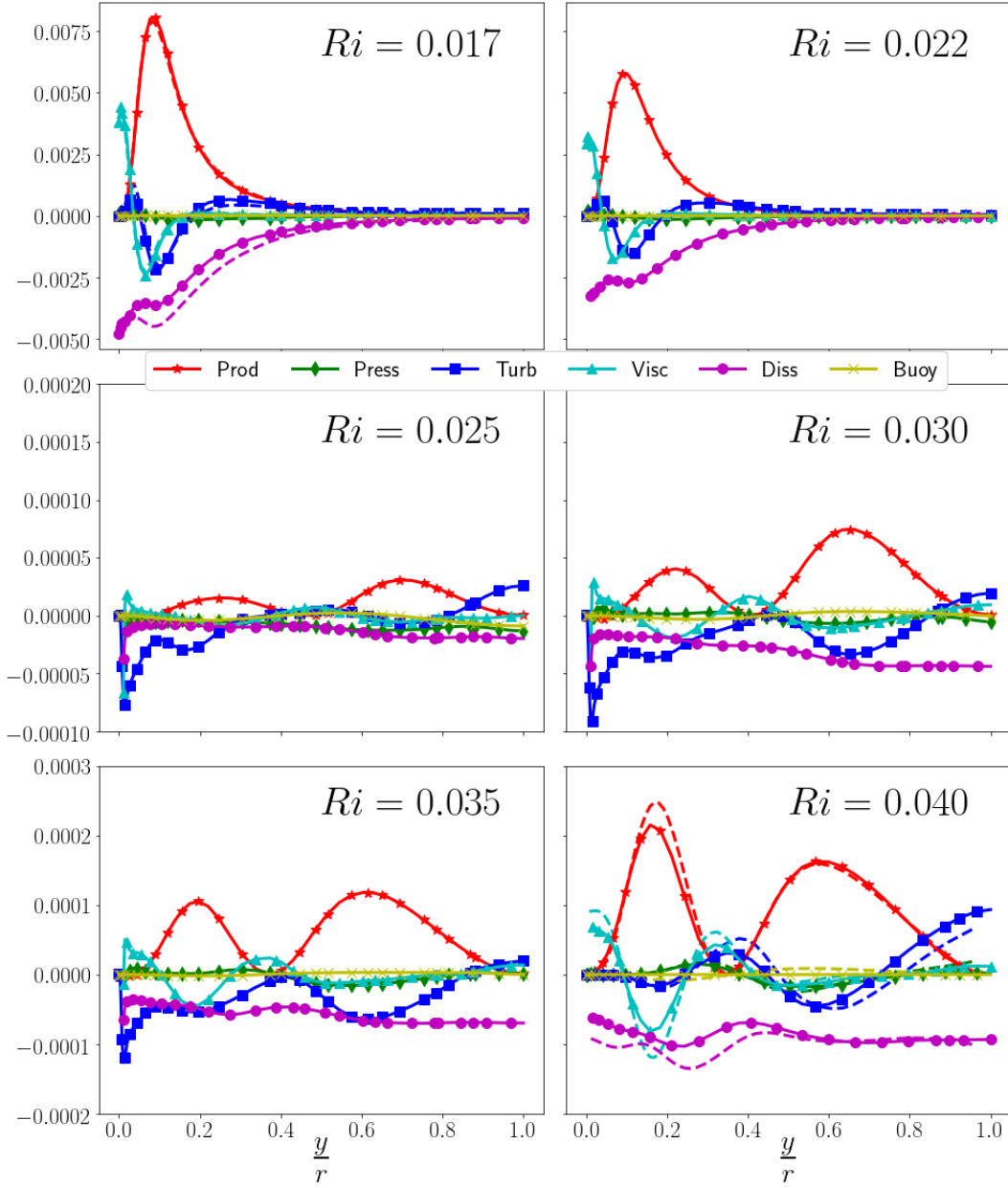
Figure 3.14: Budgets for turbulence kinetic energy plotted in global coordinates

3.5.2 Thermal

With a Prandtl number of 0.026 and $Re_d = 5300$, the dominant mode of heat transfer in this flow is conduction. In comparison, for a Prandtl number of 1.0, the thermal and momentum diffusivities are equal. For low Prandtl number fluids, thermal diffusion occurs at a much higher rate. As

seen in Figure 3.15, for this range of Richardson numbers, the change in the temperature profiles as the Richardson number increases is minimal. As shown by Zhao et al. [27] the contributions to the Nusselt number are almost completely dominated by the laminar contribution. Though less drastic to their counterparts in air, the turbulent heat fluxes here undergo a similar reduction as the Reynolds stresses. Figures 3.16 and 3.17 show the stream-wise ($\overline{u'\varphi'}^*$) and radial ($\overline{v'\varphi'}^*$) turbulent heat fluxes. The stream-wise turbulent heat flux shows a 'S-shape' profile akin to the Reynolds shear stress where contributions begin to become negative due to the increase in buoyancy. This begins to have a negative effect on the heat transfer which results in a drop in the Nusselt number.
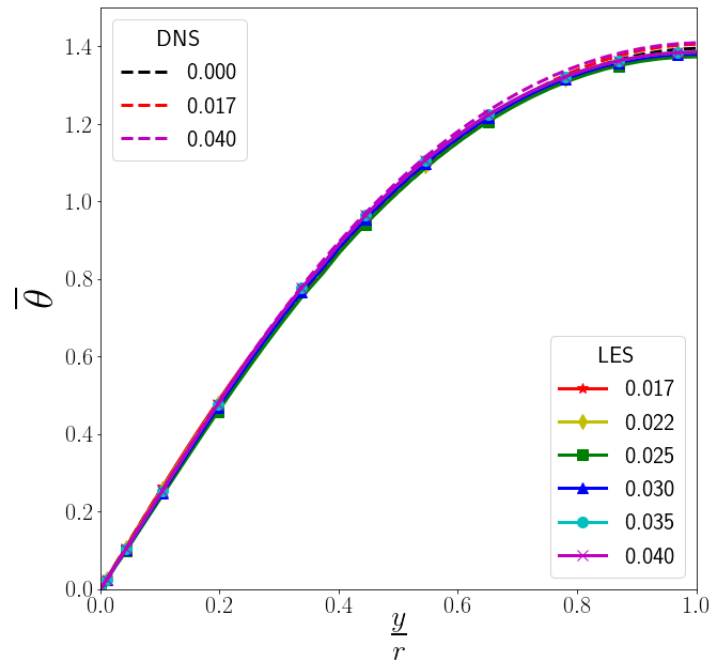
Figure 3.15: Non-dimensional Temperatures plotted in global coordinates
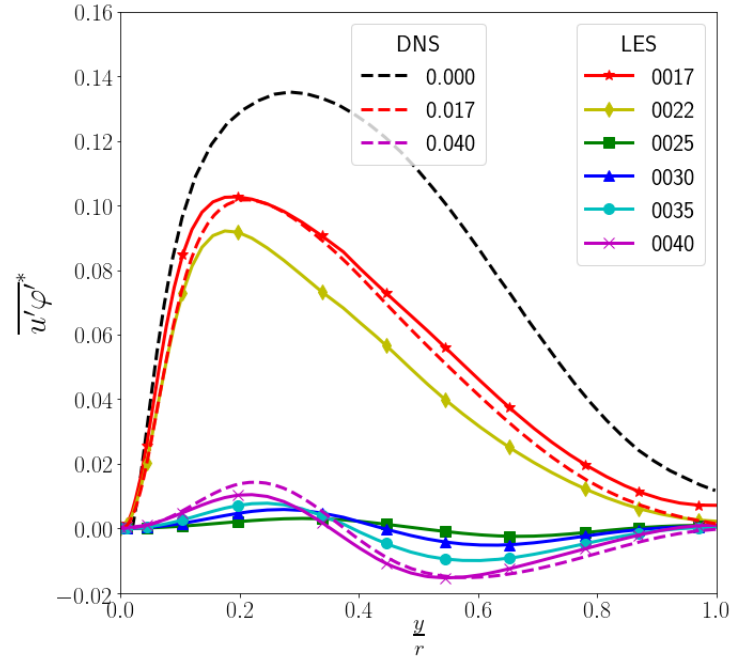
Figure 3.16: Stream-wise Turbulent Heat Flux $u'\varphi'^*$
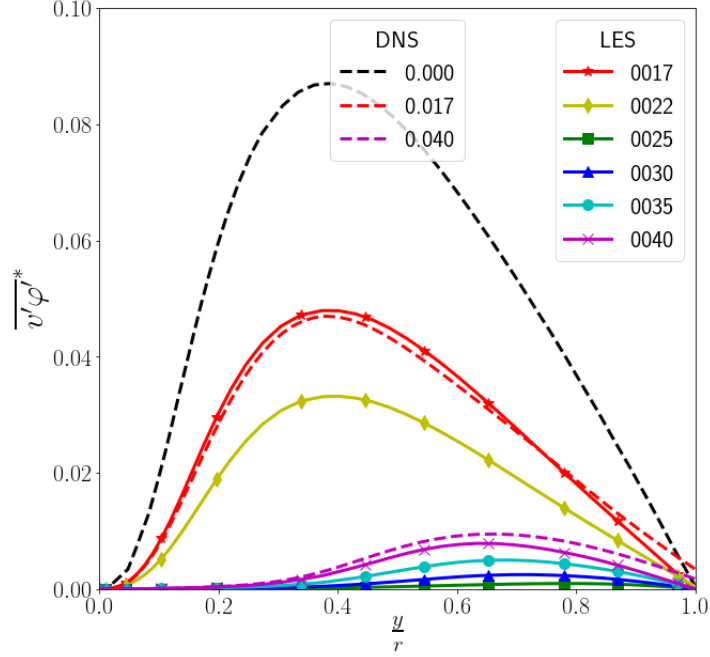
Figure 3.17: Radial Turbulent Heat Flux $\overline{v'\varphi'}^*$

The Nusselt number dependence on Richardson number is shown in 3.18. It is not surprising that the drop, and subsequent recovery of Nu is coincident with those same trends in skin friction (see Figure 3.11). It should be noted that Zhao et al. [27], since they only considered the largest and smallest Ri values, under predicted the heat transfer impairment. Only by considering additional value for Ri are we able to gain an appreciation of how significant that decrease actually is. It should also be noted that the reported values of Nu from Zhao et al. [27] are not consistent with those found from the current study. Another related LES study done by Centurelli [45] attempted to reproduce the results from Zhao et al. [27], also with limited success. However, they eventually found excellent agreement after applying an adjusted formulation for the bulk temperature (given as T_b^*) according to:

$$T_b^* = \frac{\int T^* r dr}{\int u^* r dr} \tag{3.35}$$

To provide the reader with further insight into the calculation of Nu using two different definitions for bulk temperature, we compute according to both and compare between those reported from

Zhao et al. [27] and Centurelli [45]. These results are provided in Table 3.2, and show excellent agreement for Ri = 0.017 and 0.040 to Zhao et al. [27] when we employ the bulk temperature as defined in Equation 3.35. Therefore, one would assume that Zhao et al. [27]] also used this modified form of the bulk temperature. At any rate, we feel confident moving forward that our LES modeling approach accurately captures both flow and temperature fields accurately at the two bounds of our analysis window. As a result, confidence can be placed on the intermediate values of Ri for which no other data currently exists. Future DNS efforts should be made to completely validate this claim, but for the results discussed here, the level of confidence in those results remains as high as possible, especially when accounting for what data the literature can provide for comparison.
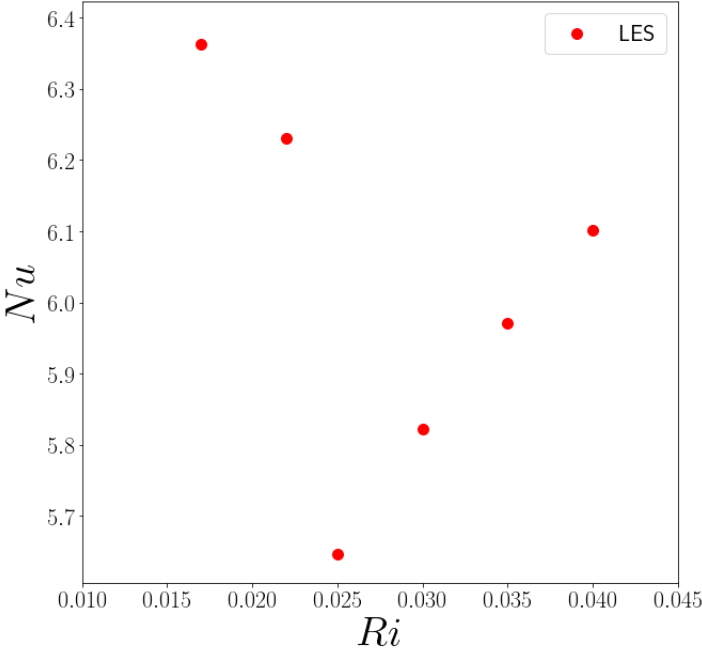
Figure 3.18: Nusselt number comparison from Ri = 0.017 to 0.040

Richardson	0.017	0.022	0.025	0.030	0.035	0.040
Nu (T_b)	6.41	6.17	5.66	5.86	6.00	6.14
Centurelli	6.55					6.07
Nu (T_b^*)	7.26	7.09	6.74	6.82	6.91	6.97
Zhao et al.	7.22					6.98

Table 3.2: Comparison of Nusselt numbers between current study, Zhao and Centurelli

3.5.3 Quadrant Analysis

While analysis of global metrics and SRQ profiles is vital in the study of turbulent flow, these really only show the effect on the flow from various sources, in this case buoyancy. In order to elucidate how the physics is altered, more detailed analysis of the flow is necessary.
Quadrant analysis is used to understand the physics involved in the generation of the Reynolds shear stress. Figure 3.19 shows the breakdown of the motions present in each quadrant reproduced based on a figure from Cai et al. [77]. Q2 and Q4 motions are considered gradient motions, which are responsible for the largest contributions to the Reynolds shear stress. Q1 and Q3 motions are characterized as counter-gradient motions which offset the effects of Q2 and Q4 motions, respectively. As shown by Wallace [78], the analysis can be expressed as the joint probability distribution function (JPDF) $P(u, v)$. Figure 3.20 shows the JPDFs for each case in this study.

Typical turbulent pipe flow shows increased activity in quadrants Q2 and Q4 which is indicative of the burst-sweep process that is responsible for the large turbulent contribution to the skin friction coefficient. As buoyancy is increased, as expected, the overall magnitude of the fluctuations is decreased in each quadrant. Remarkably though, after the onset of laminarization when the fluctuations begin to increase in magnitude, there is increased activity in Q1 with simultaneous reduction in Q2 and Q4. This indicates an increase in outward movement from the wall resulting in a negative impact on the skin friction coefficient. From this, we begin to gain an appreciation of

how the flow is directly altered by the presence of buoyancy.
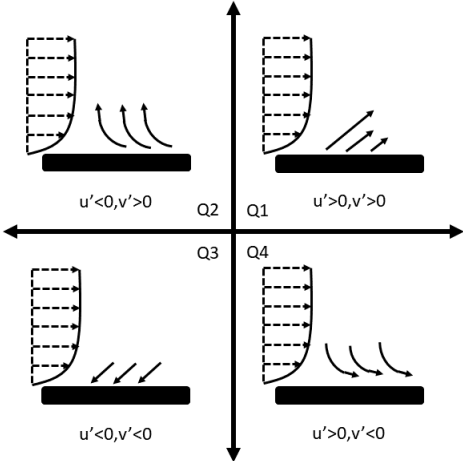
Figure 3.19: Quadrant analysis diagram reproduction based on work by Cai et al. [77]
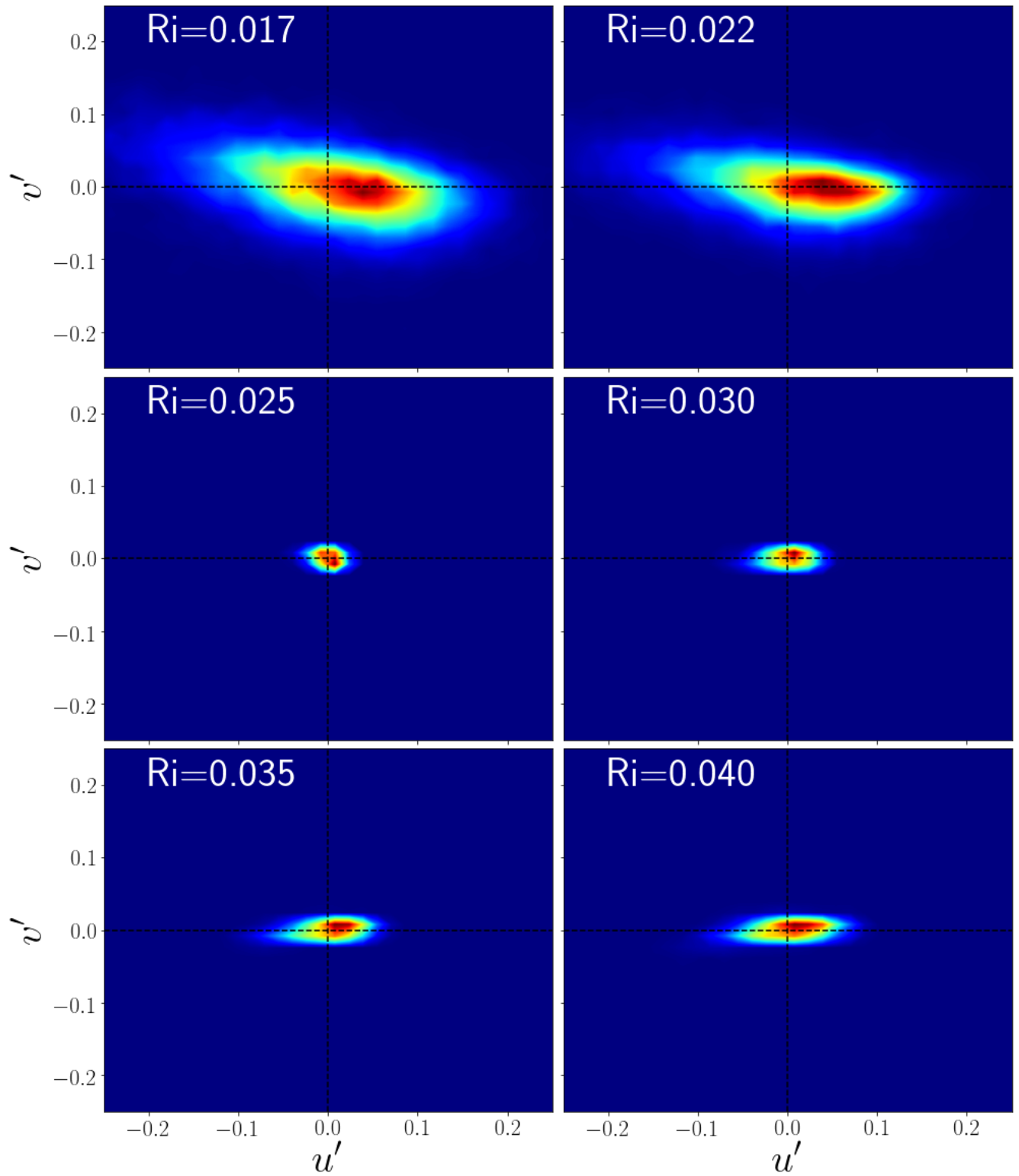
Figure 3.20: Quadrant analysis for Reynolds shear stress at $y^+ = 20$

3.5.4 Reynolds Stress Anisotropy

Anisotropy describes the physical variation of the fluctuations of the flow in magnitude and direction. Figures 3.21 and 3.22 show the invariants of the Reynolds shear stress anisotropy tensor. The second invariant, II, describes the magnitude of anisotropy and becomes zero when the turbulence is isotropic. With the attenuation of turbulence occurring in this flow, the anisotropy is increased with increasing Richardson number for buoyancy aided flows. This is consistent with results from Kasagi and Nishimura [24]. As the recovery begins, there is a return towards the initial case of $Ri = 0.017$. The third invariant, III, is a measure of the relative difference of one component of the flow direction to the other two. Consistent with Kasagi and Nishimura [24], both invariants have similar shape but different magnitude at the same condition.
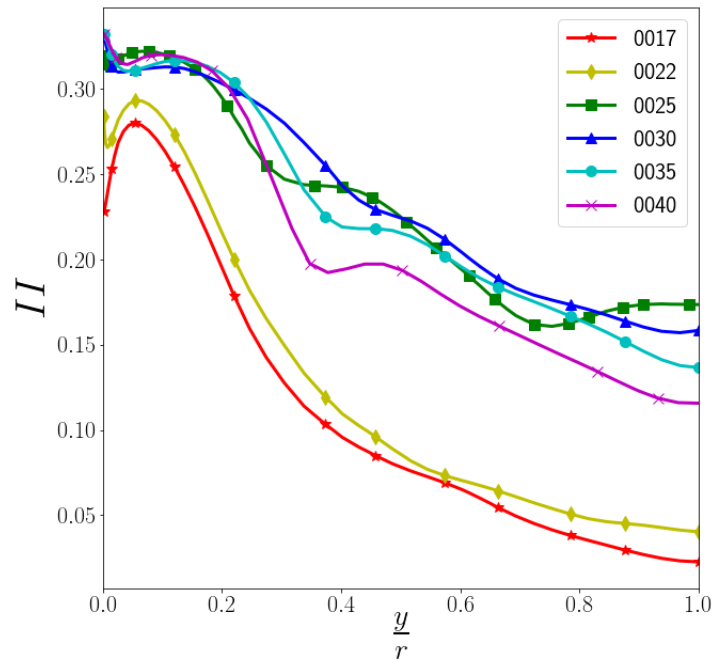
Figure 3.21: Second invariant of the Reynolds shear stress tensor
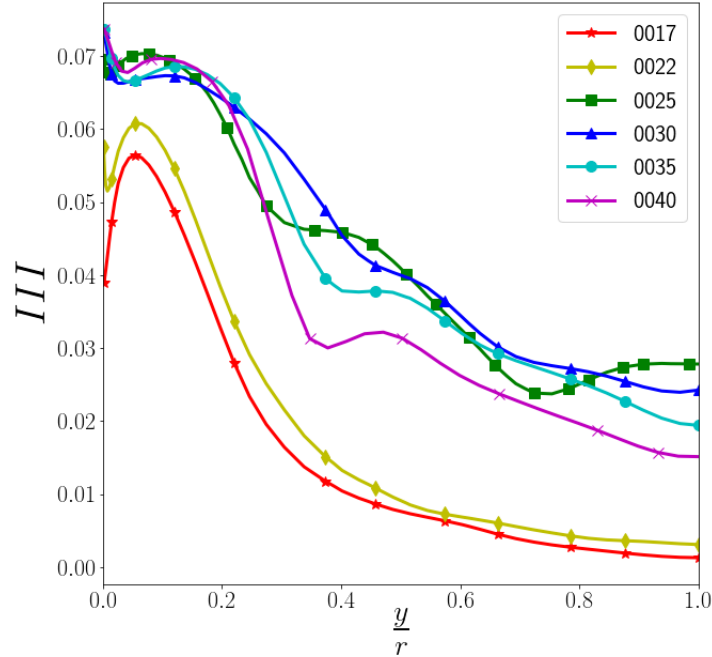
Figure 3.22: Third invariant of the Reynolds shear stress tensor

Combining these two metrics creates the Lumley triangle [79]. Figure 3.23 describes the different features of the Lumley triangle. Each of the extents (vertices and edges) is representative of a categorization of turbulence present for a flow. These represent all possible states of turbulence with the interior serving as a mixture of these states. Figure 3.24 shows each Lumley triangle from $Ri = 0.017$ to 0.040. Much like forced convection, early on in the turbulent mixed convection regime at $Ri = 0.017$, the near wall region is comprised of two-component turbulence. Away from the wall it moves towards one-component in the laminar sub-layer. From here to the log-law region it moves uni-directionally towards isotropy. With increase in buoyancy, this behavior is disrupted as the near wall region is shifted to the top-right extent, which is indicative of one-component turbulence. This disruption to the near wall turbulent processes is responsible for the reduction of skin friction. This trend continues for this range of Richardson numbers. In the center of the pipe, rod-like axisymmetric turbulence is dominant. With increase in Richardson this behavior trends towards the upper right extent of the triangle which suggests a change toward one compo-

nent turbulence occurs. With continued increase in Richardson number, the rod-like axisymmetric behavior is recovered.
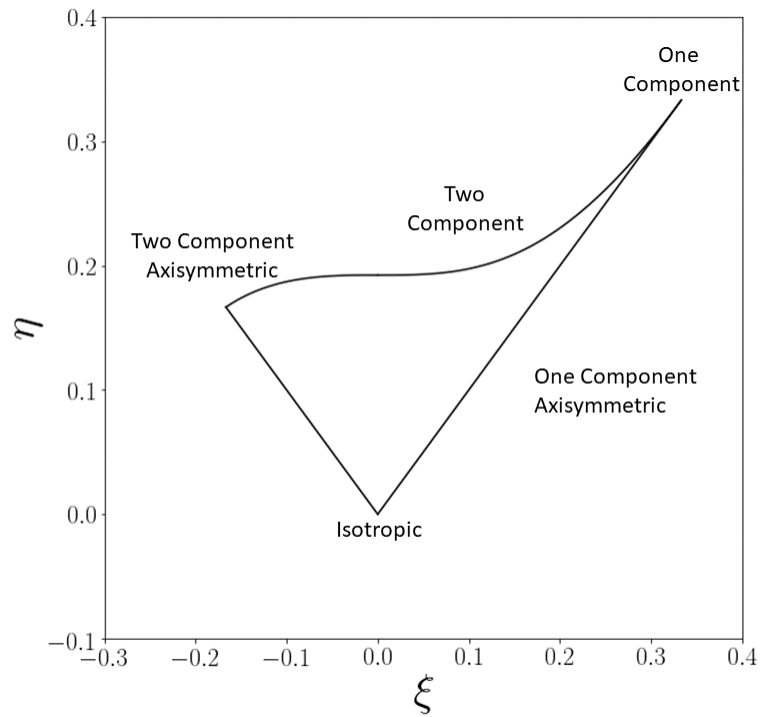
Figure 3.23: Description of the features of the Lumley triangle
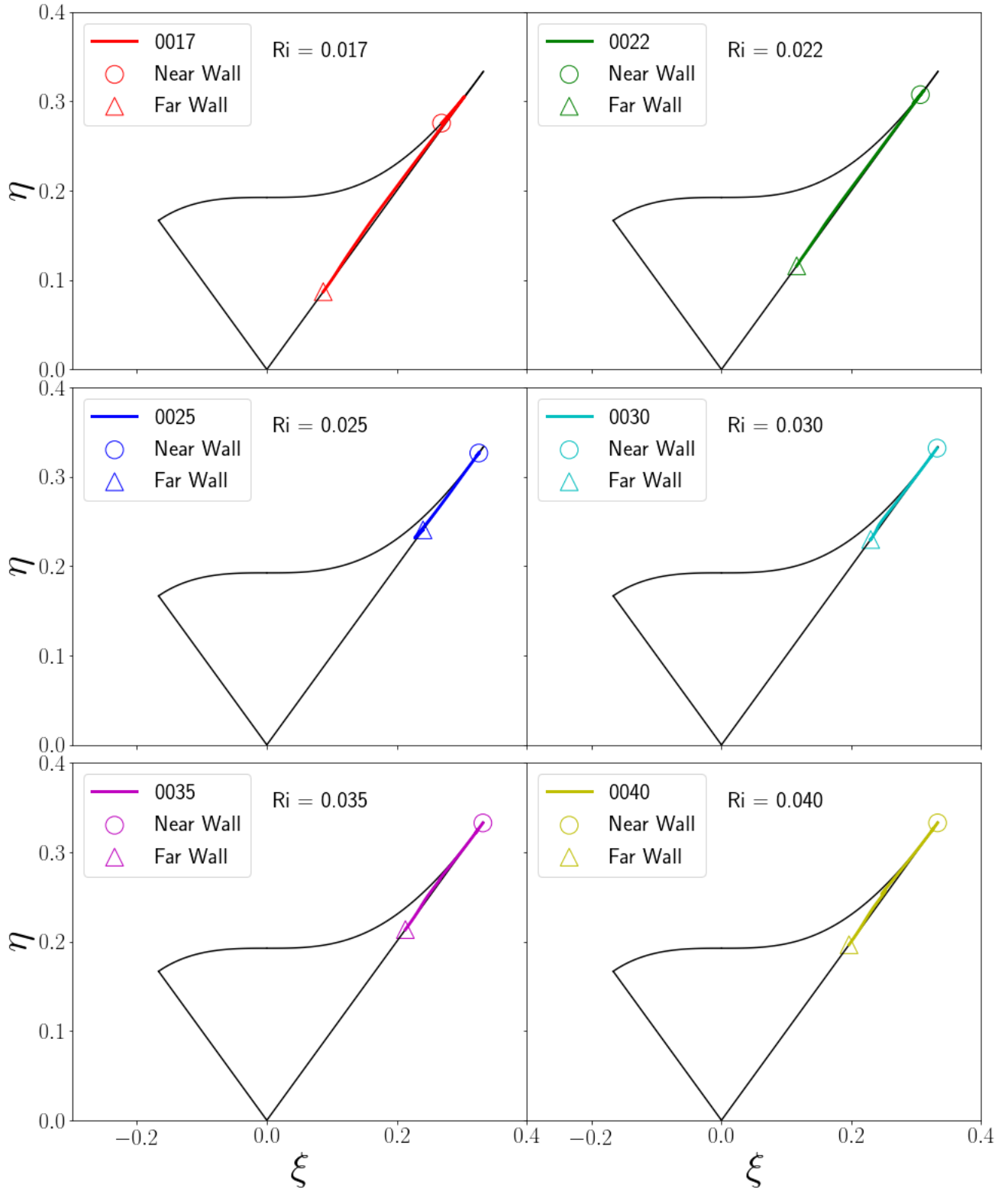
Figure 3.24: Lumley triangle comparison for each case.

3.5.5 Vorticity and Q-Criterion

Figures 3.25 and 3.26 show the stream-wise component and magnitude of the vorticity vector $(\nabla \times \vec{u}^*)$ for each Richardson number (0.017-0.040). This provides yet another glimpse at the rate of turbulence suppression and eventual recovery. This is also reflected in Figure 3.27 which shows the Q-criterion for Ri = 0.017 and 0.025 which is defined as the second invariant of the velocity gradient tensor given in it's mathematical form as:

$$Q = \frac{1}{2}\left[\left(tr(\nabla u^*)\right)^2 - tr\left(\nabla u^* \cdot \nabla u^*\right) \right] \tag{3.36}$$

This can also be written as:

$$Q = \frac{1}{2}\left[||\Omega^*||^2 - ||S^*||^2 \right] \tag{3.37}$$

Where tr represents the trace of the tensor, Ω is the vorticity tensor, and S is the strain rate tensor. The Q-criterion is representative of the physical locations where the vorticity magnitude is larger than the local rate of strain magnitude [80] [81]. Values of $Q > 0$ represent the presence of a vortex. From this the structures of turbulence are visible and comparison between multiple flows is possible using the same iso-surfaces. At Ri = 0.017 the structures are well defined throughout the pipe which is typical of turbulent pipe flow. Near the onset of laminarization at $Ri = 0.025$, the effect of the reduction in shear stress highlighted in Figures 4.6 and 3.20 is visible. Visible here, it is clear that turbulence is nearly completely removed in the near wall region, while maintaining a presence in the core of the pipe, albeit reduced. This is important to note as this could potentially have implications for modeling this behavior using methods such as Reynolds Averaged Navier-Stokes (RANS) turbulence models which are typically formulated to capture fully turbulent flows, with some models being capable of capturing transition from laminar to turbulence. These models are typically not capable of capturing both of these physics present simultaneously. Through this and the rest of this investigation, a more thorough understanding of the effect of buoyancy on turbulent buoyancy-aided pipe flow for lead-bismuth eutectic is acheived.
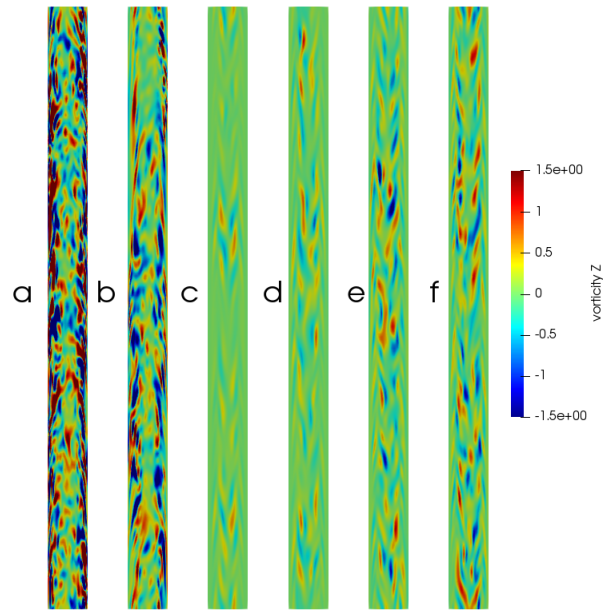
Figure 3.25: Z-component of the vorticity vector. a) 0.017 b) 0.022 c) 0.025 d) 0.030 e) 0.035 f) 0.040
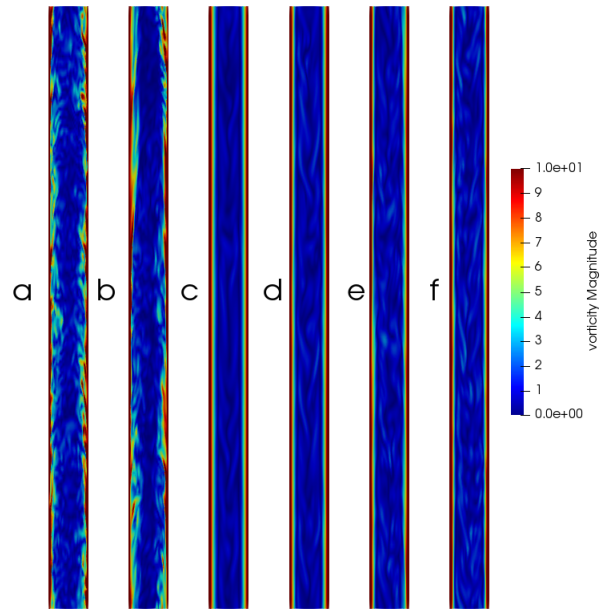
Figure 3.26: Magnitude of the vorticity vector. a) 0.017 b) 0.022 c) 0.025 d) 0.030 e) 0.035 f) 0.040
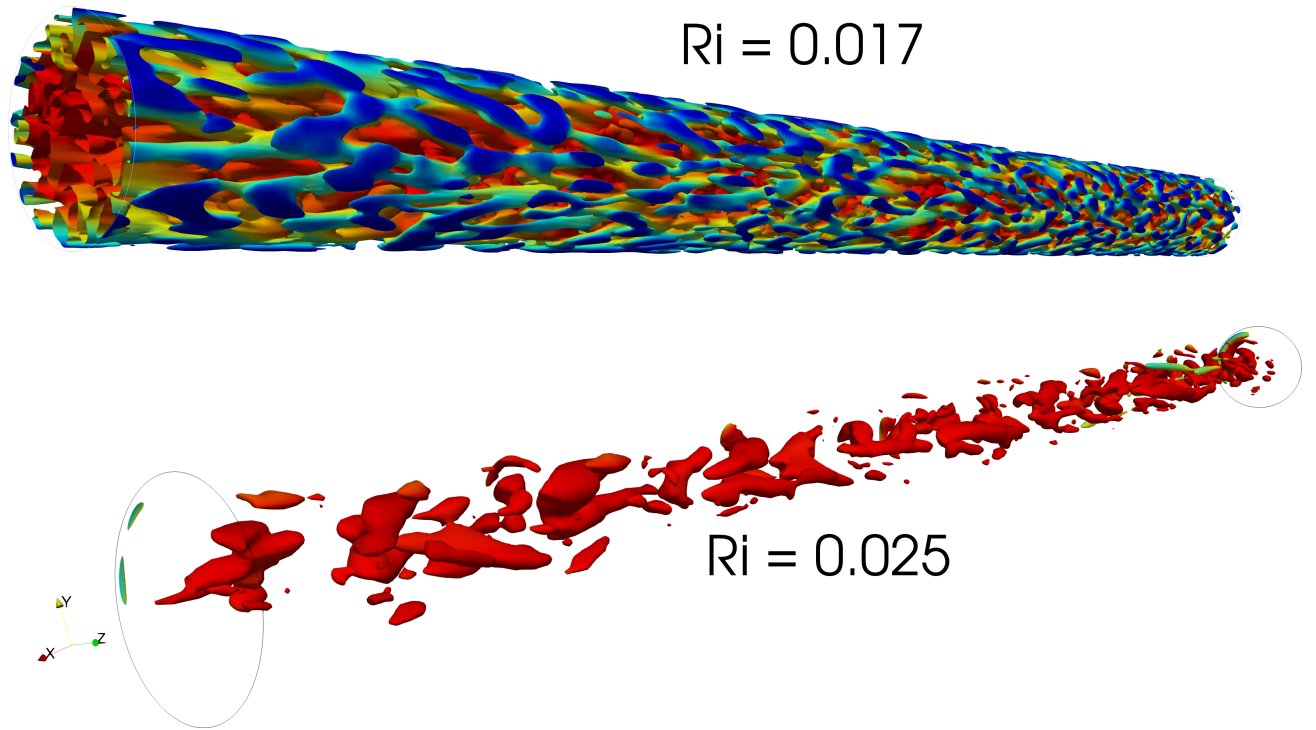
Figure 3.27: Q-criterion.

3.6 Section Conclusion

Through the use of LES, simulations of turbulent mixed convection pipe flow for LBE in an upward configuration in a range of increasing Richardson numbers was performed. Through the increase in the presence of buoyancy, the onset of laminarization was determined to occur near $Ri = 0.023$, with laminarization effectively continuing towards the end of the range of these simulations at $Ri = 0.040$. Further, the overall reduction of the skin friction at the onset of laminarization in comparison to forced convection is quantified with a reduction in over 30%. Additionally, heat transfer impairment of 15% was predicted at the onset of laminarization. Both of these values represent much larger impairments in comparison to previous predictions. This highlights the need for increased number of simulations in the Richardson number range near laminarization in order to properly quantify skin friction and Nusselt number impairment. This is made possible through the use of LES, which can signficantly reduce the computational cost of simulations in comparison

to DNS. This work represents an approach that can be used to validate and use LES for predictions of buoyancy-aided mixed convection pipe flows.

This investigation highlights the mechanisms that cause the overall reduction in skin friction which is indicative of laminarization. Using quadrant analysis, the overall change in shear stress is described with a marked change from dominance in Q4 to Q1 which is responsible for the negative turbulent contribution to the skin friction coefficient. This is visualized through vorticity contours and Q-criterion, where the separation between laminar and turbulent regions in the pipe is clearly visible near the onset of laminarization. Further, the anisotropy of the flow is quantified. This shows a complete picture of the causes and effects of the increase in buoyancy in upward flow for LBE in a pipe.

4. CALIBRATION OF LOW REYNOLDS EDDY VISCOSITY TURBULENCE MODEL FOR BUOYANCY AIDED MIXED CONVECTION

4.1 Section Summary

Turbulent mixed convection of lead-bismuth eutectic in a heated pipe at $Re_b = 5300$ is performed using a modified Reynolds Averaged Navier-Stokes approach. Using data available from direct numerical simulations and large eddy simulations, a linear eddy viscosity model is calibrated at various Richardson numbers. It is shown that through these changes that a linear model is capable of capturing the effects of buoyancy to the mean first and second order statistics including production and dissipation terms of the turbulence kinetic energy budget. Using this calibration, a potential correlative relationship between a parameter of the modified turbulence model and the Richardson number is proposed. This analysis also provides a quantitative comparative analysis between multiple RANS models including a model specifically adapted to include transition modeling from laminar to turbulent regimes.

4.1.1 Physical Domain and Numerical Method

Buoyancy aided turbulent mixed convection of LBE pipe flow is simulated using RANS. Using the DNS of Zhao et al. [27] and current LES (Section 3) for comparison, multiple RANS models were used to perform simulations from $Ri = 0.017$ to 0.04. Using this data set and model comparison, a calibration of a low Reynolds $k - \epsilon$ model was performed for each Richardson number.

To properly recreate this flow, a two-dimensional representation of a heated pipe (see Figure 4.1) was generated using ANSYS ICEM CFD, Release 19.0 [46]. The computational domain was set to be $\delta \times 5\delta$ in the x- and y-directions, respectively. Periodicity was set in the streamwise direction (y) with axisymmetric boundary conditions applied about the line $x = 0$. The mesh was designed to have $x^+ \leq 0.50$ in the radial direction to accurately capture both thermal and hydro-dynamic boundary layers for each model. Using the previously described GCI method (Section 2), three grids were constructed using a constant refinement factor of four. From the outlined base mesh configuration of 12,000 elements (60 × 200), a coarser mesh featuring 3,000 elements (30 × 100) and finer mesh with 48,000 (120 × 400). Similarly, the uncertainty using the base mesh configuration was on the order of only a few percent for each SRQ.

ANSYS Fluent, Release 19.0 [47] was used for all simulations. The thermophysical properties are assumed to be constant with the effect of buoyancy modeled using the Bousinessq approximation. Spatially each transport equation was discretized using collocated second order upwind schemes for all advection terms. Diffusion terms were discretized using central differencing. The flow condition was maintained by applying a constant pressure gradient in the streamwise direction resulting in a bulk Reynolds number of 5300, which is consistent with Zhao et al. [27] and LES performed here. Constant heat flux is applied uniformly to the walls. Fluent allows the flow to become fully developed by adjusting the upstream bulk temperature. The heat flux is adjusted to maintain $\beta(T - T_{ref})/\rho_{ref} << 1$ in order to not violate the Bousinessq approximation. From this the gravity vector was determined to achieve the desired Richardson number for each simulation. Pressure-velocity coupling was achieved from the use of the SIMPLE algorithm by Patankar [53]. The discretized set of equations was solved using an algebraic multigrid (AMG) solver with the

criteria that the RMS residual for equation must reach below 10^-9. Temperature is solved for using a segregated solver, meaning separately from the momentum and pressure equations.
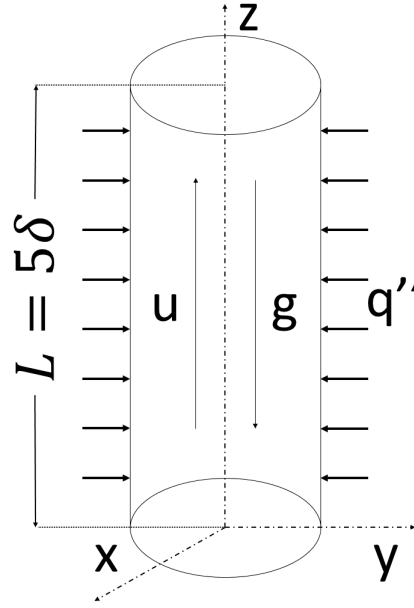
Figure 4.1: Physical domain for buoyancy-aided LBE pipe flow at $Re = 5300$

4.2 Mathematical Models

The steady state system of equations governing heat and fluid flow according the RANS approach is:

$$\frac{\partial \overline{u}}{\partial x_i} = 0 \tag{4.1}$$

$$\frac{\partial}{\partial x_j}\left(\rho \overline{u_i}\,\overline{u_j}\right) = -\frac{\partial \overline{p}}{\partial x_i} + \frac{\partial}{\partial x_j}\left[\mu\left(\frac{\partial \overline{u_i}}{\partial x_j} + \frac{\partial \overline{u_j}}{\partial x_i} - \frac{2}{3}\rho\delta_{ij}\frac{\partial u_l}{\partial u_l}\right)\right] + \frac{\partial}{\partial x_j}\left(-\rho\overline{u_i'u_j'}\right) - \beta g_i \rho\left(\Delta\overline{T}\right) \tag{4.2}$$

$$\frac{\partial}{\partial x_j}\left[\overline{u_i}\left(\rho\overline{E} + p\right)\right] = \frac{\partial}{\partial x_j}\left(\lambda_{eff}\frac{\partial T}{\partial x_j} + \overline{u_i}\left(\tau_{ij}\right)_{eff}\right) + S_h \tag{4.3}$$

80

where the contribution to turbulence is accounted for by $\rho \overline{u'_i u'_j}$ and λ_{eff} given by:

$$-\rho \overline{u'_i u'_j} = \mu_t \left(\frac{\partial u_i}{\partial x_j} + \frac{\partial u_j}{\partial x_i} \right) + \frac{2}{3} \delta_{ij} k \tag{4.4}$$

$$\lambda_{eff} = \lambda + \frac{c_p \mu_t}{Pr_t} \tag{4.5}$$

4.2.1 Low Reynolds k-ϵ models

In order to close this system of equations additional calculation is necessary to determine the turbulent viscosity, μ_t given by:

$$\mu_t = \rho C_\mu f_\mu \frac{k^2}{\epsilon} \tag{4.6}$$

The additional transport equations for turbulence kinetic energy, k and its rate of dissipation ϵ are given by:

$$\underbrace{\frac{\partial}{\partial x_i} (\rho k \overline{u_i})}_{\text{Advection}} = \underbrace{\frac{\partial}{\partial x_j} \left[\left(\mu + \frac{\mu_t}{\sigma_k} \right) \frac{\partial k}{\partial x_j} \right]}_{\text{Transport}} + \underbrace{P_k}_{\text{Production}} + \underbrace{G_b}_{\text{Buoyancy}} \underbrace{-\rho \epsilon}_{\text{Dissipation}} + \underbrace{D}_{\text{Damping}} \tag{4.7}$$

$$\underbrace{\frac{\partial}{\partial x_i} (\rho \epsilon \overline{u_i})}_{\text{Advection}} = \underbrace{\frac{\partial}{\partial x_j} \left[\left(\mu + \frac{\mu_t}{\sigma_\epsilon} \right) \frac{\partial \epsilon}{\partial x_j} \right]}_{\text{Transport}} + \underbrace{C_{1\epsilon} f_1 \frac{\epsilon}{k} P_k}_{\text{Production}} + \underbrace{C_{1\epsilon} C_{3\epsilon} \frac{\epsilon}{k} G_b}_{\text{Buoyancy}} \underbrace{-\rho C_{2\epsilon} f_2 \frac{\epsilon^2}{k}}_{\text{Dissipation}} + \underbrace{E}_{\text{Damping}} \tag{4.8}$$

The production of turbulence kinetic energy is modeled by:

$$P_k = \overline{u'_i u'_j} \frac{\partial \overline{u_i}}{\partial x_j} \tag{4.9}$$

In order to improve upon the standard k-ϵ approach, Low Reynolds $k-\epsilon$ models employ the use of damping functions to improve the near wall behavior of the turbulent viscosity (f_μ), production of turbulence dissipation rate (f_1) and destruction of turbulence dissipation rate (f_2), appearing in Equations 4.6 and 4.8, respectively. In the mean flow, the behavior of the standard $k - \epsilon$ model is recovered. Many of these models apply additional damping for both turbulence kinetic energy (D) and turbulence dissipation rates (E) (see Equations 4.7 and 4.8). For this study three different

variants of low Reynolds $k - \epsilon$ models are used for comparison:

1. Abid (AB)

2. Yang-Shih (YS)

3. Abe-Kondoh-Nagano (AKN)

Each model takes a different approach to the application of the damping functions. Their formulations can be seen as follows in Table 4.1. Additionally, the AKN model solves two other transport equations to determine the time scale for the thermal field. Ideally, this allows for the turbulent Prandtl number to be modeled rather than specified.

4.2.2 Transition SST Model

The $k - \omega$ models [82] use two transport equations to he turbulence kinetic energy (k) and the specific dissipation of turbulence kinetic energy (ω). From this a variation known as the shear stress transport model (SST) utilizes a blending function with blending between the $k - \omega$ formulation in the near wall regions and $k - \epsilon$ in the free-stream regions. Further details of this model's formulation are available from Menter [83]. Later developed by Menter et al. [84], the transition SST model uses two additional transport equations for intermittency (γ) and momentum thickness ($Re_{\theta t}$).

$$\frac{\partial(\rho\gamma)}{\partial t} + \frac{\partial(\rho u_j \gamma)}{\partial x_j} = P_{\gamma 1} - E_{\gamma 1} + P_{\gamma 2} - E_{\gamma 2} + \frac{\partial}{\partial x_j}\left[\left(\mu + \frac{\mu_t}{\sigma_\gamma}\right)\frac{\partial\gamma}{\partial x_j}\right] \tag{4.10}$$

With source terms $P_{\gamma 1}, e_{\gamma 1}, P_{\gamma 2}$, and $E_{\gamma 2}$. The second transport equation for momentum thickness is given by:

$$\frac{\partial(\rho\widetilde{Re_{\theta t}})}{\partial t} + \frac{\partial(\rho u_j \widetilde{Re_{\theta t}})}{\partial x_j} = P_{\theta t} + \frac{\partial}{\partial x_J}\left[\sigma_{\theta t}(\mu + \mu_t)\frac{\partial\widetilde{Re_{\theta t}}}{\partial x_j}\right] \tag{4.11}$$

With source term $P_{\theta t}$. Using the above along with additional proprietary correlations, the transition-SST model is suitable for flows in the transition regime. Further details of the model description are available from Menter et al. [84]. A goal of this study is to determine whether or not this model can predict laminarization from buoyancy using this same methodology.

4.3 Error Analysis

The ability to quantitatively assess the error of a model is important in the calibration process. In order to determine the effectiveness of any changes made to the model, the calculation of the change in error must be accurately performed. With many of these changes taking place over spatially varying SRQs, it becomes difficult to determine the overall effectiveness of a calibration. This need is addressed by the framework developed in Section 2. To recap, this method combines local error for a SRQ profile into two numbers that represent the cumulative relative error (ξ) between a model and the true/accepted value for the magnitude of a SRQ, $\xi\phi$ and the gradient of the SRQ, $\xi\nabla\phi$. From these two numbers a unique presentation of the comparative error can

Abbrev.	f_μ	f_1	f_2
AB	$tanh(0.0008Re_k)\left(1+\frac{4}{Re_t^{0.75}}\right)$	1	$\left[1-\frac{2}{9}exp\left(-\frac{Re_t^2}{36}\right)\right]\left[1-exp\left(-\frac{Re_k}{12}\right)\right]$
YS	$\left(1+\frac{1}{\sqrt{Re_t}}\right)\left[1-exp\left(\begin{array}{c}-1.5\times10^{-4}Re_y\\-5.0\times10^{-7}Re_y^3\\-1.0\times10^{-10}Re_y^5\end{array}\right)\right]^{0.5}$	$\frac{\sqrt{Re_t}}{1+\sqrt{Re_t}}$	$\frac{\sqrt{Re_t}}{1+\sqrt{Re_t}}$
AKN	$\left[1-\frac{5}{Re_t^{0.17}}exp\left(-\left(\frac{Re_t}{200}\right)^2\right)\right]\left(1-exp\left(-\frac{y^*}{14}\right)\right)^2$	1	$\left\{1-0.3exp\left(-\left(\frac{Re_t}{6.5}\right)^2\right)\right\}\left[1-exp\left(-\frac{y^*}{3.1}\right)\right]^2$

	D	E	Wall BC
AB	0	0	$k=0\,,\ \epsilon=\nu\frac{\partial^2 k}{\partial y^2}$
YS	0	$2\nu\nu_t\left[\left(\frac{\partial^2 V}{\partial x^2}\right)^2+\left(\frac{\partial^2 U}{\partial y^2}\right)^2\right]$	$k=0\,,\ \epsilon=2\nu\left(\frac{\sqrt{k}}{\partial y}\right)^2$
AKN	0	0	$k=0\,,\ \epsilon=2\nu\frac{k}{y^2}$

Table 4.1: Damping functions for low Reynolds $k-\epsilon$ models used in this study

be applied in the form of single scatter plot with $\xi\phi$ on the x-axis and $\xi\nabla\phi$ on the y-axis. Each model's error can be placed on this plot which allows for a clear visual representation of a model's capability.

An interest feature of this framework is the interchangeability of the metric used. As previously discussed, not all error metrics are created equal. It is up to the researcher to make a determination based on their data set which error metric is appropriate for their data set as a prior exercise to a full analysis. Previously in Section 2, the symmetric mean absolute percentage error was utilized. For this data set it was found that the error approached the maximum error bounds by most of the models for nearly every SRQ. With this in mind, an error metric discussed by Törnqvist et al. [62] was chosen due to the large disparity in model predictions in this analysis. The metric is formulated as:

$$\xi = ln\left(\frac{|P|}{|A|}\right) \tag{4.12}$$

In this instance where $P = A$, the error is 0 and grows as the disparity between predictions grows. This method is unbounded and therefore does not provide the same limitation for this data set. To cast this in the form presented in Section 2:

$$\xi\phi = \sum_{i=0}^{N} ln\left(\frac{|P|}{|A|}\right) \tag{4.13}$$

for the magnitude of a SRQ. Followed by the relative gradient error:

$$\xi\nabla\phi = \sum_{i=0}^{N} ln\left(\frac{|\nabla P|}{|\nabla A|}\right) \tag{4.14}$$

At each physical location the relative error is calculated. This error is then summed to produce a single measure of the overall relative error. This method can be applied to a calibration process to determine a relative change in error for any SRQ to determine whether or not improvement has been achieved.

4.4 Calibration of RANS model

User defined functions (UDFs) within ANSYS Fluent allow the user to dynamically modify features of the code. This enables a high level of customization, not often found in commercial CFD packages. While this alone is useful for the modification of a simulation, the task of loading and re-loading UDFs while varying a source file would be an arduous task. To accomplish this, ANSYS Fluent can be run as a server (AAS) coupled with Python 2.8 [85] using OmniOrb [86], which is a CORBA (Common Object Request Broker Architecture) ORB (Object Request Broker). This enables the C++ based Ansys Fluent code to couple with Python. From this coupling, Python can generate text user interface (TUI) commands within Fluent. TUI commands allow the user to utilize Fluent from a command line perspective. Figure 4.2 shows the work flow for a Fluent and Python coupling to implement parametric optimization. To initialize this process a precursor simulation is performed in order to obtain baseline values of all relevant system response quantities (SRQs). From this, an initial error value is calculated using experimental and/or direct numerical simulation data (DNS). For global metrics, L_1-error is typically sufficient, while for SRQ profiles a more robust quantitative framework is necessary as previously discussed.

The process used in this study is extensible to multiple parameters, though for ease of explanation and practicality, will be explained using a single parameter. Beginning with the aforementioned parameter, designated A1, the nominal value is perturbed in both positive and negative directions at equal displacements. The results from $+\Delta A1$ (positive) and $-\Delta A1$ (negative) simulations are compared to the nominal error calculation. The parameter is then adjusted to a new value based the perturbation that results in the steepest negative gradient. The process of perturbation and error calculation continues as long as the error continues to decrease, updating A1 at each iteration (2 total simulations) until perturbations at the current step size result in an increase in error for both perturbations, $+\Delta A1$ and $-\Delta A1$.

At this point, there is a reduction in the step size by a scaling factor. This procedure continues until the results once again represent an increase in error for both perturbations. Based on the precision of the calibration data, the amount and magnitude of step size reductions can be determined

86

to match the calibration data's precision. While this method is among the crudest of optimization methods, it is in fact, embarrassingly parallel. At each step, both perturbations $(+/-)$ for multiple parameters can be run concurrently. Assuming computational resources allow, multiple parameters can be perturbed for all combinations in the same amount of time as one parameter.
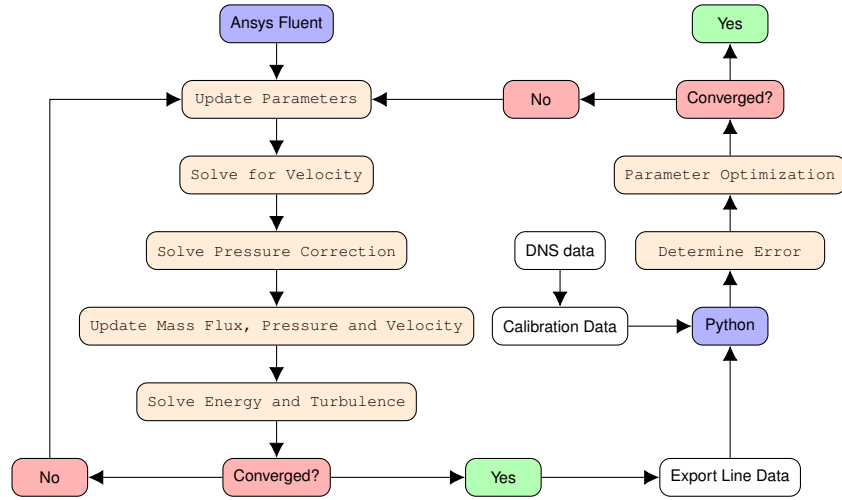
Figure 4.2: Flowchart for parametric calibration using Fluent and Python.

Using the previous described process, a parametric calibration of the damping function f_μ (Table 4.1) for the YS-model was performed. While other models were considered, YS was chosen based on the fact that only the f_μ damping function contains scaling parameters, while other models also include scaling factors in f_1 and f_2. The damping function is rewritten using A1, A2, A3 as the tunable parameters in the following form:

$$f_\mu = \left(1 + \frac{1}{\sqrt{Re_t}}\right)\left[1 - exp\left(- A1Re_y - A2Re_y^3 - A3Re_y^5\right)\right]^{0.5} \tag{4.15}$$

Via UDF, the turbulent viscosity μ_t (see Equation 4.6) can be updated. This allows the user to update parameters for f_μ. Using Python, the UDF sources files can be generated, imported, built and loaded into Fluent at the 'Update Parameters' step shown in Figure 4.2. Fluent follows this path

until the simulation is converged to the required residual error. From previous trials, not discussed here, it was determined that the only effective tuning parameter was the skin friction coefficient C_f. It was also determined that f_μ can be properly calibrated by only varying one parameter, $A1$, which has its largest effect in the near-wall region where C_f is calculated. Other system response quantities were considered including mean axial velocity $\bar{u}^*$, mean Reynolds shear stress $\overline{u'u'}^*$, dissipation $\bar{\epsilon}$ and shear production P_k which had varying results that were sub-par in comparison to calibration using the skin friction; therefore, this study presents only the results for calibration using the skin friction coefficient. Skin friction values were known to two decimal places and the algorithm was set to terminate once this precision had been reached. If this criteria is not met, the algorithm continues to run until it is determined the parametric variation no longer affects the L_1-error.

Figure 4.3 shows the value of A1 at each iteration of the optimization algorithm with the associated L_1-error ($|Cf_{dns} - Cf_{rans}| * 1000$) for $Ri = 0.017$ and 0.022. It is seen that these two cases follow similar trends during the calibration process. Initially, there is a linear decrease in error as A1 is minimized until the step-size is decreased. This results in some fine tuning with further step-size decrease. Eventually, at that step-size the L_1-error is no longer reduced resulting in termination.
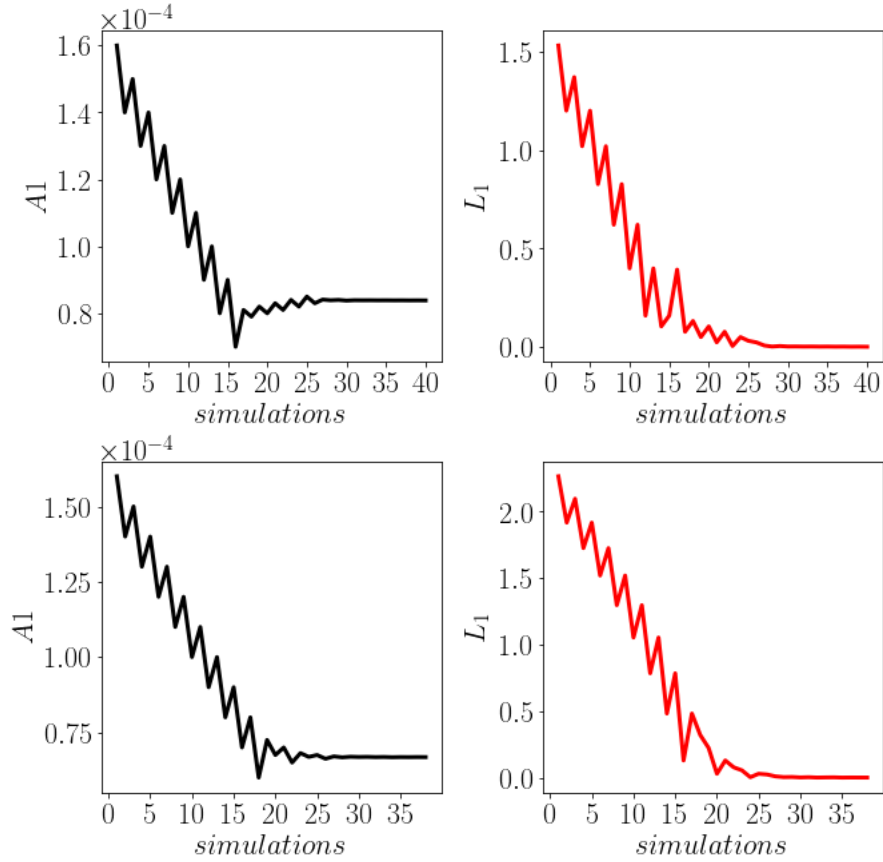
Figure 4.3: Error reduction due to calibration for $Ri = 0.017$ and 0.022

Figures 4.4 and 4.5 share remarkably similar features as well. A linear reduction in A1 results in the steady decrease in error up to a point where there is a sharp drop in error, and the algorithm terminates. Their differences lie in the amount of simulations needed to reach a minimum error value. At $Ri = 0.025$, more than 70 simulations are needed, while at $Ri = 0.04$ only 12 simulations are needed. We can see from these figures that the cases before laminarization follow a much more predictable trend and only those after the onset of laminarization have a sharp drop in error reduction. This is likely caused similarly to how the onset of laminarization occurs, where the momentum forces are suddenly overcome by the buoyant forces and the resulting change is a sudden reduction in shear stress. For these three cases, we see the trend where a continued decrease in A1 after a certain point doesn't change the error. This is evidence that there is a threshold at

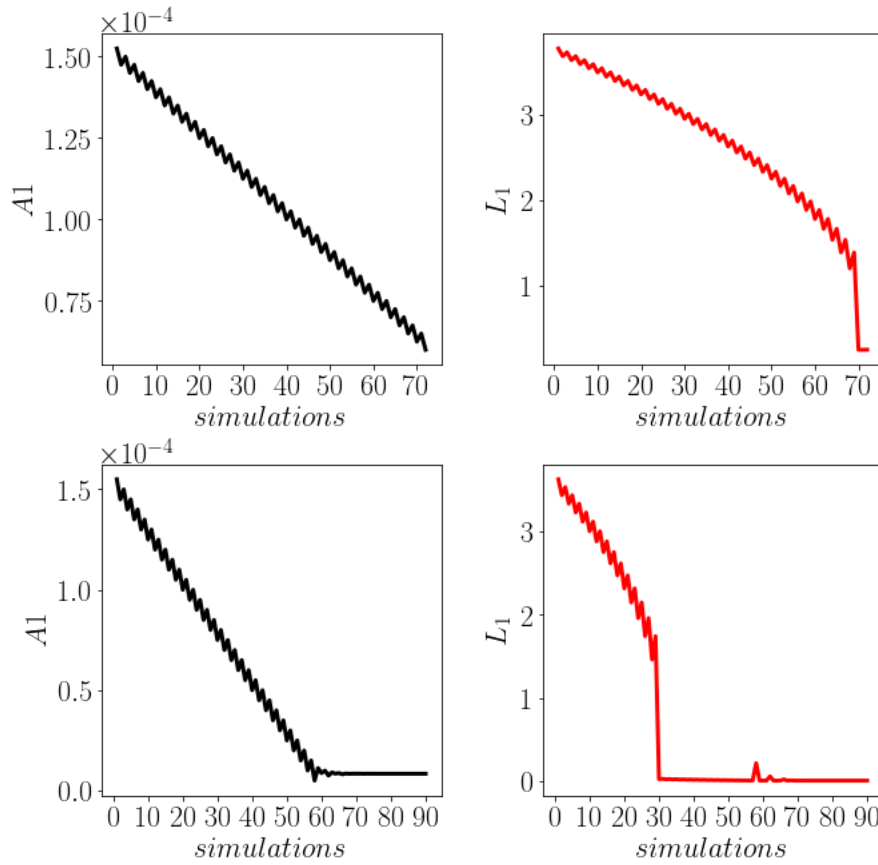where the parameter effectively no longer alters the near-wall behavior.

Figure 4.4: Error reduction due to calibration for $Ri = 0.025$ and 0.030
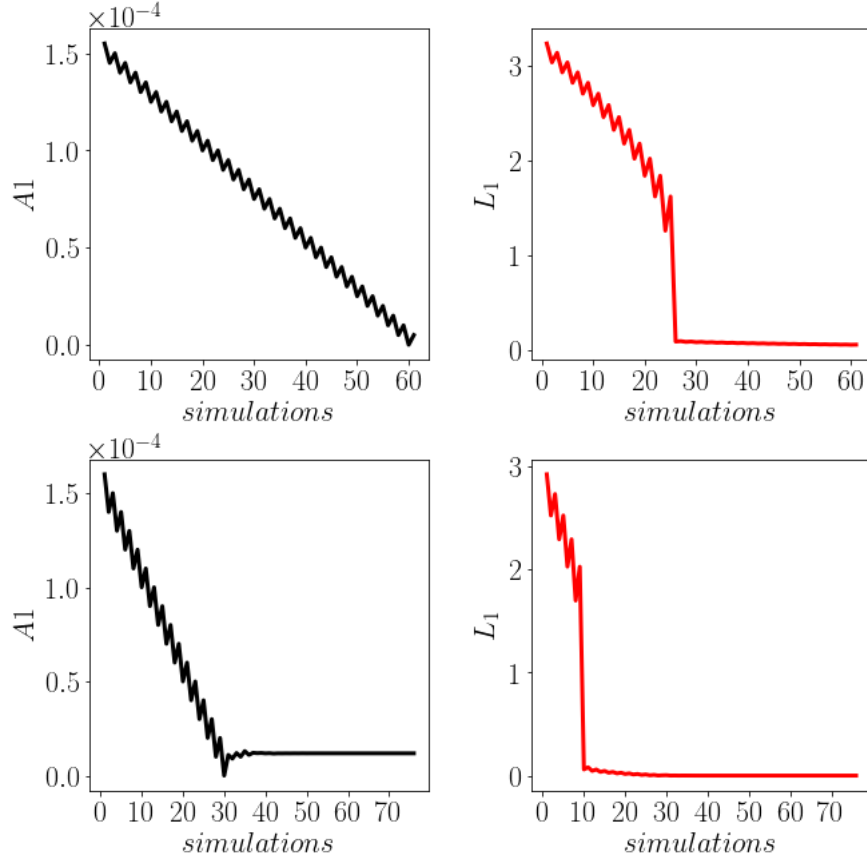
Figure 4.5: Error reduction due to calibration for Ri = 0.035 and 0.040

4.5 Results

Buoyancy-aided mixed convection offers an interesting challenge to most computational models. While the fluctuations are reduced drastically as laminarization takes places, with increasing buoyancy force the flow becomes exceedingly anisotropic before the turbulent recovery begins. Through many RANS studies, it has been shown that these models have difficulty adapting to highly anisotropic flows. Using three low Reynolds k-ϵ model variants and a more complex transition $k - \omega$ SST model with capability to predict the transition from laminar to turbulent flow regimes, simulations in a range of Richardson numbers for buoyancy-aided mixed convection pipe flow of LBE were performed. Further, a calibration is performed using the YS model and presented along with the unaltered models for each SRQ.

Figure 4.6 shows the predicted skin friction coefficient for each model in comparison to the validation LES and DNS data. AKN and YS demonstrate little to no sensitivity to buoyancy, while AB demonstrates limited adaptability. For Ri = 0.017 and 0.022, TRA greatly over predicts and then under predicts the skin friction, respectively. Although it predicts laminarization early, it eventually correctly follows the trend towards recovery in comparison to the validation data. Seeing as MOD was calibrated using each skin friction coefficient at each Richardson number, it agrees well at each Richardson number and correctly predicts the transition from turbulence to laminarized flow.

Figure 4.7 shows the skin friction coefficient in a relative comparison to the optimized parametric values. This shows there is a possible relation between skin friction and A1 for each Richardson number for this particular flow. Interestingly, at Ri = 0.025 the minimum skin friction does not result in the lowest predicted A1 value. Typically, turbulence models are designed for fully turbulent flows and as the parametric reduction continued at Ri = 0.025, the simulations became more and more unstable due to it's adjacency to the onset of laminarization. Below 5.1e-05 at Ri = 0.025, simulations began to diverge. Regardless, this does suggest there is a trend of minimization of A1 before a recovery of A1 begins towards its nominal value, similar to the skin friction trend. Overall, this suggests that different approaches to modeling the turbulent viscosity can have a large impact on the flows, and need not necessarily be as complicated as the well developed transition SST model. This is not intended to insinuate any flaws in the transition SST model exist, as it was designed to capture transition without the effects of buoyancy.
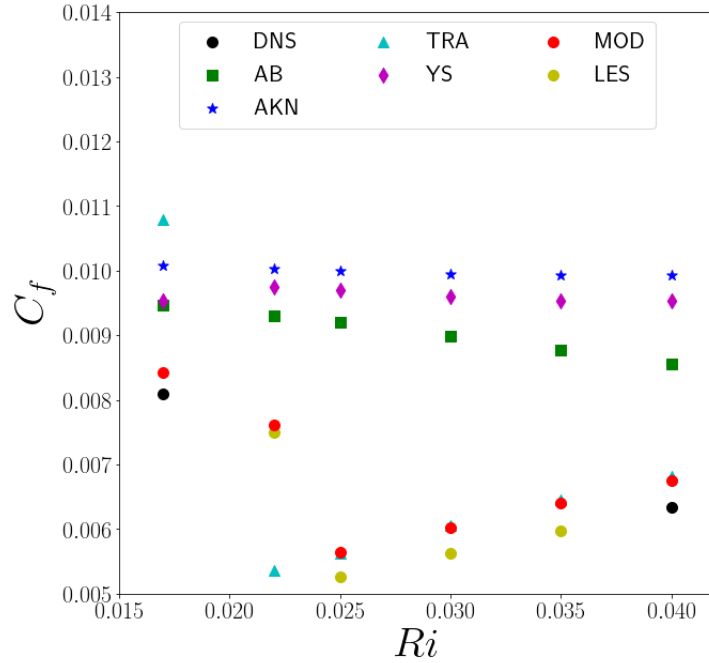
Figure 4.6: Comparison of skin friction coefficient for each model at Ri = 0.017 - 0.040
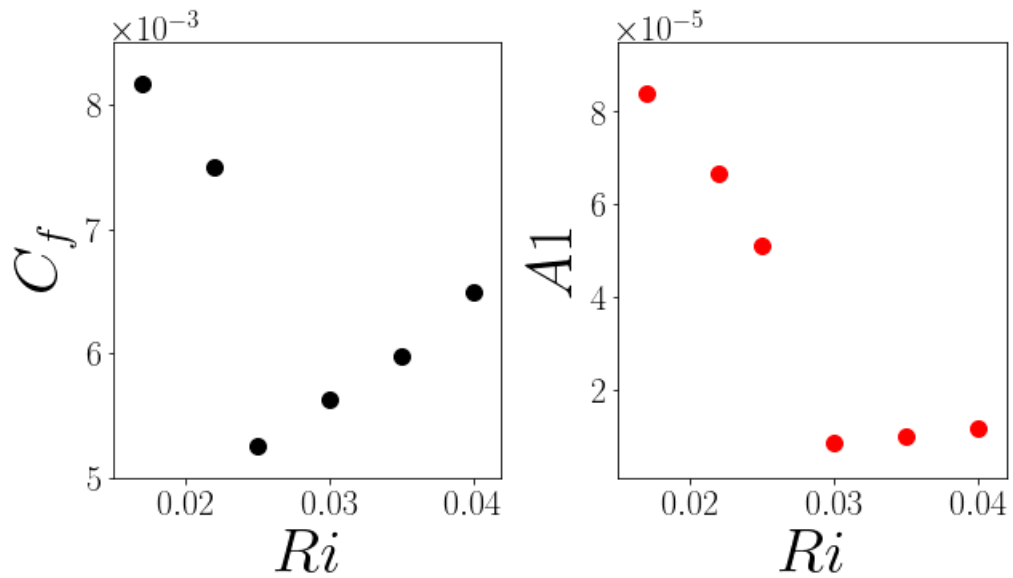

Figure 4.7: Skin friction coefficient dependence on Richardson number in comparison to optimal A1 at each Richardson number.

Figure 4.8 shows the mean axial velocity profiles ($\overline{u}^*$), for each model. All comparison are done with DNS from Zhao et al. [27] for Ri = 0.017 and 0.040 and LES performed here (Section 3) for Ri = 0.022, 0.025, 0.030, 0.035. At the onset of mixed convection the centerline mean axial velocity profiles begins to flatten from Ri = 0.017 to 0.022. In this range, TRA is overly sensitive to the presence of buoyancy and under predicts the centerline velocity at Ri = 0.017. TRA also largely misses the prediction at Ri = 0.022. Initially, YS under predicts the centerline velocity at Ri = 0.017 but recovers by Ri = 0.022. The remaining models including the re-calibrated model, MOD, all provide accurate predictions at these two Richardson numbers. After the onset of laminarization, according to the validation data the 'M-shape' velocity profile appears. MOD, which previously did not predict an 'M-shape' profile at $Ri = 0.022$ now shows this shape consistent with the LES validation data. The only other model to predict this with any consistency after laminarization is TRA. AB, AKN and YS all suffer from erratic behavior. Both AB and AKN eventually predict the m-shape profile but are unable to maintain this prediction up to Ri = 0.040. In comparison, the difference between YS and mod are vast. A simple re-calibration of a parameter in $f\mu$ has a large impact on the ability of the model to accurately capture the physics present. This further bolsters the hypothesis of Clifford and Kimber [34] which pointed to the turbulent viscosity scaling as a problem for predictions of mixed convection.

To assess the relative error and improvement of the re-calibrated MOD model, the previously discussed approach is adopted. Figure 4.9 shows the cumulative relative error between all of the models for their prediction of the mean axial velocity ($\overline{u}^*$). The MOD model best captures $\overline{u}^*$ in both magnitude and shape with TRA following second in both categories. From this, it is clear that AKN, AB and YS are unable to accurately capture $\overline{u}^*$.
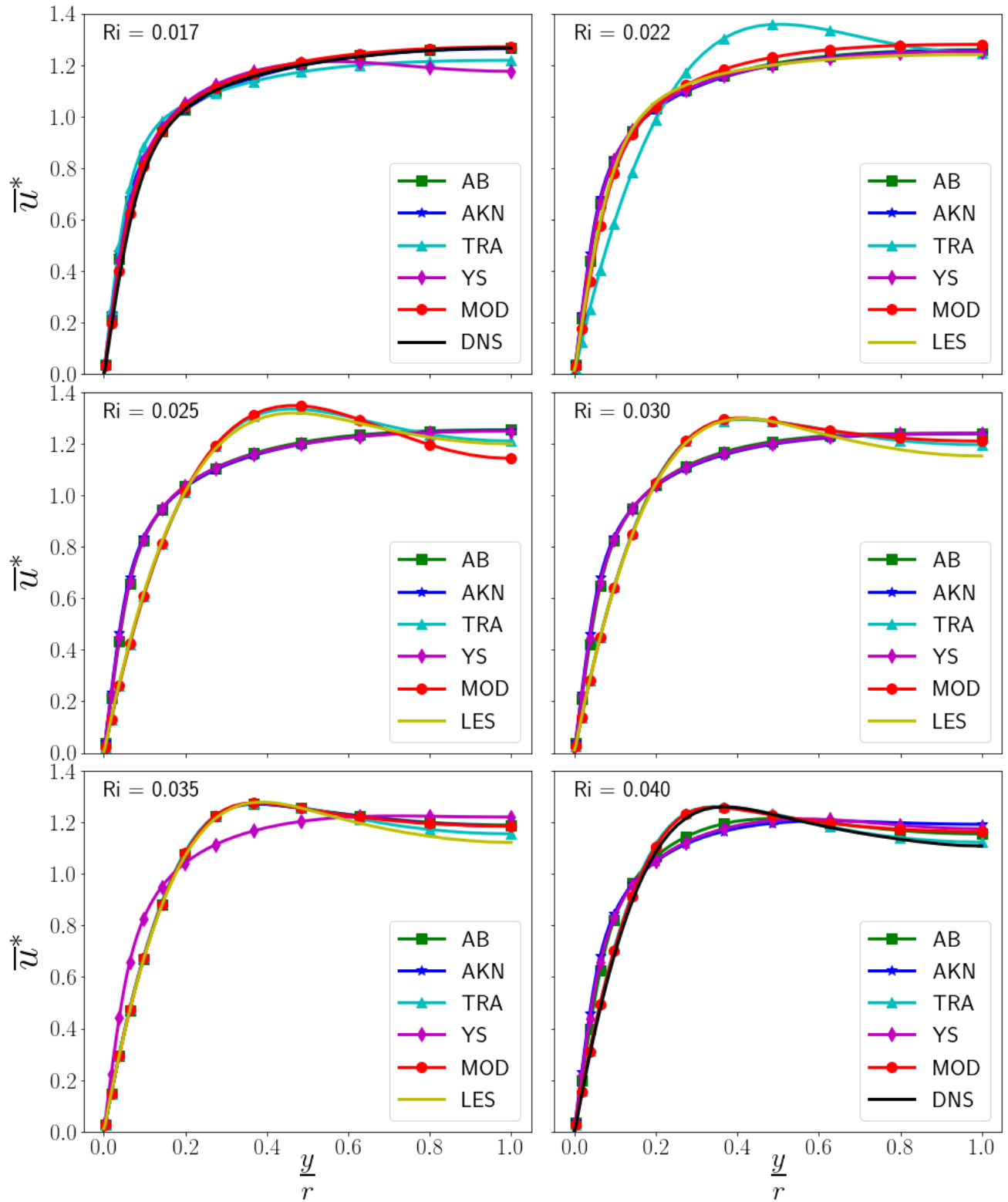
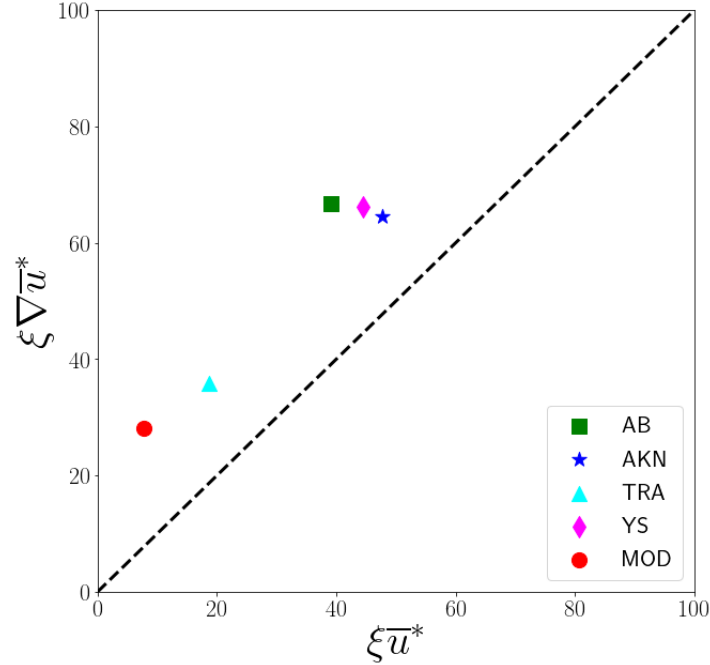Figure 4.8: Mean axial velocity profiles plotted in global coordinates

Figure 4.9: Comparison of relative error for each model for $\overline{u}^*$

It is a commonly known problem that many RANS models have trouble capturing the stream-wise Reynolds stress for forced and mixed convection [48] [34]. None of these models are able to accurately capture this stress with any accuracy as seen in Figure 4.10. The reason for this lies in the Bousinessq hypothesis which is used to determine the Reynold stress tensor. Two equation eddy viscosity models utilize a constitutive linear relationship to determine the Reynolds stresses. Regardless of this, these models have been shown to be fairly capable at predicting fundamental flows. With this in mind, there are some positives. Both TRA and MOD show sensitivity to the presence of buoyancy, while the other models remain relatively insensitive. TRA predicts a sharp decline in the stresses much earlier than the other models, while MOD better predicts this behavior. The other models are further shown to be erratic. Figure 4.11 shows the relative error for each model. The trend reverses from the mean velocity predictions. AB, AKN, and YS have the best predictions. This is largely due to the predictions of TRA and MOD being effectively zero at multiple locations for multiple Richardson numbers.
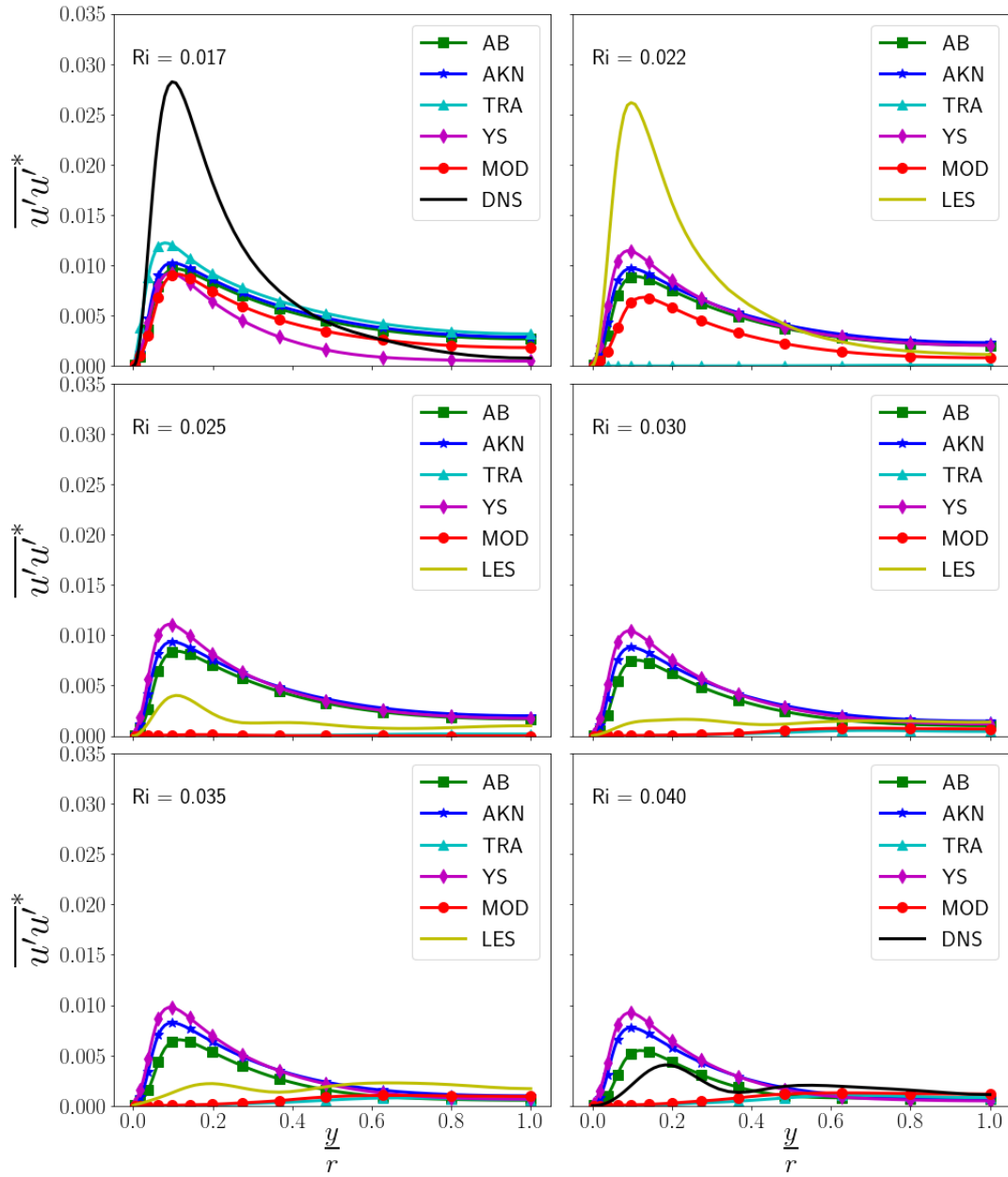
96

Figure 4.10: Comparison of the stream-wise Reynolds stress $\overline{u'u'}^*$ for each Richardson number, 0.017 to 0.040
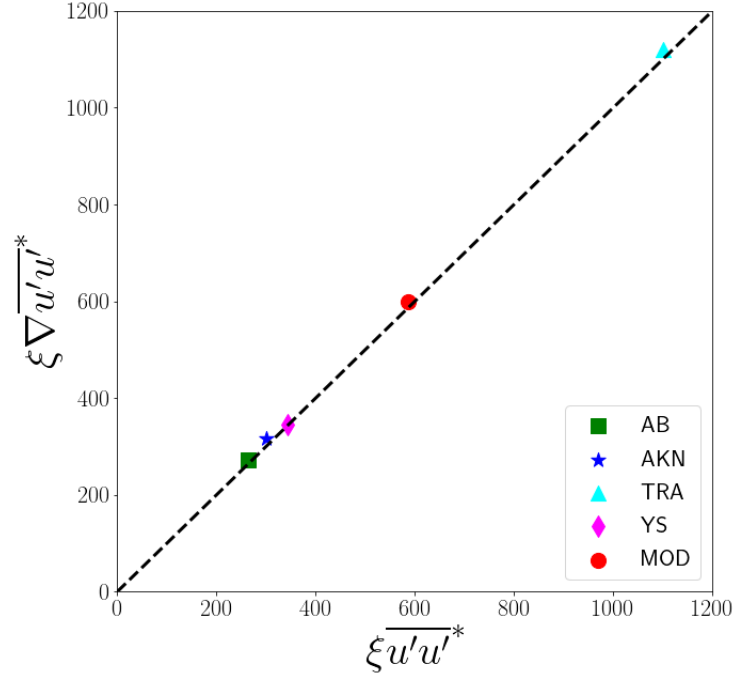
Figure 4.11: Comparison of relative error for each model for stream-wise Reynolds stress $\overline{u'u'}^*$

Figure 4.12 shows the comparison between the Reynolds shear stress $(\overline{u'v'}^*)$ for each model against the validation DNS and LES data. As expected, this follows similar trends seen in 4.6. Specifically, the low Reynolds $k - \epsilon$ models do not show the ability to adapt to buoyancy in their predictions of the shear stress, while TRA initially is unable to predict the shear stress before the onset of laminarization. Figure 4.13 shows a similar trend as 4.9, in regards to the ordering of the models with MOD providing the best prediction.

Through this calibration and comparison it is shown that the near wall modeling of the turbulent viscosity is a large reason for the failure of the low Reynolds models and their ability to predict buoyancy aided mixed convection. With this correction being made at each Richardson number for MOD, the turbulent viscosity is adjusted resulting in improved predictions of the shear stress and resulting axial velocity profiles. To further show how this change affects the flow, we analyse the resulting change to the production (P_k) and dissipation $(\bar{\epsilon})$ terms.
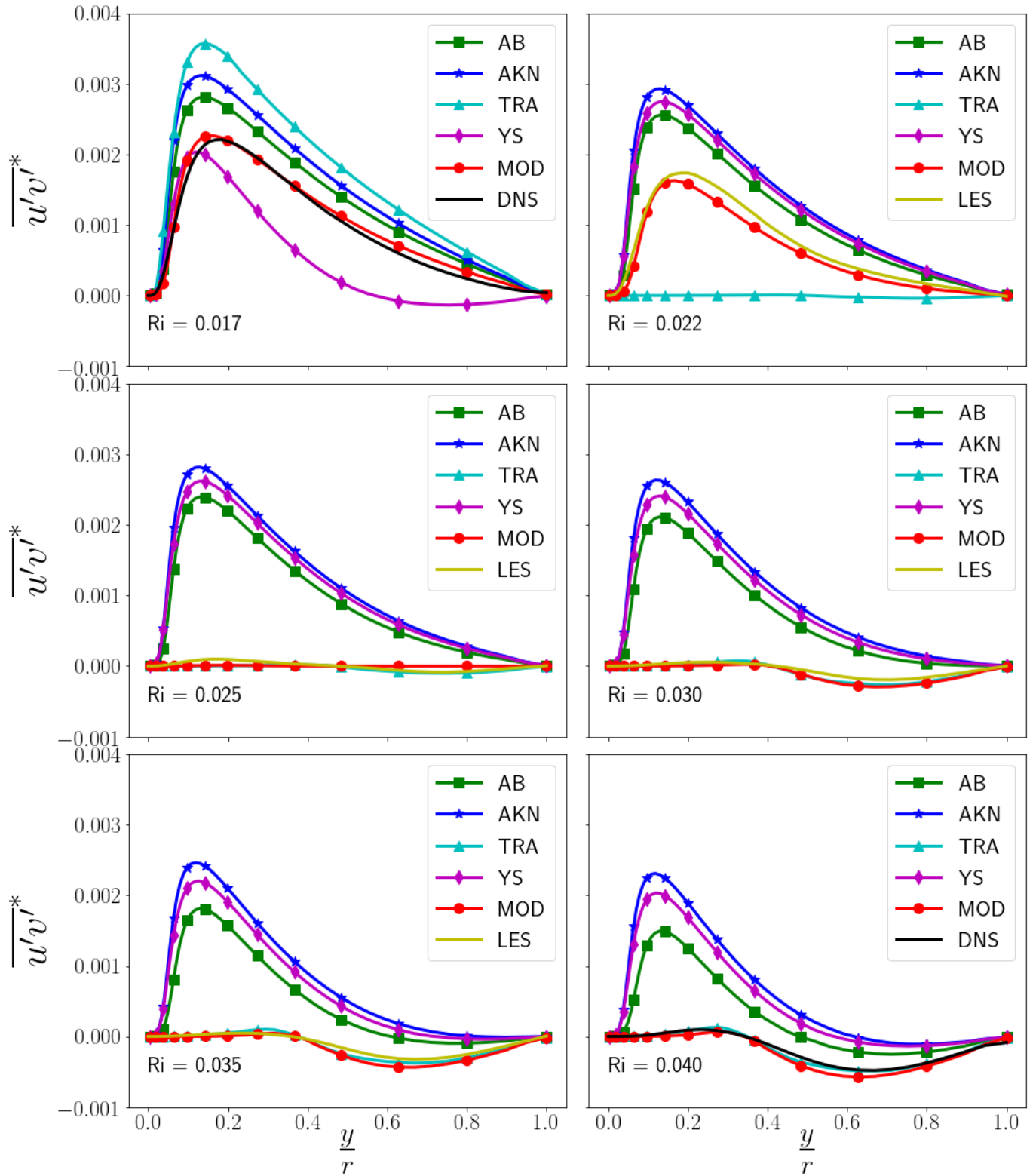
Figure 4.12: Comparison of the Reynolds shear stress $\overline{u'v'}^*$ for each Richardson number, 0.017 to 0.040
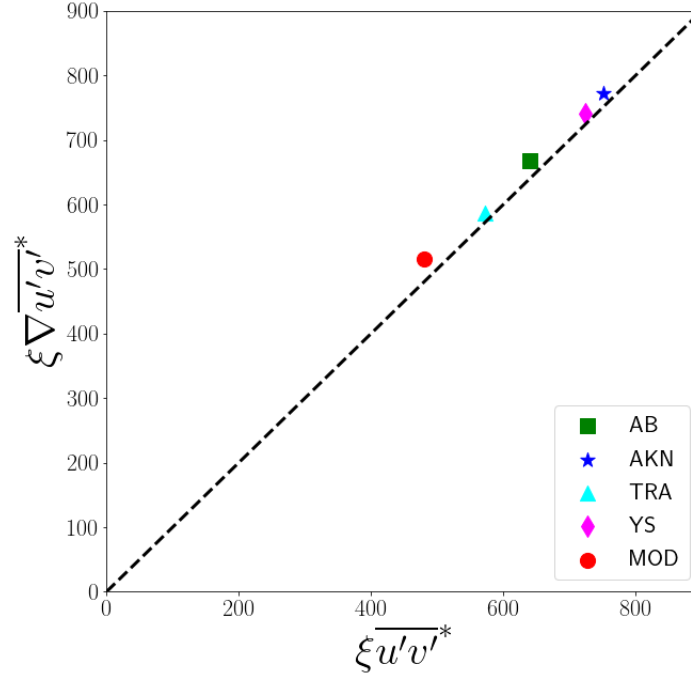
Figure 4.13: Comparison of relative error for each model for the Reynolds shear stress, $\overline{u'v'}^*$

As shown by Zhao et al. [27], You et al. [26] and the current investigation, two of the main contributions in this flow are production of turbulence kinetic energy (P_k) and dissipation of turbulence kinetic energy ($\bar{\epsilon}$). Though the turbulent viscosity (ν_t) is not directly used in their calculation, we see a feedback effect present in their predictions. With the adjustment of the Reynolds shear stress and resulting velocity profile a similar correction is made to the production term modeled as in Equation 4.9. Figure 4.14 shows the resulting comparison between all models and the DNS and LES validation data. Similar trends prevail here as previously discussed as the MOD model is able to more accurately capture the production as show in 4.15.
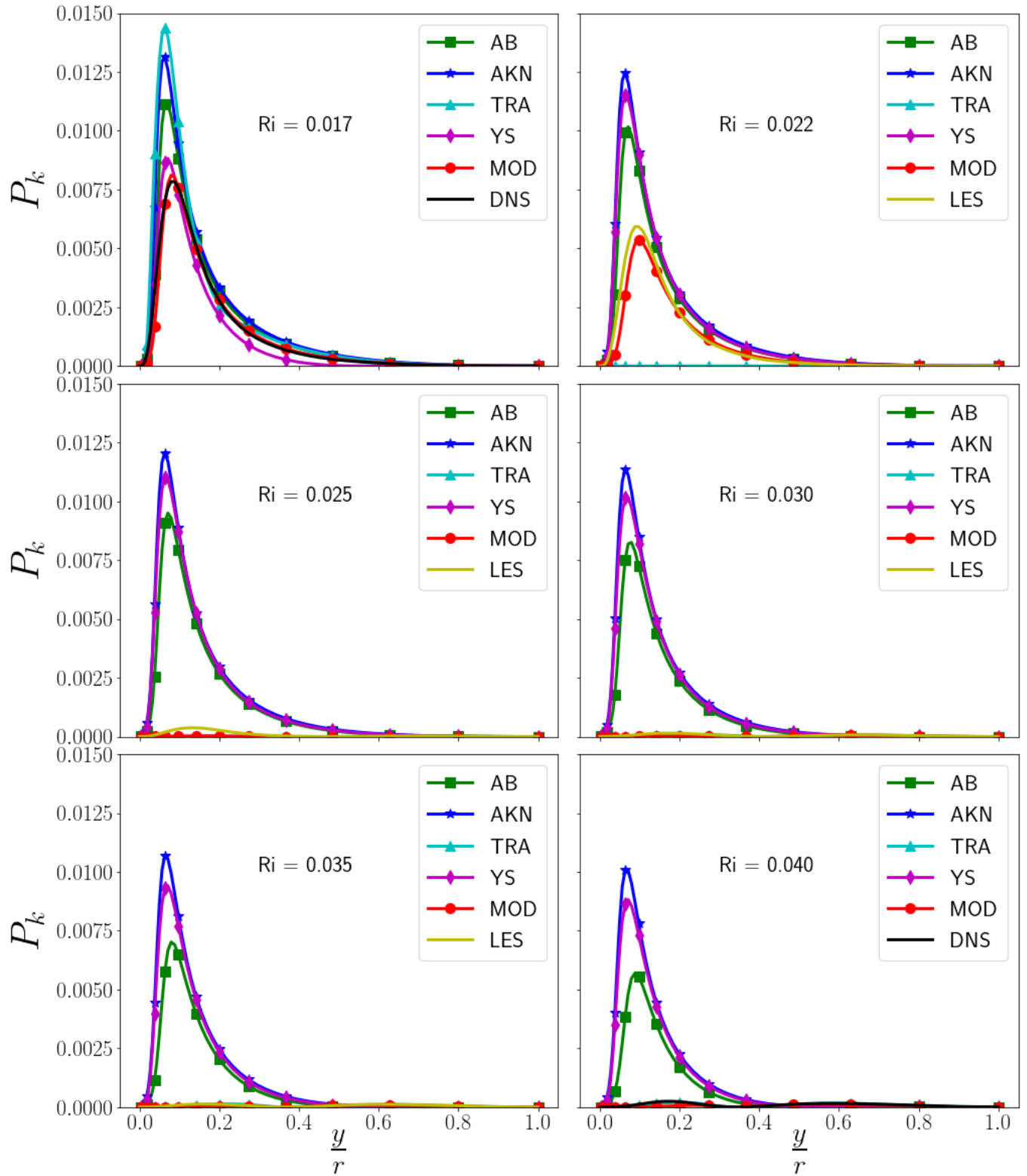
Figure 4.14: Comparison of the production of turbulence kinetic energy, P_k, for each Richardson number, 0.017 to 0.040
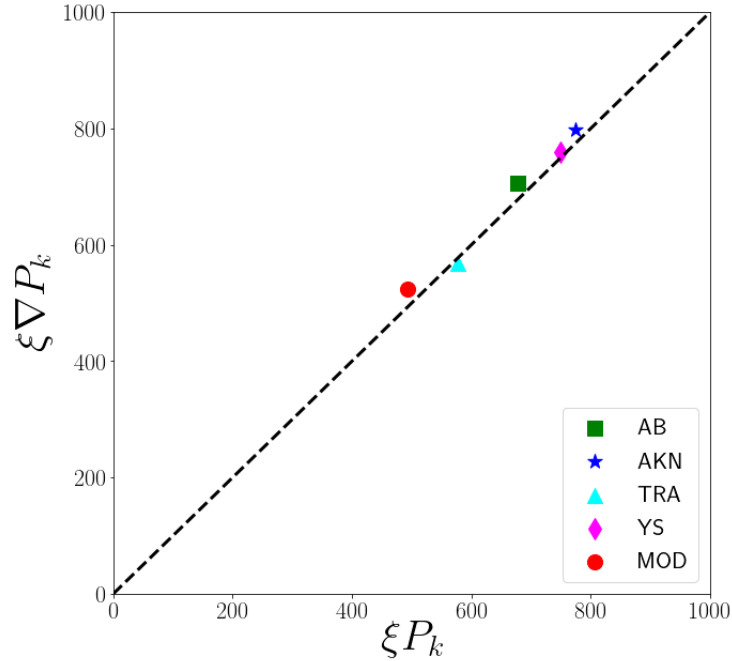
Figure 4.15: Comparison of relative error for each model for the production of turbulence kinetic energy, P_k

Similar to the production calculation, the turbulent viscosity is not directly used to calculate dissipation of turbulence kinetic energy. Figure 4.16 shows each model's prediction of the dissipation (note: the x-axis is presented in log scale to highlight the near wall profiles). Although, TRA does not directly calculate dissipation in the same manner as $k - \epsilon$ models do, the equivalent dissipation can be calculated for comparison. With this comparison available along with 4.14, reasons for the TRA models missed predictions for $Ri = 0.017$ and 0.022 are made clear. At $Ri = 0.017$, the production is over predicted while simultaneously under predicting the effective dissipation resulting in an increased Reynolds shear stress prediction, which ultimately causes poor prediction of the skin friction coefficient. At $Ri = 0.022$, both the production and dissipation terms for TRA disappear, which results in the prediction of laminarization occurring while the flow should remain turbulent. Figure 4.17 shows the error in the models in comparison to each other. This shows that MOD is once again drastically improved from YS. Overall, this further highlights the rationale that

improved turbulent viscosity modeling has vast reaching ramifications and the ability to improve flow predictions.

Figure 4.16: Comparison of dissipation of turbulence kinetic energy $\bar{\epsilon}$ for each Richardson number, 0.017 to 0.040
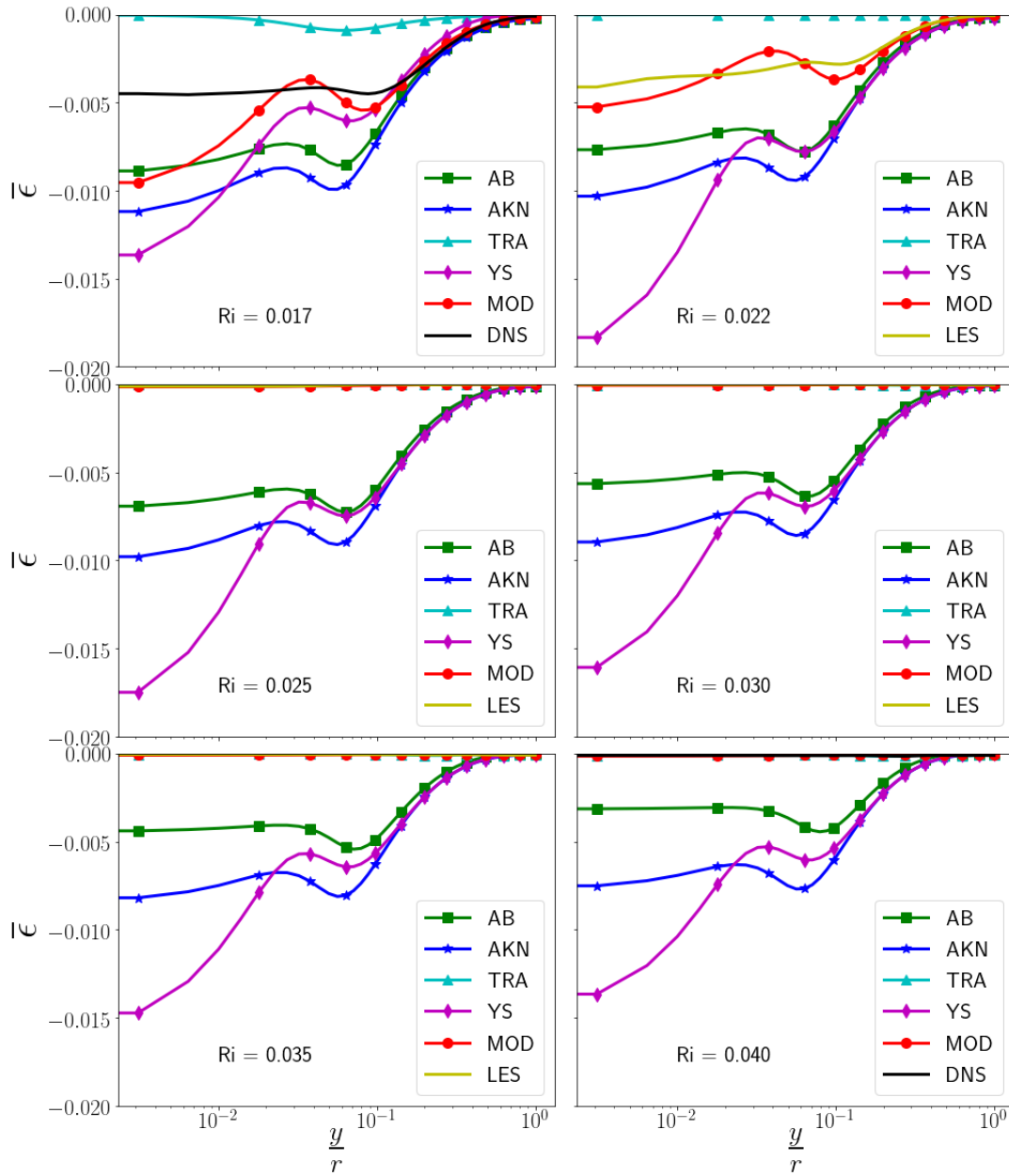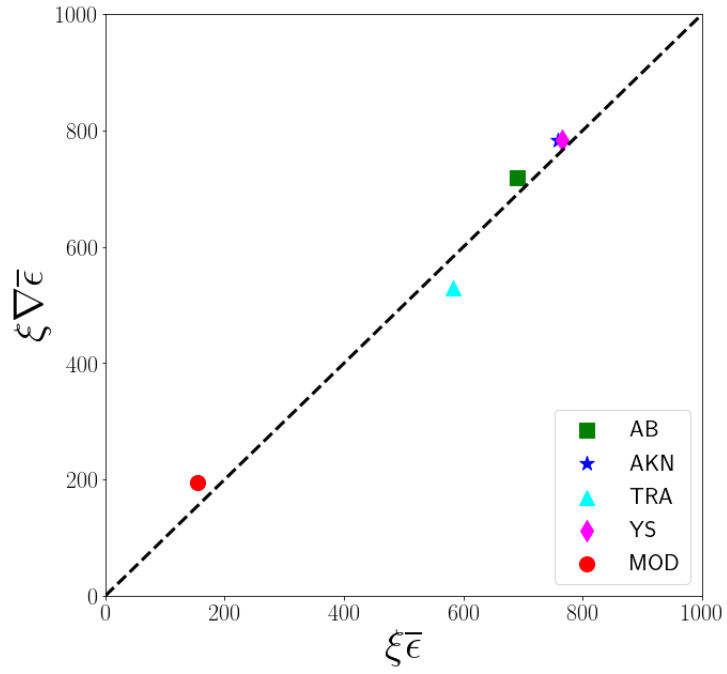
Figure 4.17: Comparison of relative error for each model for the dissipation of turbulence kinetic energy, $\bar{\epsilon}$

4.6 Possible Correlation for Damping Function ($f\mu$)

While the bulk of this investigation focuses on the calibration of the damping function $f\mu$ utilizing the variation of Richardson number for buoyancy-aided mixed convection pipe flow for LBE as a data set for comparison. Therein lies the possibility of determining a correlation between parameters and global flow quantities. Though exhaustive further research is required to effectively determine if a relationship between Richardson number, skin friction, Prandtl number and A1 exists. This initial investigation suggests a relationship between skin friction, Richardson number and A1 for $Re = 5300$. In order to lay the ground work for future work, a piece-wise correlation is proposed. Separating this range into two separate regions ($Ri = 0.017 - 0.030$ and $Ri = 0.030 - 0.040$) with a single connective Richardson number, the following relationship is proposed:

$$
A1 = \begin{cases} -0.3188Ri^2 + 0.00921Ri + 1.916\mathrm{e}05 & 0.017 \leq Ri < 0.030 \\ 3.4\mathrm{e}{-04}Ri - 1.833\mathrm{e}{-06} & 0.030 \leq Ri \leq 0.040 \end{cases}
$$

Both of these relationships can be seen in Figure 4.18. The adjusted R-square is greater than 0.99 for both relationships, suggesting the fit is acceptable for the number of degrees of freedom. While this step is only the first in the arduous journey that is model development, this process hopefully provides some valuable insight to guide model development.
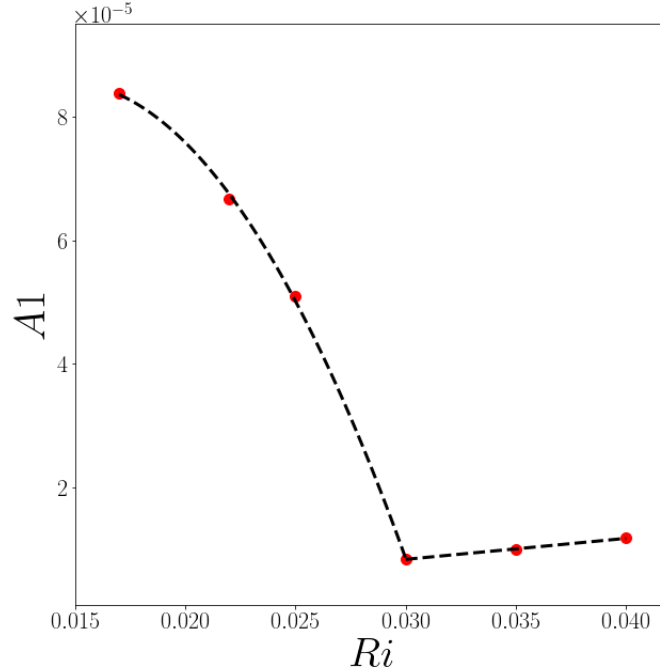
Figure 4.18: Parameter, A1, with piece-wise curve fitting

4.7 Section Conclusion

This investigation develops a framework that is capable of calibrating the damping function f_μ used in various low Reynolds $k - \epsilon$ models. Using the variant proposed by Yang and Shih [43] as a test case, it is shown that this calibration is effective in the computation of multiple SRQs important to the proper calculation of buoyancy-aided mixed convection. This framework is developed within Ansys Fluent [47] using Omniorb [86] and Python 2.8 [85], but could be extended to any open source computational code as a means of model calibration.

Using the hypothesis developed by Clifford and Kimber [34], from this investigation it is definitively shown that modifications made to the turbulent viscosity have a cascading effect that causes corrections in nearly all system response quantities. This aims to possible model development utilizing the already existing low Reynolds $k - \epsilon$ model framework. Further, recommendation can be made that the transition SST model is capable of capturing the proper physics after laminarization has occurred and can be used as-is in this range. It also recommended that this model should

106

be used as a validation metric to compare any future developed models that target this range of laminarization.

5. CONCLUSION

5.1 Summary of Work

From this work, multiple tools for turbulence model comparison and calibration are developed. First, a framework for quantitative comparative error analysis was developed. This framework involved the implementation of the use of various error metrics to predict error in magnitude of system response quantities and their gradients. This provides an additional layer of inspection into the physics of what a model is predicting. Considering only the magnitude of a profile quantitatively can lead to erroneous results in the validation of a model. Inclusion of the gradients of these profiles provides additional information to judge the competence of a model for a given prediction. This method presents as a straight forward and flexible tool that allows the use of various error metrics based on the needs of the data set used in the analysis.

From this framework, a comprehensive analysis was performed using benchmark quality DNS data for both air [24] and lead-bismuth eutectic [27]. From the analysis of lead-bismuth eutectic, a calibration tool was developed that couples the commerical CFD package Ansys Fluent [47] with the open source Python [85] code. This enables a higher level of customization to be achieved within Fluent with the addition of an automated turbulence model calibration for the damping function of low Reynolds $k - \epsilon$ turbulence models. While these models have been widely used and are well known, there exists an untapped potential in their formulation that suggests they're capable of predictions involving buoyancy influence. After completion of this initial calibration study, the need for more high quality data for buoyancy-influenced liquid metal pipe flow was recognized.

Using OpenFOAM [64], LES was performed using DNS for lead-bismuth eutectic [27] as validation. This study was able to determine that laminarization occurs in lead-bismuth eutectic much more abruptly and at a lower Richardson number than previous numerical studies. This study also showed a much larger drop in skin friction and Nusselt number for this particular flow than previous numerical studies had predicted. Further analysis showed how the Reynolds shear stress is

transformed as the force of buoyancy is changed. This provides vital information for lower resolution model development.

With this completed data set now available, further model calibration was performed. This showed the modified low Reynolds $k - \epsilon$ model was capable of predictions for each available Richardson number. From this a possible correlative relationship was proposed that would allow this model to predict buoyancy-aided mixed convection in this range of Richardson numbers for pipe flows. Overall, this work provides new tools for analysis and manipulation of models as well as new insights into the physics of buoyancy influenced flows.

5.2   Proposed Future Work

This dissertation represents a body of work that encompasses multiple aspects of computational modeling with one singular goal, to improve predictions of buoyancy influenced flows. The development of a quantitative framework for assessing model error, generation of benchmark quality LES data, and the automation of calibration of RANS turbulence models provides a basis for future computational researchers to use for years to come.

Through a combination of computational and experimental validation studies, researchers gain vital insight into the capabilities of turbulence models and their formulations. There is a clear link in the necessity of both of these types of studies in regards to nuclear thermal hydraulics. They share a symbiotic relationship, where experiments can gain much needed insight into design and analysis and numerical models gain their validation and determine their advantages and limitations. The Future work should involve extending the quantitative assessment of error to include uncertainty from experimental data with a focus on the propagation of uncertainty through the chosen error metric. This will allow for a wider range of data sets to be utilized in this framework. Use of quantitative analysis is paramount in the design and implementation of next generation nuclear reactor systems, especially with the inclusion of more advanced materials such as liquid metal coolants.

As liquid metals continue to grow in their efficacy as a potential next generation coolant for nuclear reactors, so does the need to fully understand the physics behind the heat transfer and fluid

flow for these exotic materials. Benchmark quality data is still few and far between in comparison to air and water studies. At this point in time, the emphasis needs to be placed on numerical studies to help develop methods to implement experimental studies. Only when this is fully reached, will computational models be fully validated to use for standalone predictive studies. Though, this will significantly rely on the symbiotic relationship of experiments and numerical studies. This work begins to form the relationship between important global metrics and computational parameters, yet there is much work left to be done. There is need for additional studies involving Reynolds number, Prandtl number, Grashof number dependencies for all canonical flows with the inclusion of buoyancy, focused on buoyancy-aided flows. With the determination of these dependencies correlations and improvement to model formulations are possible that will allow better design of experiments in pursuit of the design of next generation nuclear reactors.

REFERENCES

[1] R. P. Garg, J. H. Ferziger, S. G. Monismith, J. R. Koseff, Stably stratified turbulent channel flows. i. stratification regimes and turbulence suppression mechanism, Physics of Fluids 12 (2000) 2569–2594.

[2] T. Tsao, F. Jiang, C. Liu, R. Miller, S. Tung, J. Huang, B. Gupta, D. Babcock, C. Lee, Y. Tai, et al., Mems-based active drag reduction in turbulent boundary layers,'microengineering aerospace systems, ed. helvajian, 1999.

[3] C.-M. Ho, Y.-C. Tai, Micro-electro-mechanical-systems (mems) and fluid flows, Annual review of fluid mechanics 30 (1998) 579–612.

[4] J. Kim, Control of turbulent boundary layers, Physics of fluids 15 (2003) 1093–1105.

[5] H. Branover, Suppression of turbulence in pipes with transverse and longitudinal magnetic fields, Magnetohydrodynamics 47 (1967) 107.

[6] B. Metais, E. Eckert, et al., Regimes of free, forced, and mixed convection for flow through horizontal tubes, Journal of Heat Transfer 86 (1964) 295–296.

[7] B. Petukhov, et al., Turbulent flow and heat transfer in pipes under considerable effect of thermogravitational forces, Heat transfer and turbulent buoyant convection 2 (1976).

[8] B. P. Axcell, W. Hall, Mixed convection to air in a vertical pipe, in: International Heat Transfer Conference Digital Library, Begel House Inc., 1978.

[9] J. Easby, The effect of buoyancy on flow and heat transfer for a gas passing down a vertical pipe at low turbulent reynolds numbers, International Journal of Heat and Mass Transfer 21 (1978) 791–801.

[10] J. Jackson, F. J, Enhancement of turbulent heat transfer due to buoyancy for downward flow of water in vertical tubes. (1977).

[11] M. Watts, C. Chou, Mixed convection heat transfer to supercritical pressure water, in: International Heat Transfer Conference Digital Library, Begel House Inc., 1982.

[12] A. Carr, M. Connor, H. Buhr, Velocity, temperature, and turbulence measurements in air for

pipe flow with combined free and forced convection, Journal of Heat Transfer (1973).

[13] A. Polyakov, S. Shindin, Development of turbulent heat transfer over the length of vertical tubes in the presence of mixed air convection, International journal of heat and mass transfer 31 (1988) 987–992.

[14] B. Fond, C. Abram, A. L. Heyes, A. M. Kempf, F. Beyrau, Simultaneous temperature, mixture fraction and velocity imaging in turbulent flows using thermographic phosphor tracer particles, Optics express 20 (2012) 22118–22133.

[15] A. Omrane, P. Petersson, M. Aldén, M. Linne, Simultaneous 2d flow velocity and gas temperature measurements using thermographic phosphors, Applied Physics B 92 (2008) 99–102.

[16] S. Someya, Y. Okura, M. Uchida, Y. Sato, K. Okamoto, Combined velocity and temperature imaging of gas flow in an engine cylinder, Optics letters 37 (2012) 4964–4966.

[17] N. J. Neal, J. Jordan, D. Rothamer, Simultaneous measurements of in-cylinder temperature and velocity distribution in a small-bore diesel engine using thermographic phosphors, SAE International Journal of Engines 6 (2013) 300–318.

[18] T. Schulenberg, R. Stieglitz, Flow measurement techniques in heavy liquid metals, Nuclear Engineering and Design 240 (2010) 2077–2087.

[19] H. Buhr, E. Horsten, A. Carr, The distortion of turbulent velocity and temperature profiles on heating, for mercury in a vertical pipe, Journal of Heat Transfer (1974).

[20] J. Jackson, B. Axcell, A. Walton, Mixed-convection heat transfer to sodium in a vertical pipe, EXPERIMENTAL HEAT TRANSFER An International Journal 7 (1999) 71–90.

[21] J. Jackson, Turbulent mixed convection heat transfer to liquid sodium, International Journal of Heat and Fluid Flow 4 (1983) 107–111.

[22] J. Jackson, M. Cotton, B. Axcell, Studies of mixed convection in vertical tubes, International journal of heat and fluid flow 10 (1989) 2–15.

[23] J. Jackson, Fluid flow and convective heat transfer to fluids at supercritical pressure, Nuclear Engineering and Design 264 (2013) 24–40.

[24] N. Kasagi, M. Nishimura, Direct numerical simulation of combined forced and natural tur-

bulent convection in a vertical plane channel, International Journal of Heat and Fluid Flow 18 (1997) 88–99.

[25] Y. Ohtsubo, Direct numerical simulation of liquid metal mhd turbulence (in japanese), J. Jap. Soc. Fluid Mech. 11 (1992) 67–73.

[26] J. You, J. Y. Yoo, H. Choi, Direct numerical simulation of heated vertical air flows in fully developed turbulent mixed convection, International Journal of Heat and Mass Transfer 46 (2003) 1613–1627.

[27] P. Zhao, J. Zhu, Z. Ge, J. Liu, Y. Li, Direct numerical simulation of turbulent mixed convection of lbe in heated upward pipe flows, International Journal of Heat and Mass Transfer 126 (2018) 1275–1288.

[28] S. He, K. He, M. Seddighi, Laminarisation of flow at low reynolds number due to streamwise body force, Journal of Fluid Mechanics 809 (2016) 31–71.

[29] M. Duponcheel, L. Bricteux, M. Manconi, G. Winckelmans, Y. Bartosiewicz, Assessment of rans and improved near-wall modeling for forced convection at low prandtl numbers based on les up to reτ= 2000, International Journal of Heat and Mass Transfer 75 (2014) 470–482.

[30] Y.-Y. Bae, E.-S. Kim, M. Kim, Assessment of low-reynolds number k-ε turbulence models against highly buoyant flows, International Journal of Heat and Mass Transfer 108 (2017) 529–536.

[31] A. Keshmiri, M. A. Cotton, Y. Addad, D. Laurence, Turbulence models and large eddy simulations applied to ascending mixed convection flows, Flow, turbulence and combustion 89 (2012) 407–434.

[32] A. Keshmiri, J. Uribe, N. Shokri, Benchmarking of three different cfd codes in simulating natural, forced, and mixed convection flows, Numerical Heat Transfer, Part A: Applications 67 (2015) 1324–1351.

[33] A. Keshmiri, A. Revell, H. G. Darabkhani, Assessment of a common nonlinear eddy-viscosity turbulence model in capturing laminarization in mixed convection flows, Numerical Heat Transfer, Part A: Applications 69 (2016) 146–165.

[34] C. E. Clifford, M. L. Kimber, Assessment of rans-based turbulence models for buoyancy-influenced forced convection on a heated vertical surface, Journal of Verification, Validation and Uncertainty Quantification 5 (2020).

[35] A. Shams, A. De Santis, L. Koloszar, A. V. Ortiz, C. Narayanan, Status and perspectives of turbulent heat transfer modelling in low-prandtl number fluids, Nuclear Engineering and Design 353 (2019) 110220.

[36] A. Shams, A. De Santis, Towards the accurate prediction of the turbulent flow and heat transfer in low-prandtl fluids, International Journal of Heat and Mass Transfer 130 (2019) 290–303.

[37] F. Roelofs, A. Shams, I. Otic, M. Böttcher, M. Duponcheel, Y. Bartosiewicz, D. Lakehal, E. Baglietto, S. Lardeau, X. Cheng, Status and perspective of turbulence heat transfer modelling for the industrial application of liquid metal flows, Nuclear Engineering and Design 290 (2015) 99–106.

[38] G. Grötzbach, Challenges in low-prandtl number heat transfer simulation and modelling, Nuclear engineering and design 264 (2013) 41–55.

[39] S. Kenjereš, S. Gunarjo, K. Hanjalić, Contribution to elliptic relaxation modelling of turbulent natural and mixed convection, International Journal of Heat and Fluid Flow 26 (2005) 569–586.

[40] A. Shams, F. Roelofs, E. Baglietto, S. Lardeau, S. Kenjeres, Assessment and calibration of an algebraic turbulent heat flux model for low-prandtl fluids, International Journal of Heat and Mass Transfer 79 (2014) 589–601.

[41] D. De Santis, A. De Santis, A. Shams, T. Kwiatkowski, The influence of low prandtl numbers on the turbulent mixed convection in an horizontal channel flow: Dns and assessment of rans turbulence models, International Journal of Heat and Mass Transfer 127 (2018) 345–358.

[42] A. De Santis, A. Shams, Application of an algebraic turbulent heat flux model to a backward facing step flow at low prandtl number, Annals of Nuclear Energy 117 (2018) 32–44.

[43] Z. Yang, T.-H. Shih, New time scale based k-epsilon model for near-wall turbulence, AIAA

journal 31 (1993) 1191–1198.

[44] C. Lam, K. Bremhorst, A modified form of the k-ε model for predicting wall turbulence (1981).

[45] G. Centurelli, Large eddy simulation of mixed convection to a low prandtl number fluid in a vertical pipe flow, Master's Thesis (2019).

[46] I. Ansys, Cfd, ICEM CFD theory guide, Ansys inc (2015).

[47] A. Fluent, et al., Ansys fluent theory guide, ANSYS Inc., USA 15317 (2011) 724–746.

[48] W. Kim, S. He, J. Jackson, Assessment by comparison with dns data of turbulence models used in simulations of mixed convection, International Journal of Heat and Mass Transfer 51 (2008) 1293–1312.

[49] B. E. Launder, D. B. Spalding, Mathematical models of turbulence, BOOK, Academic press, 1972.

[50] M. Wolfshtein, A. Lin, D. Naot, Models of turbulence, In: Topics in transport phenomena: Bioprocesses, mathematical treatment, mechanisms.(A76-23569 09-34) Washington, DC, Hemisphere Publishing Corp.; New York, Halsted Press, 1975, p. 3-45. (1975) 3–45.

[51] T. Jongen, Simulation and modeling of turbulent incompressible fluid flows, Technical Report, EPFL, 1998.

[52] C. G. Speziale, R. Abid, E. C. Anderson, Critical evaluation of two-equation models for near-wall turbulence, AIAA journal 30 (1992) 324–331.

[53] S. Patankar, Numerical heat transfer and fluid flow, Taylor & Francis, 2018.

[54] C. Rhie, W. L. Chow, Numerical study of the turbulent flow past an airfoil with trailing edge separation, AIAA journal 21 (1983) 1525–1532.

[55] A. S. of Mechanical Engineers, Standard for Verification and Validation in Computational Fluid Dynamics and Heat Transfer: An American National Standard, American Society of Mechanical Engineers, 2009.

[56] W. L. Oberkampf, C. J. Roy, Verification and validation in scientific computing, Cambridge University Press, 2010.

115

[57] P. J. Roache, Verification and validation in computational science and engineering, volume 895, Hermosa Albuquerque, NM, 1998.

[58] B. A. Kitchenham, L. M. Pickard, S. G. MacDonell, M. J. Shepperd, What accuracy statistics really measure, IEE Proceedings-Software 148 (2001) 81–85.

[59] J. S. Armstrong, L.-R. Forecasting, From crystal ball to computer, New York ua (1985).

[60] S. Makridakis, Accuracy measures: theoretical and practical concerns, International Journal of Forecasting 9 (1993) 527–529.

[61] J. S. Armstrong, F. Collopy, Error measures for generalizing about forecasting methods: Empirical comparisons, International journal of forecasting 8 (1992) 69–80.

[62] L. Törnqvist, P. Vartia, Y. O. Vartia, How should relative changes be measured?, The American Statistician 39 (1985) 43–46.

[63] J. O. Hinze, Turbulent fluid and particle interaction, in: Proceedings of the International Symposium on Two-Phase Systems, Elsevier, 1972, pp. 433–452.

[64] T. O. Foundation, 2020. URL: `https://cfd.direct/openfoam/user-guide`.

[65] S. Van Haren, Testing dns capability of openfoam and star-ccm+, Master's Thesis (2011).

[66] A. Yoshizawa, Statistical theory for compressible turbulent shear flows, with the application to subgrid modeling, The Physics of fluids 29 (1986) 2152–2164.

[67] W.-W. Kim, S. Menon, A new dynamic one-equation subgrid-scale model for large eddy simulations, in: 33rd Aerospace Sciences Meeting and Exhibit, 1995, p. 356.

[68] M. Germano, U. Piomelli, P. Moin, W. H. Cabot, A dynamic subgrid-scale eddy viscosity model, Physics of Fluids A: Fluid Dynamics 3 (1991) 1760–1765.

[69] D. K. Lilly, A proposed modification of the germano subgrid-scale closure method, Physics of Fluids A: Fluid Dynamics 4 (1992) 633–635.

[70] F. Nicoud, F. Ducros, Subgrid-scale stress modelling based on the square of the velocity gradient tensor, Flow, turbulence and Combustion 62 (1999) 183–200.

[71] B. J. Geurts, J. Fröhlich, A framework for predicting accuracy limitations in large-eddy simulation, Physics of fluids 14 (2002) L41–L44.

[72] I. Celik, Z. Cehreli, I. Yavuz, Index of resolution quality for large eddy simulations (2005).

[73] S. B. Pope, Turbulent flows, 2001.

[74] K. Lilly, The representation of small-scale turbulence in numerical simulation experiments (1966).

[75] R. Absi, A simple eddy viscosity formulation for turbulent boundary layers near smooth walls, Comptes Rendus Mecanique 337 (2009) 158–165.

[76] K. Fukagata, K. Iwamoto, N. Kasagi, Contribution of reynolds stress distribution to the skin friction in wall-bounded flows, Physics of Fluids 14 (2002) L73–L76.

[77] W.-H. Cai, F.-C. Li, H.-N. Zhang, X.-B. Li, B. Yu, J.-J. Wei, Y. Kawaguchi, K. Hishida, Study on the characteristics of turbulent drag-reducing channel flow by particle image velocimetry combining with proper orthogonal decomposition analysis, Physics of Fluids 21 (2009) 115103.

[78] J. M. Wallace, Quadrant analysis in turbulence research: history and evolution, Annual Review of Fluid Mechanics 48 (2016) 131–158.

[79] J. L. Lumley, Computational modeling of turbulent flows, in: Advances in applied mechanics, volume 18, Elsevier, 1979, pp. 123–176.

[80] J. C. Hunt, A. A. Wray, P. Moin, Eddies, streams, and convergence zones in turbulent flows (1988).

[81] V. Kolář, Vortex identification: New requirements and limitations, International journal of heat and fluid flow 28 (2007) 638–652.

[82] D. C. Wilcox, et al., Turbulence modeling for CFD, volume 2, DCW industries La Canada, CA, 1998.

[83] F. R. Menter, Two-equation eddy-viscosity turbulence models for engineering applications, AIAA journal 32 (1994) 1598–1605.

[84] F. R. Menter, R. B. Langtry, S. Likki, Y. Suzen, P. Huang, S. Völker, A correlation-based transition model using local variables—part i: model formulation (2006).

[85] G. Van Rossum, F. L. Drake Jr, Python reference manual, Centrum voor Wiskunde en Infor-

matica Amsterdam, 1995.

[86] Apasphere Ltd, OmniOrb, Version 2.1, http://omniorb.sourceforge.net/.